STUDIES OF THE STRUCTURE AND EVOLUTION OF THE INTRACLUSTER MEDIUM

BY

TIMOTHY BRIAN O'HARA

B.S., Carnegie Mellon University, 2001
M.S., University of Illinois at Urbana-Champaign, 2003

DISSERTATION

Submitted in partial fulfillment of the requirements
for the degree of Doctor of Philosophy in Physics
in the Graduate College of the
University of Illinois at Urbana-Champaign, 2007

Urbana, Illinois

Doctoral Committee:

Professor Frederick K. Lamb, Chair
Associate Professor Joseph J. Mohr, Adviser
Professor Jon J. Thaler
Professor James P. Wolfe

Abstract

The intracluster medium (ICM) in galaxy clusters is influenced by multiple processes, such as mergers and radiative cooling. In this dissertation we examine how these processes affect the structure and formation history of the ICM via both detailed individual cluster study and by study of bulk properties in large cluster data sets. This work provides important constraints on the evolution of the ICM, and in particular on the effects of mergers and cool core formation on ICM structure.

We use high-resolution X-ray data to identify merger features in the cluster A2319, and propose a dynamical model for the merger. Remarkably, the bulk properties of this merging cluster are not significantly perturbed relative to the values predicted by scaling relations.

This question of merger effects on bulk properties is pursued further in a study of 45 nearby clusters. We show that cool core-related phenomena, and not mergers, are the primary source of scatter in scaling relations among bulk properties. This surprising result, with greater scatter in the cool core population than in non-cool core clusters, may support cluster formation scenarios in which the presence of a cool core is primarily determined by factors beyond simply the time since the last major merger. We show that the central X-ray surface brightness can be used to significantly decrease the scatter in scaling relations by acting as a proxy for cool core "strength", a finding beneficial for cluster cosmology surveys that use X-ray luminosity as a proxy for mass.

Finally, we examine how scaling relations evolve with redshift using a 70 cluster sample over the redshift range $0.18 < z < 1.24$. We show that X-ray luminosity and ICM mass evolve more slowly toward higher redshifts than is predicted by self-similar models of cluster formation. Effects of core structure are again apparent in this work, as scaling relations constructed from core subtracted quantities evolve differently from those using non-core subtracted quantities, and the scatter in scaling relations and in central surface brightness increases at low redshift.

Acknowledgments

First, naturally, thanks to Joe Mohr for patient guidance and for all the opportunities he provided for me to develop as a scientist (including the ones I didn't take advantage of!).

Thanks also to my fellow group members who helped in some way: Yen-Ting Lin, for assistance with the near-IR data; Alastair Sanderson, for a tremendous amount of help with *Chandra* reduction; and Jeeseon Song, for helping me keep track of our adviser. My thanks also to other collaborators, including John Bialek, Prof. Gus Evrard, and Martín Guerrero.

Thanks to Prof. Yasushi Suto for hosting my stay at the University of Tokyo, and to Prof. Tetsu Kitayama for his assistance in the application process.

Ending up in this position took a lot of help over a lot of years. Under the assumption ending up here was a good thing, a few more thanks are in order. First, my parents, for letting their 16 year old go off to (more or less) college, and in the years following not insisting that he should consider engineering instead. Prof. Paul Marshall gave me my first research experience in his physical chemistry lab at the University of North Texas, and helped solidify my interest in the physical sciences (even if Organic wound up sending me scurrying away from chemistry). At Carnegie Mellon, Prof. Steve Garoff gave major grad school help and advice, while teaching a fantastic lab course; Prof. Jeff Peterson gave an astrophysics course which I took on a whim, but which must have made quite an impression; and Prof. Bob Nichol taught a cosmology course that involved my first real contact with astronomical data analysis, which turned out to be rather fun. Finally, Prof. Margaret Meixner kindly took me on, sight unseen, and supervised (and funded) my first graduate research project.

And of course, thanks to my lovely wife Mădălina, with whom grad school was, all in all, quite a pleasant experience. Te iubesc, păpuşică!

This work was supported by the *Chandra X-ray Observatory* grant G02-3181X, NASA Long Term Space Astrophysics grant NAG 5-11415, a NASA Graduate Student Researchers Program fellowship (NNG05GO42H),

and an NSF/JSPS East Asia and Pacific Summer Institutes award (NSF Grant No. 0611808).

The material in chapters 2 and 3 has been published in the *Astrophysical Journal*, as noted in each chapter. Modifications to the published material have been made for style and for minor corrections that do not affect the scientific conclusions.

Table of Contents

List of Tables

List of Figures

Chapter 1

Introduction

In this chapter we give some brief background on galaxy cluster structure, and describe the motivation behind the work contained in this dissertation. Detailed introductions for each subject are given in the individual relevant chapters.

1.1 Cluster Background

Clusters of galaxies are the most massive collapsed structures at the present epoch. Their large masses (typically $\sim 10^{14}$–10^{15} $M_{\odot}$) are dominated by dark matter, which at $\sim$80% of the cluster mass far exceeds the mass contribution of the galaxies themselves, which make up only a few percent of cluster mass. The remaining $\sim$15% of cluster mass is in a hot ($\sim 10^{7}$–10^{8} K), diffuse ($\sim 10^{-3}$ cm^{-3}) intracluster medium (ICM) that fills the space between the cluster galaxies.

The ICM is what make clusters observable in X-rays, and indeed clusters are, excepting quasars, the most X-ray luminous objects in the universe, with typical X-ray luminosities of $\sim 10^{43}$–10^{45} erg s^{-1}. This X-ray emission arises primarily from thermal bremsstrahlung, with some contribution from atomic line emission. The emissivity of the ICM varies with the square of the gas density, which has the practical result of making X-ray surveys an attractive means of finding large numbers of clusters in surveys that seek to use clusters to constrain cosmological parameters by, for example, measuring the mass function of clusters and its evolution with cosmic time (e.g., Bahcall & Cen 1993; Bahcall et al. 1997; Reiprich & Böhringer 2002).

However, accurate direct measurements of the mass of clusters with X-ray observations requires long exposure times and high-resolution spectral data. Fortunately, clusters exhibit regular power law scaling relations among parameters such as total mass, ICM mass, X-ray luminosity, and ICM temperature, making it possible to use an easily measured observable (such as luminosity) as a proxy for the underlying halo mass. Such scaling relations are a natural prediction of simple gravitational collapse models of cluster formation (e.g., Kaiser 1986), wherein clusters gradually accrete material and relax to virial equilibrium. However, the observed scaling relations do not precisely match the predictions of simple spherical collapse models

(e.g., Edge & Stewart 1991; Markevitch 1998; Mohr & Evrard 1997; Mohr et al. 1999), as a result of some combination of radiative cooling of the ICM leading to the formation of cool, dense cores in some clusters, star formation in cluster galaxies, energy injection by supernovae and active galactic nuclei (AGN), cluster formation history, and perhaps other phenomena (e.g., Cavaliere et al. 1998; Bryan 2000; Bialek et al. 2001; Bower et al. 2001; Borgani et al. 2002; McCarthy et al. 2004; Kay et al. 2007). Although scaling relations are recovered in hydrodynamical models of structure formation, the regularity of these relations is not fully understood, as in addition to the above processes clusters undergo frequent mergers (Geller & Beers 1982; Dressler & Shectman 1988; Mohr et al. 1995). Thus, while scaling relations are analytically predicted and are produced in simulations, our understanding of the processes that contribute to their exact form and scatter is still evolving.

In the last few years the study of galaxy clusters has been spurred on by increasingly detailed X-ray spectroscopic and imaging data; large X-ray, optical, and radio surveys; increased interest in clusters as cosmological tools; and progressively more detailed computational simulations. As a result, this is a particularly interesting time to be studying the effects of mergers, core formation, and other aspects of cluster structure on the observed properties of clusters. These phenomena, and their effects on the structure and evolution of the ICM, are the primary subject of this dissertation.

1.2 Detailed Studies of Cluster Structure

Detailed investigations of individual clusters are an important part of cluster studies. The advent of high-resolution X-ray instruments such as *Chandra* and XMM-*Newton* has permitted very detailed spectroscopic and imaging analyses of cluster structure. One particularly notable accomplishment is refutation of the theory of "cooling flows", the flow of radiatively cooled gas into the centers of clusters that was postulated to be a consequence of high X-ray luminosities (e.g., Cowie & Binney 1977; Fabian & Nulsen 1977). Though earlier problems with the cooling flow hypothesis had pointed out by observers (e.g., McNamara & O'Connell 1992; Voit & Donahue 1995), it was these new instruments that provided direct spectroscopic evidence of the nonexistence of cooling flows (e.g., Peterson et al. 2001; Hicks et al. 2002). This has in turn led to searches for the processes that can disrupt cooling, such as AGN and cluster mergers.

Newer X-ray instruments have also led to a large number of detailed studies of merging systems (e.g., Markevitch et al. 2000, 2002; Vikhlinin et al. 2001; Markevitch & Vikhlinin 2001). High-resolution imaging spectroscopy permits detailed investigation of merger features, and led to the discovery of "cold fronts", where cluster cool cores survive through at least the initial stages of mergers (Markevitch et al. 2000).

Observations of the ICM temperature structure and the spatial distribution of interacting galaxy clusters in such systems, especially when combined with observations of cluster galaxies and in some cases, via weak lensing, measurements of the dark matter distribution, provide information about cluster structure in ways often not possible in studies of relaxed systems.

In Chapter 2 we carry out our own detailed study of galaxy cluster A2319, a nearby merging system, using data from *Chandra*. We characterize the merger feature, and suggest a scenario for the ongoing merger. Beyond simply examining the nature of the merger, however, we show that A2319's bulk properties have not been affected to the point of making it stand out significantly from cluster scaling relations. This interesting finding points toward the need for statistical studies of the relationship between the structure of a cluster and its position on scaling relations.

1.3 Cluster Structure and Scaling Relations

While detailed observations of single clusters are an important contribution to cluster studies, there remains the need to examine the relationships between simple observables such as luminosity and cluster mass. As mentioned above, observed scaling relations between such properties do not follow simple predictions, and the precise reasons for this are not yet completely understood. Several factors are undoubtedly important, but two are of primary concern.

First, the ICM undergoes radiative cooling as it emits X-rays. Though the observed rate of cooling does not meet that of the classical "cooling flow" prediction, a large fraction of the cluster population does contain cool, dense cores (e.g., Bauer et al. 2005). Because X-ray emissivity varies with the square of the gas density, these relatively small, unrepresentative core regions can significantly bias measured ICM temperature, X-ray luminosity, and other cluster bulk properties. This results in a separation on scaling relations of the populations of clusters with and without cool cores (e.g., Fabian et al. 1994).

Second, and perhaps of greater concern due to its potential unpredictability, cluster mergers can induce major changes to bulk properties, as large amounts of energy are thermalized and dense shock features are formed in the ICM; simulations of isolated cluster mergers have predicted large, potentially correlated, shifts in temperature and luminosity (Ricker & Sarazin 2001; Randall et al. 2002). For fear that mergers could bias their results, cosmological studies using clusters often specifically exclude systems that appear to be unrelaxed (e.g., Allen et al. 2004). While this may be possible in small surveys where clusters are individually selected, it is not feasible in large surveys over a range of redshifts, wherein many clusters will have observations of insufficient duration or resolution to identify disturbed systems. Over half of clusters

in the local universe show evidence of ongoing or recent mergers (Mohr et al. 1995); it is thus vital for these surveys that the effects of mergers on scaling relations be understood.

In Chapter 3 we carry out a study of such effects in a sample of 45 nearby clusters observed with *ROSAT*, using quantitative substructure measurements and multiple scaling relations. We show that the separation between cool core and non-cool core cluster populations can be largely removed via the use of a third scaling relation parameter, the X-ray central surface brightness, which is well-correlated with the cluster central cooling rate and thus provides a quantitative measure of the "strength" of any cool core. We show that even when core-induced scatter is minimized, however, disturbed systems do not exhibit more scatter about scaling relations than relaxed systems; indeed the opposite is true. Further, clusters with cool cores generally have more scatter about scaling relations than those without. This challenges the conventional view of cluster formation, wherein clusters develop cool cores as they relax in the absence of major merging events, and thus suggests that cool core and non-cool core clusters differ in ways beyond simply the time since last merger.

1.4 Evolution of ICM Structure

The studies discussed above concern the properties of galaxy clusters in the local universe. It is well-established that the slopes and normalizations of *local* cluster scaling relations do not follow the predictions of simple gravitational models, and explaining these differences has resulted in possible models for cooling flow disruption and aspects of cluster formation history. Models of cluster formation also make specific predictions for the *evolution* of scaling relations; for example, the X-ray luminosity within a region corresponding to a fixed overdensity with respect to the background should decrease as the universe expands and the average density drops. While some observations agree with the simplest models for scaling relation evolution (e.g., Vikhlinin et al. 2002; Kotov & Vikhlinin 2005), others do not (e.g., Ettori et al. 2004a; Branchesi et al. 2007). The nature of scaling relation evolution has direct relevance not only to models of clusters themselves, but also to cosmological studies which assume that gas mass fractions (i.e., the fraction of a cluster's mass that lies in the ICM) are constant with redshift (e.g., Rines et al. 1999; Allen et al. 2004).

We enter this debate in Chapter 4 with a study of a 70 cluster sample, using *Chandra* observations of clusters that span $0.2 \lesssim z \lesssim 1.3$; this is the largest data set yet used to study scaling relation evolution. We show that clusters do indeed evolve more slowly with redshift than expected from simple models; that is, cluster luminosity and ICM mass at a fixed temperature are lower than predicted at higher redshifts. The measured evolution in these observables can be modeled as a simple evolution in the gas mass fraction within

the cluster radii we examine, providing a note of caution for cosmology studies that assume this fraction to be constant. Though we do not do a detailed study of the evolution of cluster scatter, there are indications that this scatter increases at lower redshifts, providing evidence for evolution in core structure. Simulations of the evolution of cluster structure are not yet mature enough that we can confirm specific cluster formation models, but this work provides important constraints for future simulations.

1.5 Summary

Cluster studies have advanced dramatically in the period during which this work was carried out. As detailed above, the work described in this dissertation represents a significant contribution to the data constraining models of the structure and formation of the ICM.

In Chapters 2–4 we present the work summarized above, and in Chapter 5 we briefly discuss additional relevant studies that have appeared since this work was carried out, as well as possible directions for future research.

Chapter 2

Effects of a Major Merger on the Structure of A2319

We present an analysis of a *Chandra* observation of the massive, nearby galaxy cluster A2319.[1] A sharp surface brightness discontinuity—suggested by previous, lower angular resolution X-ray imaging—is clearly visible in the ACIS image. This ~300 kpc feature suggests that a major merger is taking place with a significant velocity component perpendicular to the line of sight. The cluster emission-weighted mean temperature is 11.8 ± 0.6 keV, somewhat higher than previous temperature measurements. The *Chandra* temperature map of A2319 reveals substructure resembling that anticipated based on hydrodynamic simulations of cluster mergers, and shows an associated cool core not previously known. The map shows a separation between the intracluster medium (ICM) and galaxies of one subcluster, indicating a transient state in which the ICM has been stripped from the subcluster galaxies (and presumably the dark matter). Detailed analysis of the merger feature shows a pressure change across the surface brightness discontinuity by a factor of $\lesssim 2.5$. The higher density side of the front has a lower temperature, suggesting the presence of a cold front similar to those in many other merging clusters. The velocity of the front is roughly sonic.

We compare bulk properties of the ICM and galaxies in A2319 to the same properties in a large sample of clusters as a way of gauging the effects of the major merger. Interestingly, by comparing A2319 to a sample of 44 clusters studied with the *ROSAT* PSPC we find that the X-ray luminosity, isophotal size, and ICM mass are consistent with the expected values for a cluster of its temperature; in addition, the K-band galaxy light is consistent with the light–temperature scaling relation derived from a sample of ~100 clusters studied with 2MASS. Together, these results indicate either that the merger in A2319 has not been effective at altering the bulk properties of the cluster, or that there are large but correlated displacements in luminosity, isophotal size, ICM mass, galaxy light, and emission-weighted mean temperature in this cluster.

[1]This work has been published as O'Hara, Mohr, & Guerrero 2004, ApJ, 604, 604.

2.1 Introduction

Galaxy cluster mergers are highly energetic events, driving shocks into the intracluster medium (ICM) of the colliding clusters. Flattened and asymmetric X-ray morphologies are signatures of recent merging (Mohr et al. 1993), and these signatures have been used to study the prevalence of merging in large samples of present-epoch clusters (Mohr et al. 1995; Buote & Tsai 1996). A study of X-ray images of a flux-limited sample of 65 clusters indicates that more than half of nearby clusters show evidence of merging (Mohr et al. 1995). Hydrodynamical simulations indicate that complex temperature structures should also be produced in these mergers; however, until relatively recently the required spectral and angular resolution to map this structure has not been available. *Chandra* and *XMM-Newton*, with their high angular resolution, are well-suited for detailed studies of merger features in galaxy clusters (e.g., Markevitch et al. 2000; Vikhlinin et al. 2001; Markevitch & Vikhlinin 2001; Sun et al. 2002; Markevitch et al. 2002; Kempner et al. 2002; Maughan et al. 2003). These studies have already revealed that merger features observed in clusters may not indicate shock fronts, but rather "cold fronts", wherein the cool, dense cores of clusters survive through the initial impact of the merger (Markevitch et al. 2000). In fact, it now appears that many well-known merger candidates contain these cold fronts, e.g., A2142 (Markevitch et al. 2000), A3667 (Vikhlinin et al. 2001), A2256 (Sun et al. 2002), and A85 (Kempner et al. 2002).

Abell 2319 is a massive nearby cluster ($z = 0.0564$; Abell 1958; Struble & Rood 1987). We chose to study it with the high resolution of *Chandra* because its X-ray morphology observed at lower resolution with the *ROSAT* PSPC shows a strong asymmetry or "centroid variation", which is a classic indicator of a recent merger. Our goal in this study is not only to better understand the merger state of A2319, but also to determine how the ongoing merger in A2319 is affecting its bulk ICM and galaxy properties. Of particular interest is understanding how merging—which has long been known to be prevalent in the cluster population (Geller & Beers 1982; Dressler & Shectman 1988; Mohr et al. 1995)—is likely to impact attempts to use cluster surveys to study cosmology (e.g., Haiman et al. 2001; Randall et al. 2002; Majumdar & Mohr 2003, 2004; Hu 2003).

On the basis of galaxy spectra, Faber & Dressler (1977) suggested that A2319 is actually composed of two clusters superimposed along the line of sight, with the smaller subcluster located $\sim 10'$ to the northwest of the main cluster and X-ray surface brightness peak. Additional redshift measurements led to an estimated mean velocity for the main subcluster of $\sim$100 members (hereafter A2319A) of 15,727 km s^{-1}, and for the smaller subcluster of $\sim$25 members (hereafter A2319B) of 18,636 km s^{-1} (Oegerle et al. 1995). This analysis suggests that there is a $\sim$50% chance that the two subclusters are in fact not gravitationally bound and will not merge.

A2319 has been extensively studied with previous X-ray instruments, and the inferences about the cluster dynamical state have been quite varied. Emission-weighted mean temperature estimates are generally in the 9–10 keV range (e.g., David et al. 1993; Markevitch et al. 1998; Molendi et al. 1999; Irwin & Bregman 2000). Markevitch (1996) produced a temperature map of A2319 using *ASCA*. These observations provided no evidence for a cold core region near the surface brightness discontinuity, although a region to the northwest of the brightness peak appeared to have a temperature ~ 1.5 keV lower than the mean. This same subcluster region was identified by Molendi et al. (1999) using *BeppoSAX*; it is proposed that this cool region is associated with subcluster A2319B. Using the *ASCA* temperature map, Markevitch (1996) argued that there is no evidence of a large-scale merger in A2319. Mohr et al. (1995), however, found a value for the centroid variation of A2319 in the *Einstein* IPC image that indicates an ongoing merger. Interestingly, a combined X-ray and radio study of the cluster suggests that the two subclusters are in a premerger state (Feretti et al. 1997). This study also takes note of X-ray evidence for another merger in a late stage taking place along the northeast-southwest direction.

In this chapter, we present a detailed X-ray study of A2319 based on imaging spectroscopy from *Chandra* ACIS-I, providing clear evidence for an ongoing merger of two major subclusters. In §2.2 we present the observations. After a description of the data reduction process in §2.2.1, we present an analysis of the overall cluster spectrum (§2.2.2) and a temperature map of the cluster (§2.2.3). In §2.3 we analyze the merger feature in detail, including quantitative estimates of changes in the physical state of the ICM across the feature, and propose a simple dynamical model. This is followed in §2.4 by a study of how this merger has affected the bulk X–ray properties of the cluster; we examine how A2319—a cluster in the middle of a major merger—behaves relative to an X-ray flux-limited sample of clusters in its luminosity, isophotal size, and ICM mass. Finally, we summarize our conclusions in §2.5.

Throughout this chapter we assume a ΛCDM cosmology with $\Omega_M = 0.3$ and $\Omega_\Lambda = 0.7$, and take the Hubble parameter to be $H_0 = 70\,h_{70}$ km s^{-1} Mpc^{-1}.

2.2 Observation

A2319 was observed with *Chandra* on 2002 March 15 for 14.6 ks using ACIS-I and ACIS-S2, with the ACIS-I field of view centered at $\alpha =$ 19h21m12.00s, $\delta = +43°56'43.7''$, roughly on the surface brightness peak. The pixel scale is $0''.492$. Time bins were checked for periods with count rates greater or less than 20% of the mean; no such intervals were found. Hence all of the data with grades of 0, 2, 3, 4, and 6 were used. The ACIS-I data were adjusted for charge-transfer inefficiency (CTI) using the PSU CTI corrector (Townsley

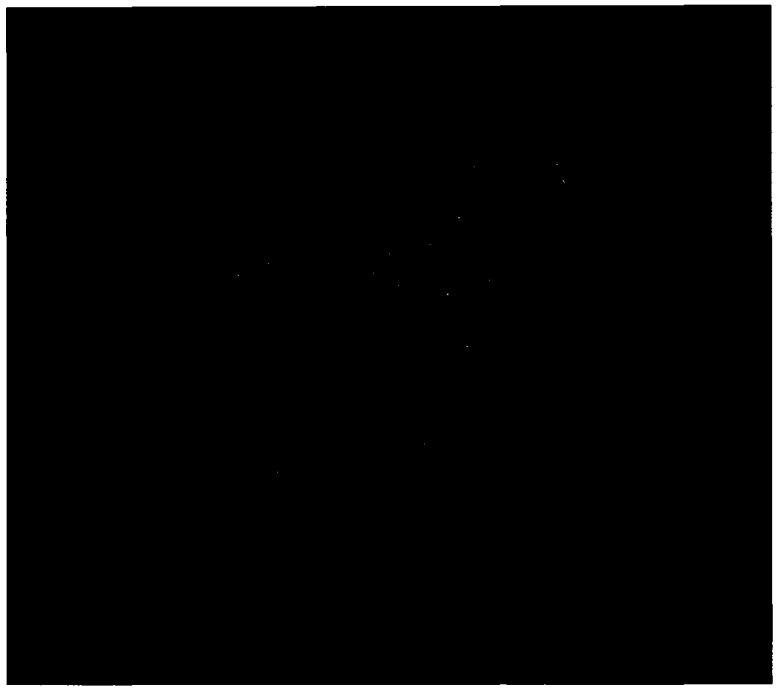

Figure 2.1 — *ROSAT* PSPC image of A2319 with *Chandra* observation footprint overlaid. North is up and east is to the left in all images. The ACIS-I footprint is roughly 17′ on a side.

et al. 2000). We used the *Chandra* data analysis software CIAO, version 2.2, for data reduction. All spectral analysis was done using the X-ray spectral fitting package XSPEC, version 11.2.

2.2.1 Background and Imaging

Because A2319 is a large, nearby cluster, its emission fills the ACIS-I chip, preventing a direct background measurement from that data set. The count rate in the S2 chip is found to be roughly 2 times higher than the typical background rate, making its use for background estimation likewise dubious. One source of this higher than expected rate could be a flare affecting the entire observation; however, the uniformity of the count rate over the exposure time makes this unlikely, and a visual inspection of the S2 spectrum does not reveal any flare-like features. A clear brightness gradient is visible in the exposure-weighted S2 image, as well as in the *ROSAT* PSPC image shown with the *Chandra* footprint in Figure 2.1; hence, it is clear that emission from the very extended cluster is present in the S2 data.

Because there were no portions of the observation without significant cluster contamination, we use the Markevitch blank-sky observations[2]. The background was scaled up by ∼10% after visual comparison of the S2 spectrum and the blank sky spectrum, under the assumption that emission in the 7–10 keV band

[2]http://cxc.harvard.edu/contrib/maxim/acisbg/

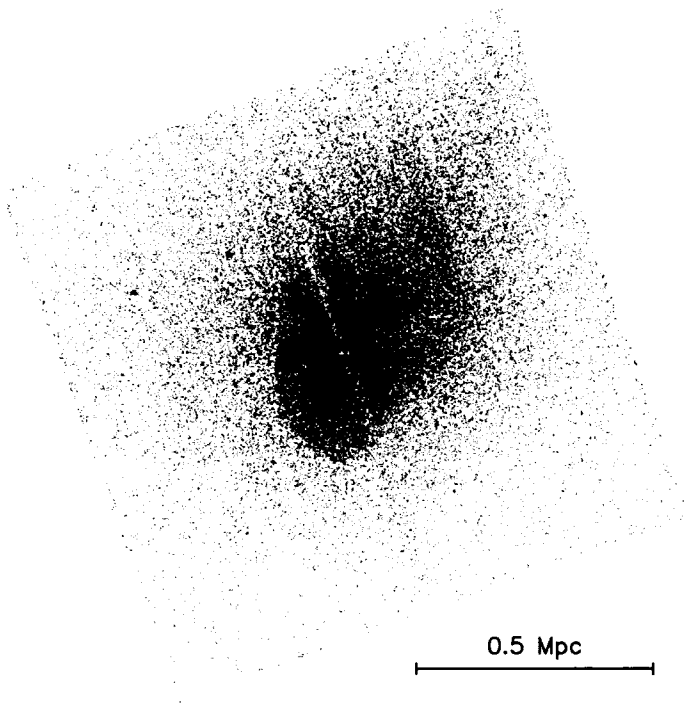

Figure 2.2 — Raw counts ACIS-I image in the 0.5–5 keV band, with pixels binned by 4 (i.e., the pixel scale is $\sim 2''$). The merger feature is visible to the southeast of the brightness peak, and the "tail" of diffuse emission is seen extending to the northwest.

is background dominated. The recommended procedure for using these blank-sky files is to compare the emission in the 10–12 keV band; however, the spectral shapes of the S2 spectrum and the background spectrum are somewhat better matched in the 7.0–10 keV band, and matching the two spectra in the higher band results in obvious oversubtraction at energies below 10 keV. We compared the blank-sky corrected mean surface brightness in the S2 data to that of the background corrected PSPC observation; the *Chandra* measured surface brightness is brighter by a factor of $\sim$1.5.

The raw ACIS-I exposure-weighted counts image in the 0.5-5.0 keV band is shown in Figure 2.2. The presumed merger feature is visible as a sharp surface brightness discontinuity to the southeast of the brightness peak. The presence of the merger signature is much clearer than in previous X-ray observations; the arclike discontinuity and the "tail" of emission towards the northwest strongly resemble similar features in merging clusters such as A2142 and A3667. This is not the possible merger in the northeast-southwest direction discussed by, e.g., Feretti et al. (1997), as it clearly indicates gas movements along the axis connecting A2319A and A2319B.

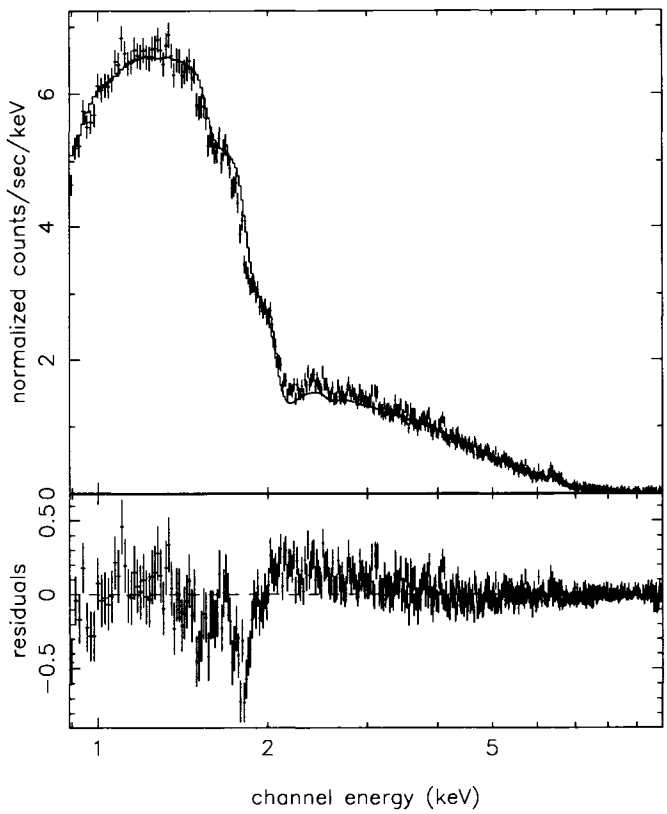

Figure 2.3 — Entire cluster spectrum (excluding point sources) and residuals, plotted with the best-fit MEKAL spectrum described in the text.

2.2.2 Spectral Analysis

All spectra are fitted using a single-temperature MEKAL model, plus components for absorption along the line-of-sight and for absorption due to molecular contamination of the ACIS detector. We fit spectra in the energy range 0.9–10.0 keV; poor understanding of the low-energy response of ACIS-I prevents us from using data at lower energies.

We first fit for temperature and abundance, fixing the hydrogen column density at the Dickey & Lockman (1990) value of 8.33×10^{20} cm^{-2}. Fitting over the entire cluster, excluding point sources, gives $T_{\rm X} = 11.8 \pm 0.2$ keV and $Z = 0.19 \pm 0.03$ (all abundances are in units of solar abundance; all fitted uncertainties are at the 1 σ level), with $\chi^2 = 1017$ for 594 degrees of freedom. This temperature is several standard deviations above previously published estimates, e.g., $T_{\rm X} = 9.2 \pm 0.7$ keV determined by Markevitch et al. (1998) using *ASCA* data. This spectrum is plotted with residuals in Figure 2.3.

Previous studies of A2319 have used hydrogen column densities in the range $(7.85 - 8.9) \times 10^{20}$ cm^{-2}; often the value of $N_{\rm H}$ used is not provided. By fitting the entire cluster spectrum with varying values of

$N_{\rm H}$, we have found that the emission-weighted mean temperature varies roughly linearly with $N_{\rm H}$, with the temperature decreasing by approximately 0.5 keV per 10^{20} cm^{-2} (cluster temperature uncertainties are generally $\sim$0.2 keV). Fitting for the column density along with the other parameters yields $T_{\rm X} = 10.6 \pm 0.3$ keV, $Z = 0.20 \pm 0.03$, and $N_{\rm H} = (10.7 \pm 0.5) \times 10^{20}$ cm^{-2}, with $\chi^2 = 999$ for 593 degrees of freedom.

The Dickey & Lockman (1990) value for the hydrogen column density of 8.33×10^{20} cm^{-2}, as well as other values used in previous studies of A2319, fall a few standard deviations below the range of our fit value. However, uncertainties are not readily available for the HI survey data of Dickey & Lockman (1990); moreover, measured $N_{\rm H}$ values in the region of the sky around A2319 vary to levels above our fit value. A2319 lies at a fairly low galactic latitude where there is a significant amount of interstellar medium along the line of sight, and the optically thin assumption for deriving $N_{\rm H}$ likely underestimates the true column density by a factor of 1.1–1.3 (Dickey & Lockman 1990). Further, with a column density this high there is likely to be a significant contribution ($\geq$ 10%) to the hydrogen column by molecular hydrogen (Lockman 2004). Furthermore, fitting $N_{\rm H}$ along with other parameters in our temperature mapping suggests that there may be a gradient with magnitude of a few times 10^{20} cm^{-2} across the ACIS-I image. For the rest of the chapter we adopt the value of 8.33×10^{20} cm^{-2}, but readers should keep in mind that it is almost certainly too low.

The uncertainty of 0.2 keV given for the cluster temperature above includes only the statistical uncertainty from the spectral fit. We adopt a 1 σ uncertainty in $N_{\rm H}$ of $\sim 10^{20}$ cm^{-2}, which introduces a corresponding 0.5 keV uncertainty in the temperature. The background subtraction also affects the temperature. The Poisson uncertainty in the background scale factor determined using the 7–10 keV S2 spectrum is $\sim$4%, corresponding to a 0.2 keV uncertainty in the cluster temperature. In addition, the background scaling using the 7–10 keV band produces a cluster temperature that is 0.3 keV higher than that when scaling the background using the 10–12 keV band; thus, we adopt a temperature uncertainty contribution from the background scaling of 0.3 keV. Combining our three sources of uncertainty (statistical, $N_{\rm H}$, and background scaling), we arrive at a cluster temperature and uncertainty of 11.8 ± 0.6 keV. It should be noted that hydrogen column density uncertainties are not included in temperature uncertainties in the rest of the chapter unless explicitly noted.

Because X-ray point sources are visible in the *Chandra* data that were not noticeable in previous observations, it is possible that their presence could have affected previous temperature measurements. To check this, we also fit the entire cluster spectrum without removing point sources; this produces a temperature decrease of less than 0.1 keV.

Our measured value of $T_{\rm X} = 11.8 \pm 0.6$ keV is somewhat higher than previous temperature measurements;

our abundance value of 0.19 ± 0.03 is low in comparison to previous studies, though abundances in this range appear to be typical in studies of merging clusters (De Grandi & Molendi 2001). The discrepancy between our temperature measurement and previously published temperatures may be partially explained by *Chandra*'s relatively small field of view and the large angular extension of A2319. As is clear from Figure 2.1, there is significant cluster emission outside of the ACIS-I field. Using the PSPC image, we found that $\sim 30\%$ of the cluster emission in the 0.5–2.0 keV band lies outside of our ACIS-I observation. A MEKAL model fit on the S2 chip (excluding point sources) gives a temperature of 7.1 ± 1.2 keV ($\chi^2 = 214$ for 204 d.o.f.). This value is in agreement with *ASCA* measurements of 6–9 keV in large regions around and including the area covered by our S2 observation (Markevitch 1996). If the bulk of the gas outside the ACIS-I field is similarly cooler than our measured average temperature of the cluster, then our temperature measurement with *Chandra* would naturally be higher than measurements with previous–generation, larger field of view instruments. This effect probably does not account for the entire difference between our result and others, because measurement of temperatures within small regions of the ACIS-I chip give slightly higher-than-expected results as well, as is discussed in §2.2.3.

If a higher value for $N_{\rm H}$ were used, as discussed above, our fit temperature would be lower. This cannot account for the discrepancy between our results and previously published measurements, however, as previous studies have used column densities within $\sim 0.5 \times 10^{20}$ cm^{-2} of our adopted value.

The cluster temperature fit is sensitive to the choice of energy band. For example, fitting the entire cluster spectrum (with abundance and hydrogen column density allowed to vary) in the 0.9–10.0 keV band gives $T_{\rm X} = 10.6 \pm 0.3$ keV ($\chi^2 = 999$ for 593 d.o.f.); however, fitting between 1.7–10.0 keV gives $T_{\rm X} = 6.2 \pm 0.2$ keV ($\chi^2 = 705$ for 559 d.o.f.), and fitting between 2.0–10.0 keV gives $T_{\rm X} = 7.6 \pm 0.4$ keV ($\chi^2 = 576$ for 523 d.o.f.). While the specific behavior will vary by instrument, it should be noted that the lower energy limit of most previous temperature measurements has been $\sim$1.5–2.0 keV. One obvious explanation for the extreme dependence of spectral fitting on energy band is simply that the cluster is not isothermal, as we show in §2.2.3.

2.2.3 Temperature Structure

Chandra provides the means to perform a much more detailed study of the temperature structure of A2319 than previous instruments, permitting inspection of the cluster merger features. To this end we have made an X-ray temperature map of A2319 using the ACIS-I data. The map was created by measuring the temperature at each point on a grid, using a circular region enlarged until it contained 2000 counts in the 0.9–2.0 keV energy range. The regions overlap slightly at the center, and increasingly toward the edge; hence the pixels

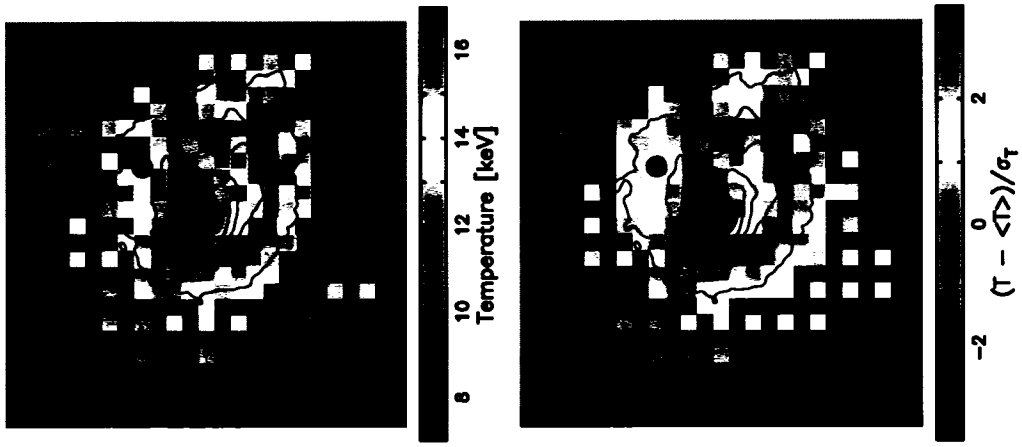

Figure 2.4 — X-ray temperature map (*left*), and significance map (*right*). The contours are from the 0.5–5 keV energy band image shown in Figure 2.2 after smoothing with a Gaussian of constant size, and are spaced at 10% of peak cluster intensity. Temperature pixels are 1′ (66 kpc) on a side. The average temperature $\langle T \rangle = 11.8$ keV, and uncertainties in this average temperature are not included in the significance map.

are not independent of one another. In the faint regions of the observation, where fitting region radii are larger than two pixel widths, only one pixel in four is measured. The spectra at each point were calculated using the same procedure as for the whole cluster spectrum described in §2.2.2, with abundance floating and $N_{\rm H} = 8.33 \times 10^{20}$ cm^{-2}. The abundance was left as a free parameter as abundances are known to vary in merging systems; fixing it to the cluster average produces temperature changes of $< 1\sigma$ across the temperature map.

The temperature map is shown in Figure 2.4 (*left panel*) with overlaid surface brightness contours. Also in Figure 2.4 (*right panel*) is a map of the significance of deviations from the mean temperature; that is, the difference between each pixel temperature and our adopted cluster mean temperature of 11.8 keV, divided by the uncertainty in the pixel temperature. The general structure of the temperature map includes two cooler-than-average regions that lie along a northwest–southeast line, and possibly two hotter-than-average regions that lie to the northeast and southwest of center. This temperature morphology is suggestive of a merger along a northwest–southeast trajectory, where remnants of cold cores remain and shock heated gas is escaping perpendicular to this merger axis, as seen in hydrodynamical simulations (Roettiger et al. 1997; Ricker & Sarazin 2001). The cold spots deviate from the mean by $> 2\sigma$; the hot spots are somewhat less significant. The very high ($\gtrsim 15$ keV) temperature regions lie where the cluster surface brightness is lowest, making these temperatures particularly susceptible to background subtraction errors. Overall, temperatures are higher than would be expected based on previous studies of A2319 (Markevitch 1996). Regardless of any overall temperature increase, the nonisothermality of the cluster provides some indication as to the origin

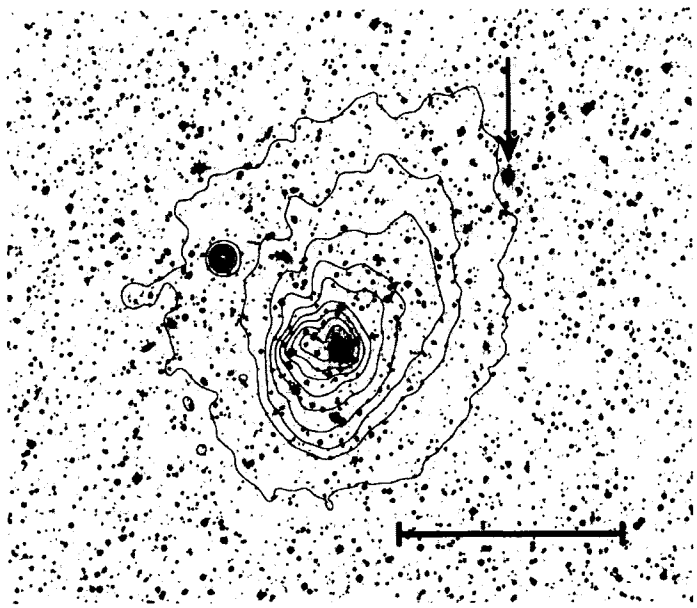

Figure 2.5 — V-band image from the Digitized Sky Survey with *Chandra* observation overlaid. Contours are the same as in Figure 2.4. The central (i.e., brightest) galaxy of A2319B is indicated with an arrow. The bar indicates a distance of 0.5 Mpc.

of the poor fit discussed in §2.2.2.

The level of substructure revealed here is more detailed than has been previously seen. The coolest region lies just south of the surface brightness peak, perhaps indicating a cool core that has thus far survived the ongoing merger. It is not immediately obvious from this map whether there is a sharp temperature change across the merger feature significant enough to deduce the existence of either a shock front or a cold front; we examine this in more detail in §2.3.1.

This cool core has not been identified in the earlier *ASCA* temperature map (Markevitch 1996). It seems likely that surrounding areas of higher-than-average temperatures obscured the core in the lower angular resolution *ASCA* map. Molendi et al. (1999) pointed out a "subcluster" of temperature 6.9 ± 1.0 keV to the northwest of the cluster center, and there is evidence for the presence of this cool region in the temperature map of Markevitch (1996). This subcluster is seen here $\sim 6'$ northwest of the X-ray brightness peak, although at a somewhat higher temperature. Also present is a distinct region of somewhat elevated (i.e., above the mean) temperatures between this subcluster and the cool center.

The cool ICM "subcluster" has been identified with subcluster A2319B; however, at this resolution it is clear that the cool region is not associated with the center of A2319B, but rather lies 2–3′ to the east-southeast of it, as can be seen by comparing the temperature map to the visual-band image shown in Figure 2.5. This suggests that the subcluster is in a transient phase wherein the ICM has decoupled from

the galaxies. Such a state has been observed in other merging clusters such as 1E0657-56 (Markevitch et al. 2002) A754 (Zabludoff & Zaritsky 1995; Markevitch et al. 2003), Cl J0152.7–1357 (Maughan et al. 2003), and A2034 (Kempner et al. 2003).

Overall, the temperature map reveals complex substructure of the type now known to occur in galaxy cluster mergers. Such substructure is also seen in hydrodynamical simulations (e.g. Roettiger et al. 1997; Onuora et al. 2003)

2.3 Merger Analysis

We present here a simple analysis of the merger features in A2319, wherein we assume a simple spheroidal geometry for an isothermal body of gas falling into a relaxed β-model cluster. This is what might be termed the "traditional" analysis of a merging cluster (following Vikhlinin et al. 2001). However, numerical simulations of clusters (e.g., Ricker & Sarazin 2001; Bialek et al. 2002; Nagai & Kravtsov 2003; Onuora et al. 2003) have made it clear that the dynamics within a mid-stage merger are much more complex than this. Nevertheless, this naive analysis offers some level of quantitative information about the nature of the merger front, and permits comparison to other merger analyses.

2.3.1 Temperature and Brightness Profiles Across Merger Feature

We measure the surface brightness and temperature profiles across the merger feature (see Figure 2.6). The brightness is measured in arcs on a wedge, chosen with a radius of curvature and angular width that match the brightness discontinuity reasonably well. We then measure the temperature, making spectra as previously described, in arc segments of sizes chosen both to provide a sufficient number of photons and to permit study of temperature variation across the front; we select the segment boundaries to avoid having a region straddling the surface brightness discontinuity. Note that this is not a cluster radial profile; the wedge in which this is measured is chosen to match the brightness discontinuity, and is not centered on the brightness peak.

While there is clearly a brightness change, this change is not as sharp as those seen in merging clusters such as A3667 (Vikhlinin et al. 2001). This can be readily explained if the merger is not taking place close to perpendicular to the line of sight; indeed, the aforementioned difference in line-of-sight velocity between A2319A and A2319B of $\sim$ 2900 km s^{-1} (Oegerle et al. 1995) suggests that we are viewing the merger at some large angle. This introduces substantial uncertainties into the analysis below.

If we assume that the infalling gas body is a spheroid with constant gas density, then the surface brightness

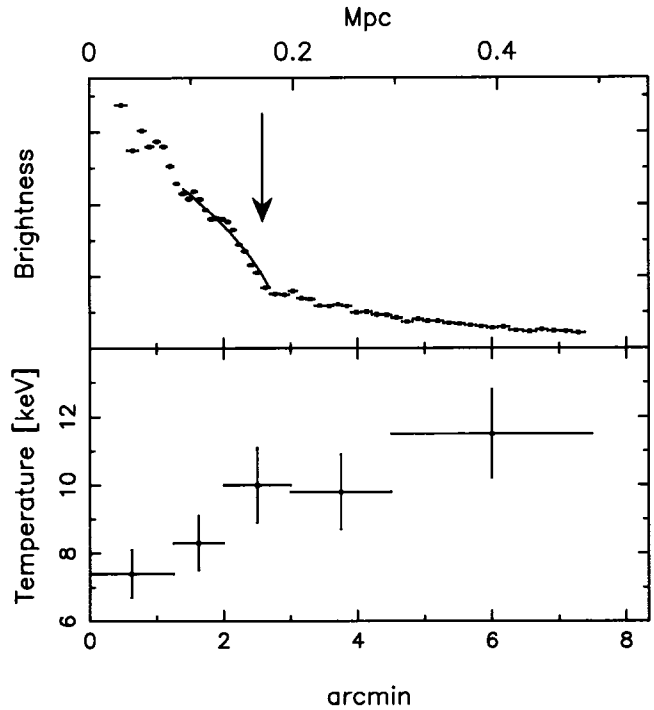

Figure 2.6 — Brightness (in arbitrary units) and temperature profiles across the merger feature. The arrow indicates the approximate position of the brightness discontinuity seen in Figure 2.2. A fit to the surface brightness inside the merger feature using Equation 2.2 is shown by the solid line.

profile at distances from the front much less than the major axis of the spheroid will be given by

$$S(d) = 2^{3/2}\sqrt{R}\varepsilon_0\sqrt{d}\,, \tag{2.1}$$

where R is the radius of curvature at the front, ε_0 is the volume emissivity of the gas, and d is the distance from the front (Vikhlinin et al. 2001). This function adequately describes the surface brightness profile of our data in the region just inside the front (i.e., the region between roughly 1.5–2.8′ in Figure 2.6).

More precisely, the surface brightness profile is

$$S(d) \simeq 2a\varepsilon_0 \left(\frac{2d}{b} - \frac{d^2}{b^2}\right)^{1/2} \left(1 - \frac{d}{b}\right)^{-3.45\beta} \tag{2.2}$$

for $|\beta| < 0.25$, where a and b are the short and long axes of the spheroid, respectively (Vikhlinin et al. 2001). Fitting this function to the brightness profile just interior to the front gives $\beta \lesssim 0.1$. Our approximation of constant density inside the front is thus justified.

An examination of Figure 2.6 does not conclusively determine the nature of the merger feature, i.e., whether it is a shock front or cold front. The temperature just inside the merger is 9.0 ± 0.9 keV, while the

temperature just outside is 10.8 ± 1.3 keV. This suggests that the feature is a cold front, but the temperature uncertainties are large. The temperature falls by another 1–2 keV deeper inside the infalling subcluster.

To rule out significant upward biasing of temperatures inside the front by projected hotter gas in front of and behind the cooler gas, we fit a two-component MEKAL model to a region inside the front, near the brightness discontinuity, with the hotter component fixed to the temperature measured outside the discontinuity. We find that to measure a cool component temperature that is 1 σ lower than the single-component temperature measurement requires a hot component contribution of $\gtrsim 40\%$ of the emission. As this seems unreasonably high, we conclude that our temperature measurements inside the front are not significantly biased by projected hotter gas.

2.3.2 Density Variation Across Merger Feature

In general, the intensity of a body of gas at constant temperature is

$$I = \frac{1}{(1+z)^4} \int n_e n_H \Lambda(T_X, l)\, dl \ , \tag{2.3}$$

where $\Lambda(T_X, l)$ is the emissivity of the gas and the length element dl is along the line of sight; the integration is carried out over the entire body along the line of sight.

If the spheroid's long axis is much larger than the minor axes, we can model the infalling subcluster as a "bullet" of width L; we assume a constant temperature and intensity. Using these assumptions in equation (2.3) and solving for the electron density gives

$$n_e = \left(\frac{I}{L\Lambda(T_X)} \frac{\mu_e}{\mu_H} \right)^{1/2} (1+z)^2 \ . \tag{2.4}$$

We use $\mu_e = 1.67$ and $\mu_H = 1.4$, the values for a fully ionized gas of one-third solar abundance. Using estimated values for I and L, we obtain an electron density immediately inside the merger front of $(6.0 \pm 1.0) \times 10^{-3}$ cm^{-3}.

To get the electron density outside the front, we assume that the gas fits a spherical β-model density profile:

$$n_e = n_{e_0} \left(1 + \left(\frac{\theta}{\theta_c} \right)^2 \right)^{-3\beta/2} \ , \tag{2.5}$$

with central electron density n_{e_0} and critical radius θ_c. That is, we assume that the gas to the southeast of the front is part of the original relaxed cluster into which a subcluster is falling, and is thus far unperturbed

by the merger. To get values for β and θ_c, we fit the surface brightness in our wedge, outside the merger. We arrive at an electron density immediately outside the merger feature of $(2.0 \pm 0.6) \times 10^{-3}$ cm^{-3}, or roughly one-third the density immediately inside the feature.

These densities correspond to pressures ($p = n_e T_X$) inside of $p_{in} = (5.4 \pm 1.0) \times 10^{-2}$ keV cm^{-3} and outside of $p_{out} = (2.2 \pm 0.7) \times 10^{-2}$ keV cm^{-3}. Using the relationships between these pressures and the Mach number M of the infalling gas cloud (where $M = v/c_{out}$ is the Mach number in the free stream outside the merger) gives $M = 1.1 \pm 0.3$ (see §122; Landau & Lifshitz 1987). The infalling cluster would thus probably be moving at a roughly sonic speed if indeed the merger were taking place in the plane of the sky, as we have assumed for this analysis. Because of the line of sight velocity difference of the galaxies associated with A2319A and A2319B, we expect that the merger axis does not lie in the plane of the sky.

2.3.3 Toward a Cluster Dynamical Model

Combining the results of the previous sections, we present the following picture of the merger in A2319. There is a jump by a factor of 3.0 ± 1.0 in the density of the gas as one crosses the brightness discontinuity from the unperturbed gas outside the merger towards the cluster core. This is accompanied by a slight temperature decrease of 1–3 keV, and a brightness increase by a factor of ~ 3; the combined densities and temperatures give a pressure jump by a factor of 2.5 ± 0.9. These results indicate the presence of a cold front, although the temperature difference across the front is not as large as is observed in, e.g., A3667 (Vikhlinin et al. 2001).

However, we have assumed for this analysis that the infalling subcluster is moving in the plane of the sky; our value for the electron density in the cool core is thus an overestimate given the known line-of-sight velocity difference between A2319A and A2319B that indicates that bulk gas motions are not perpendicular to the line of sight. This is most easily seen by examining equation 2.4; if the subcluster is not oriented perpendicular to the line of sight, then we are overestimating the X-ray intensity I, and hence also the electron density n_e. Moreover, if this merger has a nonzero impact parameter, then our estimate for the ambient electron density, i.e., the density outside the merger feature, is likewise an overestimate. It is thus possible that the inside/outside density and pressure ratios are in fact lower or, less likely, higher than the values given. This does not change the general interpretation of the merger feature as a cold front; the temperature change is indisputable, and the uncertainties in density are not large enough to accommodate a pressure outside the front greater than that inside the front.

The simplest interpretation for the merger geometry seen in A2319 is that A2319B has recently fallen through A2319A, in the process losing much of its ICM as indicated by the low X-ray brightness around the

giant elliptical that dominates its galaxy population. The separation of the cold spot near A2319B from its galaxies supports this (see Figures 2.4 & 2.5). However, the structure of the cold front suggests motion away from A2319B. We suggest that the encounter of the two subclusters of A2319 has caused the cool core of A2319A to be displaced from its position at the center of the subcluster, and that this core is now recoiling from that displacement and has passed its original, central position. This is supported by the fact that the coldest part of A2319A's core is located slightly to the southeast of the brightest cluster galaxy. The merger feature is then a result of the interaction of the dense core ICM with less dense, warmer ICM surrounding the core.

The apparent survival in some form of the cold core ICM of A2319B may indicate a non-zero impact parameter. Given this and the relative sizes of the two subclusters, displacement of the core of A2319A to the point of creating motion of the core at near-sonic speeds would require a large infall velocity. It is also possible that the merger was essentially head–on, and that cool ICM spatially associated with the galaxies of A2319B is not from the original core of the subcluster, but was pulled from the core ICM of A2319A during the collision (see Pearce et al. 1994).

We estimate the timescale since closest approach of the two subclusters by constructing a simple, two-body dynamical model. Using the line of sight velocity dispersion of A2319A ($\sigma_A = 1324$ km s^{-1}, Oegerle et al. 1995), we obtain a crude estimate of the collision infall velocity of $\sqrt{6}\sigma_A = 3243$ km s^{-1} (this assumes infall from infinity). Combined with the measured line-of-sight velocity difference of subclusters A and B (2909 km s^{-1} Oegerle et al. 1995), we estimate that the merger trajectory has an angle of $\sim$65° out of the plane of the sky. The corresponding velocity in the plane of the sky is $\sim$1430 km s^{-1}. This gives a time since closest approach of the subcluster cores of $\sim$0.4 Gyr.

We emphasize that this is only one possible merger scenario. It does not include the possibility of a second merger event taking place along the northeast-southwest direction such as that suggested by an analysis of earlier X-ray data (Feretti et al. 1997).

2.4 Cluster Observables During a Major Merger

The merger signatures in A2319 are clear. These include significant centroid shifting in the *Einstein* IPC (Mohr et al. 1995) and *ROSAT* PSPC X-ray images; two subclusters identified in the optical (Faber & Dressler 1977; Oegerle et al. 1995); differing distributions of galaxies and ICM; and a surface brightness discontinuity and temperature structure in the *Chandra* data. We seek now to examine how mergers perturb the global physical structure of clusters. We address this empirically by simply examining how particular

bulk properties of A2319 (binding mass, ICM mass, isophotal size, luminosity, emission weighted mean temperature, and galaxy light) compare to typical galaxy clusters. Specifically, we compare the properties of A2319 to what is essentially a flux-limited ensemble of 44 galaxy clusters from the nearby universe (Mohr et al. 1999). While the high resolution of *Chandra* is not necessary for this, the *Chandra* observation nonetheless provides another high-quality data set for such study.

The question of how much merging perturbs the global structure of galaxy clusters is particularly important in light of the planned and ongoing high-yield galaxy cluster surveys. In these surveys, rather simple observables like the SZE flux, X-ray flux, and galaxy light will be used to estimate cluster masses for studies of the dark energy (e.g., Haiman et al. 2001). Even though it has recently been shown that very large surveys contain enough information to self–calibrate while precisely constraining the dark energy (Majumdar & Mohr 2003, 2004; Hu 2003), any improvements in our understanding of cluster mass–observable relations, their evolution, and the effects of merging on them will lead to tighter limits on systematic uncertainties in the resulting cosmological constraints.

2.4.1 Naive Analysis of Mass Profile

We obtain a naive measure of M_{2500}, i.e., the mass enclosed by r_{2500}, the radius within which the mean density is 2500 times the critical density of the universe. Most cluster surveys focus on properties at larger radii (e.g., r_{500}), but *Chandra*'s small field of view relative to the large angular extent of A2319 makes this impossible with a single pointing.

We assume that the cluster ICM density distribution is fit by a spherical β-model and that the ICM is in hydrostatic equilibrium; the binding mass within a radius r is then

$$M(r) = -\frac{k_B}{\mu m_p G} r T(r) \left(\frac{\partial \ln \rho_{\rm gas}(r)}{\partial \ln r} + \frac{\partial \ln T(r)}{\partial \ln r} \right) . \tag{2.6}$$

Figure 2.7 contains a projected temperature profile of A2319, where the cluster center is that found by the β-model fit to the X-ray surface brightness (described below). There is no easily quantifiable variation of temperature as a function of distance from the cluster center. Given the measured density and temperature profile, r_{2500} lies mostly outside the ACIS-I image. To estimate the mass at this radius, we adopt an isothermal temperature profile and extract the average temperature from the outer three annuli in Figure 2.7. This temperature is 11.1 ± 0.9 keV, less than 1σ lower than the emission weighted mean temperature for the cluster.

A fit to the *Chandra* surface brightness image of A2319 gives core radius $r_c = 0.17 \pm 0.01$ Mpc ($\theta_c =$

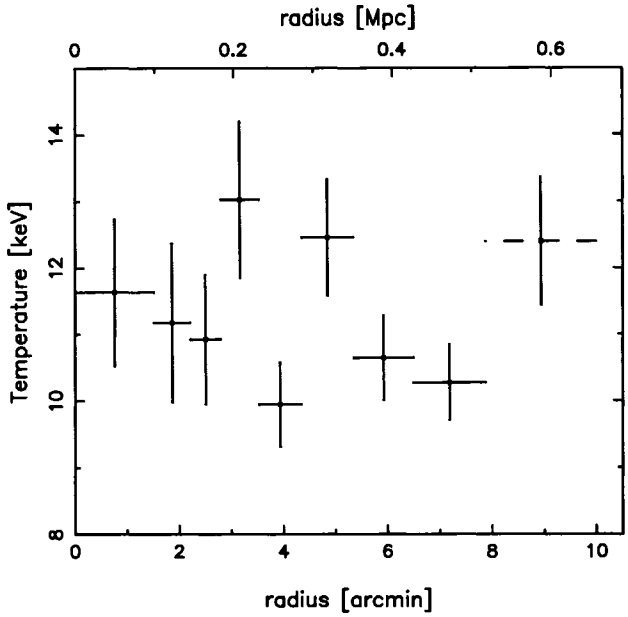

Figure 2.7 — Projected temperature profile created around the center of the cluster as found by a β-model fit, not around the surface brightness peak. The outermost annulus partially extends beyond the boundaries of the ACIS-I observation, and so we mark the angular extent of this annulus with a dashed line.

$2'.6 \pm 0'.1$) and $\beta = 0.55 \pm 0.01$ (compared to $r_c = 0.15 \pm 0.05$ Mpc and $\beta = 0.54 \pm 0.06$ from the analysis of the PSPC image; Mohr et al. 1999). With these values and equation (2.6), we find $r_{2500} = 0.67 \pm 0.02$ Mpc ($\theta_{2500} = 10'.2 \pm 0'.4$) and binding mass $M_{2500} = (4.2 \pm 0.5) \times 10^{14}\ M_\odot$. The uncertainties quoted here for the β-model fit are 1 σ statistical uncertainties only, and do not reflect the fact that the β model is not a particularly good fit to the surface brightness in this complex cluster. The mass uncertainty is dominated by the uncertainty in the temperature measurement.

We compare this mass estimate to that expected for a cluster with this emission-weighted mean temperature, using an M_{2500}-T_X relation derived from a sample of seven intermediate-redshift clusters (Allen et al. 2001). For our cluster temperature of $T_X = 11.8 \pm 0.6$ keV the best fit relation gives $M_{2500} = (6.7 \pm 0.8) \times 10^{14} M_\odot$, which is a factor of 1.6 ± 0.3 higher than our value. In this merging cluster, the hydrostatic equilibrium assumption and spherical β-model fitting thus lead to a mass estimate that lies $\sim 60\%$ off the relation found in apparently "relaxed" clusters. The Allen et al. (2001) sample is too small to make meaningful statements about the scatter, but other analyses of much larger samples show scatter at roughly the 25% level (Finoguenov et al. 2001).

2.4.2 Comparison of A2319 to Large Cluster Sample

We examine five bulk properties of A2319—the X-ray luminosity, emission-weighted mean temperature, ICM mass, isophotal size, and K-band galaxy light—and compare these properties to the same properties for large samples of galaxy clusters. In the case of all but the galaxy light we use an ensemble of 44 clusters studied using the *ROSAT* PSPC (Mohr & Evrard 1997; Mohr et al. 1999, 2000), but reanalyzed at the cluster radius r_{2500}. For each cluster we determine r_{2500} using the emission weighted mean temperature and the published M_{2500}–temperature relation (Allen et al. 2001). For the PSPC sample, exposure corrected, background subtracted images were prepared in the rest frame 0.5–2.0 keV band for each cluster. In the case of the galaxy light, we compare to an ensemble of ∼100 clusters whose properties are being studied using X-ray data and 2MASS near-IR data (Lin et al. 2003).

We measure $L_{X,2500}$, the X-ray luminosity projected within a circle of radius r_{2500} in the 0.5–2.0 keV band. As a result of the uncertainty of the spectral response of *Chandra* below ∼0.9 keV, for our observation of A2319 we measure the flux (and thus luminosity) in an image that includes only counts in the 0.9–2.0 keV band. With the emission-weighted mean temperature, we calculate the conversion between the count rate in this band and the flux within the rest frame 0.5–2.0 keV band. Another difficulty is that we find $\theta_{2500} = 11'.8$ from the Allen et al. (2001) M_{2500}-T_X relation, slightly too large to fit within the ACIS-I observation. However, the low luminosity near the edges, relative to the central luminosity, means that our value $L_{X,2500} = 5.2 \times 10^{44}$ erg s^{-1} contains the bulk of $L_{X,2500}$. Indeed, using the *Chandra* footprint on the *ROSAT* PSPC image, we find that 15% of the flux within r_{2500} is missed; thus, our corrected estimate of the luminosity in the 0.5–2.0 keV band is $L_{X,2500} = 6.0 \times 10^{44}$ erg s^{-1}. This is high by ∼18% compared to the value $L_{X,2500} = 5.1 \times 10^{44}$ erg s^{-1} measured using the PSPC image. The top panel of Figure 2.8 contains the *ROSAT* sample (small points) with best fit power law together with the *Chandra* measurement (large point). The luminosity is low by 54% relative to the expectation for a cluster with a temperature of 11.8 keV, compared to an RMS fractional scatter about the best fit relation of 57% (the PSPC value for $L_{X,2500}$ is low by $\sim 61\%$).

We measure the ICM mass within r_{2500} using a measurement of the flux from the cluster combined with the β-model fit parameters and our cluster temperature of 11.8 keV. The count rate emissivity of a parcel of gas within the 0.5–2.0 keV band has low sensitivity to temperature variations and, assuming that all the ICM is emitting at the emission weighted mean temperature, provides a good estimate of the ICM mass (see Fabricant et al. 1980; Mohr et al. 1999). The ICM mass from the *Chandra* analysis is $M_{ICM,2500} = 6.9 \times 10^{13} M_\odot$, corresponding to an ICM mass fraction of $f_{ICM,2500} = 16\%$. The corresponding value from the PSPC analysis is $M_{ICM,2500} = 5.2 \times 10^{13} M_\odot$, roughly 30% lower. The middle panel of

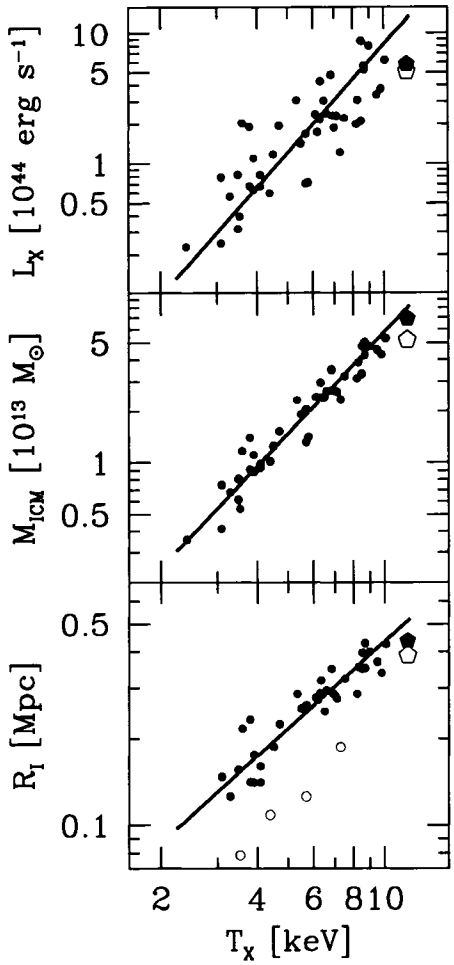

Figure 2.8 — Scaling relations for the sample of *ROSAT* PSPC observations from Mohr et al. (1999) (circles), plus our measurements for A2319 (*Chandra* solid pentagon; PSPC open pentagon), using a temperature of 11.8 keV. Best fits to the PSPC sample are shown as lines. *Top*: $L_{X,2500}$ in the 0.5–2.0 keV band. *Middle*: M_{ICM} within r_{2500}. *Bottom*: Isophotal size for an isophote of 1.53×10^{-13} erg s^{-1} cm^{-2} arcmin^{-2} in the 0.5–2.0 keV band. Open points mark clusters that were excluded from the fit, as the use of a very high isophote caused them to give erroneous results.

Figure 2.8 contains the *ROSAT* sample (small points) with best fit power law together with the *Chandra* measurement (large point). The ICM mass is low by $\sim 14\%$ relative to the expectation for a cluster with a temperature of 11.8 keV, compared to an RMS fractional scatter about the best fit relation of 20% (the PSPC value for the ICM mass is low by $\sim 35\%$).

We measure the isophotal size R_I for A2319 at an isophote of 1.53×10^{-13} erg s^{-1} cm^{-2} arcmin^{-2} in the 0.5–2.0 keV band. This isophote is chosen so that the isophotal size is not affected by the limited field of view of the *Chandra* footprint. We measure the size using the area A_I enclosed by this isophote, and find an equivalent radius from $A_I = \pi R_I^2$. For the *Chandra* observation we obtain $R_I = 0.44$ Mpc, compared to the value $R_I = 0.39$ Mpc obtained when using the PSPC image. The bottom panel of Figure 2.8 contains the

ROSAT sample (small points) with best-fit power law together with the *Chandra* measurement (large point). Note that at an isophote this bright there are several clusters that simply fall off the relation defined by the bulk of the PSPC clusters. We are forced to use such a bright isophote because the *Chandra* footprint is so small compared to the angular extent of A2319. Nevertheless, A2319's isophotal size is ~14% lower than that expected for a cluster with its emission weighted mean temperature, compared to an RMS fractional scatter about the best fit relation of 14% (the PSPC value for R_I is low by $\sim 24\%$).

Interestingly, A2319 does not stand out significantly from the sample of 44 clusters (essentially an X-ray flux-limited sample) studied with the *ROSAT* PSPC. The merger in A2319 does not perturb the cluster significantly in luminosity, ICM mass, or isophotal size from the values expected for a cluster with its emission weighted mean temperature. In addition, an analysis of the galaxy light in the K-band that is projected within r_{500} in A2319 leads to an estimate of the cluster K-band light that is 14% higher than expected for a cluster with a 11.8 keV temperature, when compared to a sample of ~100 clusters where the rms scatter is 30% (Lin et al. 2003).

One possible explanation is that the merger event is relatively minor (the ratio of velocity dispersions of A2319A and A2319B suggests a mass ratio of ~8), but it may also be that merging clusters are perturbed in all their quantities in such a way that they remain close to the population-defined scaling relations. In fact, it should be noted that many of the clusters contained in the PSPC sample exhibit evidence for ongoing mergers (Mohr et al. 1995; Buote & Tsai 1996). We cannot hope to deliver a final verdict on the effects of merging on the bulk properties of clusters with studies of single clusters; however, our results do provide some evidence that bulk properties either do not change much as a result of mergers, or change in a correlated way that maintains the strikingly small scatter of scaling relations.

Correlated changes in luminosity and temperature within merging clusters have been examined with numerical simulations. Ricker & Sarazin (2001) measured the luminosity and temperature boosts in merging cluster systems as a function of time. If we assume a 1:3 mass ratio for the subclusters, then the simulations predict a peak luminosity boost by a factor of ~2–4, along with a peak temperature boost of a factor of ~1.5–2.0, with correspondingly smaller boosts associated with larger mass ratio mergers. Simultaneous boosts to the luminosity and temperature of these magnitudes would not make A2319 stand out in the luminosity–temperature relation in Figure 2.8. However, A2319 appears "normal" with respect to its luminosity–temperature, isophotal size–temperature, ICM mass–temperature and galaxy light–temperature properties. It would seem to be contrived to claim that large, merger related excursions in these five bulk properties of the cluster all take place in just such a way as to keep the cluster near the observed, typical behavior for a large sample of clusters. A simpler explanation would appear to be that these five cluster properties are

simply not dramatically affected by the merger taking place in A2319.

2.5 Conclusions

Using *Chandra* data, we have identified and studied a major merger event in A2319 that appears to be taking place along the axis connecting its two major optical subclusters. The X-ray brightness map shows a clear discontinuity that appears similar to cold fronts found in other clusters. Although this cold front appears to be as large as the one studied in A3667 (Vikhlinin et al. 2002), it is not as sharp. This, together with previous measurements of the line of sight velocity difference between the two main optical subclusters (Oegerle et al. 1995), suggests that the merger is not taking place in the plane of the sky. We propose a merger model where the trajectory lies approximately 65° out of the plane of the sky, and at this viewing angle it becomes even more challenging to make quantitative statements about the ICM properties near the cold front. Nevertheless, we estimate that the pressure change across the front is $\lesssim 2.5$, and that the higher density ICM also has the lower temperature. The estimated merger Mach number of $\sim$1.1 is likewise consistent with other merging systems such as A3667. We propose a two body merger where A2319B merged from the southeast traveling northwest, with the A2319B galaxies and dark matter passing through the A2319A core roughly 0.4 Gyr ago.

The measured emission-weighted mean temperature of this messy, merging cluster is $T_{\rm X} = 11.8 \pm 0.6$ keV and the mean abundance is $Z = 0.19 \pm 0.03$, using a hydrogen column toward the cluster of $N_{\rm H} = 8.33 \times 10^{20}$ cm^{-2}. The fit values deviate somewhat from previous studies of A2319. Our higher temperature is likely due in part to the small field of view of *Chandra* compared with other instruments used to study this cluster. In addition, we have shown that the emission-weighted mean temperature depends sensitively on the choice of energy band, which is at least partly explained by the highly nonuniform temperature structure we have revealed in this cluster.

Our temperature map shows substructure now considered typical in merging systems. The cool core of A2319A is readily visible, and the angular separation of the galaxies of A2319B and an associated cool ICM region indicates a separation of the galaxies from the ICM of this subcluster, a transient phenomenon that gives further evidence of a merger event. There is some evidence for a hot bridge of ICM between the two cores, a characteristic associated with shock heating in mergers that has been seen in simulations.

We examine how this merger affects the bulk properties of A2319. We naively apply the hydrostatic equilibrium assumption to measure a total mass within r_{2500} of $M_{2500} = (4.2 \pm 0.5) \times 10^{14}\ M_{\odot}$, a factor of 1.6 ± 0.3 lower than the mass predicted by a mass–temperature relation derived from five intermediate-

redshift clusters (Allen et al. 2001). This offset is the strongest indication that the structure of A2319 has been significantly affected by the merger. Our measurements for L_X–temperature, M_{ICM}–temperature, and isophotal size–temperature are compared to a sample of 44 clusters observed with *ROSAT* PSPC (Mohr & Evrard 1997; Mohr et al. 1999, 2000). In all three cases our measured values for A2319 are within the scatter of the PSPC-derived scaling relations. In addition, we note that the K-band light in the A2319 galaxy population is consistent with that expected for a cluster of this emission weighted mean temperature (Lin et al. 2003). It is possible that changes in bulk parameters due to mergers are actually quite large but take place in a correlated way that maintain the low, observed scatter in cluster scaling relations; this has been shown for some properties in numerical simulations (Ricker & Sarazin 2001; Evrard & Gioia 2002). However, it will require further studies to determine whether it is possible for mergers to create large, correlated displacements in five cluster parameters (i.e., emission-weighted mean temperature, luminosity, isophotal size, ICM mass, and K-band galaxy light) that maintain the low scatter in all four scaling relations. Another possibility is that despite the X-ray imaging spectroscopy and optical evidence for an ongoing merger in A2319, a merger of this scale is simply not sufficient to grossly perturb the bulk properties of the cluster.

We thank Yen-Ting Lin for providing results of a near-infrared analysis of A2319 prior to publication, and an anonymous referee for helpful comments. This work made use of a Digitized Sky Survey image. The Digitized Sky Surveys were produced at the Space Telescope Science Institute under U.S. Government grant NAG W-2166.

Chapter 3

Effects of a Mergers and Core Structure on the Bulk Properties of Nearby Galaxy Clusters

We use X-ray morphological measurements and the scatter of clusters about observed and simulated scaling relations to examine the impact of merging and core-related phenomena on the structure of galaxy clusters.[1] We use a range of X-ray and near-infrared scaling relations; all observed scaling relations constructed from emission-weighted mean temperature and intracluster medium mass, X-ray luminosity, isophotal size, and near-IR luminosity show a separation between clusters identified as cool core (CC) and those identified as non-cool core (NCC). We attribute this partially to a simple temperature bias in CC clusters, and partially to other cool core-related structural changes. Scaling relations constructed from observables that are largely independent of core structure show smaller separation between CC and NCC populations. We attempt to minimize cool core-related separation in scaling relations via two methods: by applying a uniform scale factor to CC cluster temperatures and determining the scale factor for each relation that minimizes the separation between CC and NCC populations, and by introducing cluster central surface brightness as a third parameter in observable–temperature scaling relations. We find an average temperature bias factor of 1.07 ± 0.02 between the CC and NCC populations; the three parameter approach reduces scatter in scaling relations more than a simple CC temperature scaling.

We examine the scatter about the best-fit observable–temperature–brightness scaling relations, and compare the intrinsic scatter within subsamples split by CC/NCC and four different morphological merger indicators. CC clusters and clusters with *less* substructure generally exhibit higher scatter about scaling relations. The larger structural variations in CC clusters are present well outside the core, suggesting that a process more global than core radiative instability is at work. Simulations without cooling mechanisms also show no correlation between substructure and larger scatter about scaling relations, indicating that any merger-related scatter increases are subtle. Taken together, the observational and simulation results indicate that cool core related phenomena—not merging processes—are the primary contributor to scatter in scaling relations. Our analysis does not appear to support the scenario in which clusters evolve cool cores over time unless they experience major mergers.

[1]This work has been published as O'Hara, Mohr, Bialek, & Evrard 2006, ApJ, 639, 64.

3.1 Introduction

Galaxy clusters provide a setting for exploring the composition of the universe on large scales, and for studying the growth of structure. X-ray and Sunyaev-Zel'dovich effect surveys of large numbers of clusters will soon be used to study the nature of the dark energy. It is thus vitally important to understand cluster structure and its connections to observable, bulk properties of clusters.

Clusters exhibit strikingly regular power law scaling relations between such properties as emission-weighted mean temperature, intracluster medium (ICM) mass, binding mass, X-ray luminosity, isophotal size, and near-IR light (e.g., Mohr & Evrard 1997; Mohr et al. 1999; Vikhlinin et al. 2002; Lin et al. 2003). For relaxed, isolated systems this is expected, although even for isolated systems there should be some scatter at a given average temperature due to variations in formation epoch, gas fraction, and galaxy and star formation history.

However, clusters are in fact young, dynamic systems. There is evidence, much of it based on quantitative substructure measures, for merging in a significant fraction (>50%) of nearby clusters (e.g., Geller & Beers 1982; Dressler & Shectman 1988; Mohr et al. 1995; Buote & Tsai 1996). The advent of high-resolution X-ray instruments such as *Chandra* has made observation of the complex hydrodynamical structure of merging clusters possible, revealing and permitting detailed measurements of ICM properties around features such as "cold fronts" (Vikhlinin et al. 2001).

This dual nature of clusters—frequent merging on the one hand, and regular scaling relations on the other—is puzzling. The extreme energetics of merger events, in which $\sim 10^{63}$ erg of kinetic energy can be thermalized and cluster structure greatly disrupted, would suggest that cluster properties should not be correlated in such a simple way. One might expect to find a statistical correlation between the deviation of a particular cluster from a scaling relation and the substructure—an indication of merger activity—in that cluster.

Tight scaling relations are observed in simulations of clusters that evolve in a cosmological context (e.g., Evrard et al. 1996; Bryan & Norman 1998; Bialek et al. 2001). However, simulations of mergers of isolated, relaxed clusters suggest that merging clusters should exhibit massive boosts in cluster bulk parameters such as temperature and X-ray luminosity (Ricker & Sarazin 2001; Randall et al. 2002). While the simulations indicate that these boosts are correlated, it seems likely that a cluster involved in a major merger would stand out from scaling relations constructed from several observables simultaneously.

If the cool cores found in a large fraction of the cluster population are an expected outcome of cluster relaxation in the absence of merger activity (e.g., Ota et al. 2006), then we may expect "relaxed" clusters to display less structural variation than clusters recently involved in mergers. If, on the other hand, cool

core structure is linked to more fundamental properties of individual clusters, such as early-time entropy injection (McCarthy et al. 2004), then merger-related effects may be overshadowed. There is presently no consensus as to whether merger-related effects dominate the scatter in scaling relations (e.g., Smith et al. 2005), or are a minority contribution (e.g., Balogh et al. 2006).

In this chapter we study multiple scaling relations. One may envision surfaces of clusters in a hyperplane constructed from several observables, and imagine studying deviations from these relations in multiple dimensions. We begin by examining only two parameters at a time, largely due to the greater ease of visualizing and understanding the deviations. Later we combine these two-observable analyses to examine cluster departures from the population in the much higher-dimensionality space. Our hope is that by examining nine different X-ray and near-infrared observables, each of which represents a different integral over the structure of the ICM and galaxies, we will be able to discern even modest structural deviations and probe their relationship to merging and other cluster phenomena.

If, as expected, cluster mergers perturb crude observables—for example, producing erroneously high estimates of cluster mass—then this must be taken into account in surveys using clusters to study cosmology (e.g. Haiman et al. 2001; Hu 2003; Majumdar & Mohr 2003, 2004; Lima & Hu 2005). It is thus of great importance to understand the true effects of merging on cluster bulk properties. Positions on scaling relations have been examined for a few individual merging clusters, e.g., Cl J0152.7–1357 (Maughan et al. 2003) and A2319 (O'Hara et al. 2004), with no significant deviations found. Clearly, however, analysis of a larger sample of clusters is needed to make meaningful statements about the relationship between merger signatures and bulk properties. Such an undertaking is the subject of this chapter.

Scaling relations have already been used to study cluster structure; for example, by examining the the effects of structure on the slope of the relations (e.g., Evrard et al. 1996; Cavaliere et al. 1997; Mohr & Evrard 1997; Bialek et al. 2001). The trend in recent X-ray studies of clusters, however, has been toward detailed studies of clusters using high-resolution instruments such as *Chandra*, and correspondingly detailed simulations (e.g., Ricker & Sarazin 2001; Nagai & Kravtsov 2003; Onuora et al. 2003). These studies have uncovered many surprising aspects of cluster structure. There is still a need, though, for a clearer picture of the effects of merging on the entire cluster population. An analysis of populations of simulated clusters suggests that it will not be possible to isolate "undisturbed" or "relaxed" clusters in large samples over a range of redshifts, and so a better understanding of merger effects on cluster bulk properties and on the general population is required.

We present here a joint analysis of a flux-limited sample of 45 nearby clusters observed with the *ROSAT* PSPC and the Two Micron All Sky Survey (2MASS), and an ensemble of 45 simulated clusters evolved in a

cosmological context. We begin with the scaling relations from the observational sample in §3.2. In §3.3 we discuss the effects of cool cores in our sample. We discuss a method of correcting for cool core effects so that we can examine only structural, merger-related scatter. We discuss the use of peak surface brightness as an indication of cool core strength in §3.4. §3.5 reports the study of the relationship between displacement from scaling relations and substructure in both observed and simulated clusters. Finally, we list our conclusions in §3.6.

Throughout this chapter we assume a ΛCDM cosmology with $\Omega_M = 0.3$ and $\Omega_\Lambda = 0.7$, and use a Hubble parameter of $H_0 = 70\,h_{70}$ km s^{-1} Mpc^{-1}. All uncertainties are 68% confidence, or 1 σ.

3.2 Observed Scaling Relations

We study an ensemble of 45 members of the Edge et al. (1990) flux-limited sample, observed with *ROSAT* PSPC. We use the same reduced imaging data as Mohr et al. (1999) (hereafter MME). These data have a pixel scale of 14″.947, and an energy range of 0.5–2.0 keV. The resolution of PSPC is, of course, poorer than the current generation of X-ray instruments, but none of the observables we are measuring require higher resolution. For details of the reduction, see MME. For 34 of these clusters we also use measurements of K-band light from Lin et al. (2004); the reduction, measurements, and uncertainties are discussed therein.

We use previously published emission-weighted mean temperatures measured with *Ginga* and *ASCA*, except for A2244, where we use a temperature measured with the *Einstein* MPC. We use PSF-corrected, cluster X-ray peak surface brightness values from MME, but all other X-ray observable quantities are measured as part of this analysis. We divide the sample into cool core (CC) and non-cool core (NCC) clusters based on published central cooling times (Peres et al. 1998). We adopt the classification of Mohr & Evrard (1997) in which CC clusters are those with central cooling times at least 3σ below 7.1 Gyr (for $H_0 = 70$ km s^{-1} Mpc^{-1}; 10 Gyr for $H_0 = 50$ km s^{-1} Mpc^{-1}). By this measure our sample of 45 clusters contains 30 CC and 15 NCC clusters. Basic information about the sample, plus the measured observables, is given in Table 3.1

In this section we first examine the X-ray luminosity–temperature relation in detail as an example of the scaling relations we are using. We point out features that will be common to all relations and demonstrate that the source of scatter is true structural variation among clusters, not measurement uncertainties. We then present the remaining X-ray scaling relations and quantify their scatter as well. Finally, we present the near-IR luminosity–temperature relation and discuss the additional information available from the galaxy properties.

Table 3.1: PSPC Sample Information

Cluster	z	T_X (keV)	$M_{ICM,500}$ ($h_{70}^{-5/2}$ $M_\odot$)	$M_{ICM,2500}$ ($h_{70}^{-5/2}$ $M_\odot$)	R_{3E-14} (h_{70}^{-1} Mpc)	$R_{1.5E-13}$ (h_{70}^{-1} Mpc)	$L_{X,500}$ (h_{70}^{-2} $L_\odot$)	$L_{X,2500}$ (h_{70}^{-2} $L_\odot$)	$L_{XCS,500}$ (h_{70}^{-2} $L_\odot$)	$L_{NIR,500}$ (h_{70}^{-2} $L_\odot$)	CC	T_X Reference
A85	0.0521	$6.10^{0.12}_{0.12}$	$6.62^{0.11}_{0.11}$E13	$2.41^{0.04}_{0.04}$E13	$0.564^{0.003}_{0.003}$	$0.278^{0.001}_{0.001}$	$2.80^{0.03}_{0.03}$E44	$2.31^{0.01}_{0.01}$E44	$1.38^{0.03}_{0.03}$E44	$5.99^{0.06}_{0.06}$E12	×	9
A119	0.0444	$5.80^{0.36}_{0.36}$	$4.93^{0.16}_{0.16}$E13	$1.42^{0.05}_{0.05}$E13	$0.471^{0.004}_{0.004}$	...	$1.03^{0.03}_{0.03}$E44	$6.59^{0.08}_{0.08}$E43	$8.16^{0.24}_{0.24}$E43	$6.46^{0.07}_{0.07}$E12		9
A262	0.0163	$2.21^{0.03}_{0.03}$	$9.88^{0.31}_{0.31}$E12	$3.36^{0.10}_{0.10}$E12	$0.189^{0.002}_{0.002}$	...	$2.54^{0.09}_{0.09}$E43	$2.00^{0.03}_{0.03}$E43	$1.42^{0.09}_{0.09}$E43	$1.99^{0.07}_{0.07}$E12	×	13
A401	0.0748	$8.30^{0.31}_{0.31}$	$1.11^{0.03}_{0.03}$E14	$3.84^{0.10}_{0.10}$E13	$0.726^{0.005}_{0.005}$	$0.355^{0.001}_{0.001}$	$3.85^{0.05}_{0.05}$E44	$2.99^{0.02}_{0.02}$E44	$2.30^{0.03}_{0.03}$E44	...		9
A426	0.0179	$5.28^{0.03}_{0.03}$	$7.11^{0.16}_{0.16}$E13	$2.68^{0.06}_{0.06}$E13	$0.596^{0.009}_{0.009}$	$0.319^{0.001}_{0.001}$	...	$4.05^{0.02}_{0.02}$E44	...	$7.92^{0.06}_{0.06}$E12	×	13
A478	0.0882	$6.84^{0.13}_{0.13}$	$8.43^{0.17}_{0.17}$E13	$3.50^{0.07}_{0.07}$E13	$0.621^{0.003}_{0.003}$	$0.351^{0.000}_{0.000}$	$5.29^{0.04}_{0.04}$E44	$4.74^{0.03}_{0.03}$E44	$1.98^{0.02}_{0.02}$E44	$7.96^{0.09}_{0.09}$E12	×	7
A496	0.0331	$3.91^{0.04}_{0.04}$	$2.96^{0.05}_{0.05}$E13	$1.11^{0.02}_{0.02}$E13	$0.375^{0.004}_{0.004}$	$0.175^{0.000}_{0.000}$	$1.22^{0.02}_{0.02}$E44	$1.04^{0.01}_{0.01}$E44	$5.57^{0.21}_{0.21}$E43	$3.91^{0.05}_{0.05}$E12	×	2
A644	0.0711	$6.59^{0.10}_{0.10}$	$6.54^{0.20}_{0.20}$E13	$2.61^{0.08}_{0.08}$E13	$0.533^{0.002}_{0.002}$	$0.295^{0.000}_{0.000}$	$2.72^{0.03}_{0.03}$E44	$2.36^{0.02}_{0.02}$E44	$1.25^{0.02}_{0.02}$E44	$6.34^{0.06}_{0.06}$E12	×	2
A754	0.0542	$8.50^{0.30}_{0.30}$	$1.04^{0.11}_{0.11}$E14	$3.32^{0.34}_{0.34}$E13	$0.665^{0.003}_{0.003}$	$0.349^{0.001}_{0.001}$	$2.83^{0.04}_{0.04}$E44	$2.04^{0.01}_{0.01}$E44	$1.99^{0.03}_{0.03}$E44	$9.28^{0.05}_{0.05}$E12		5
A780	0.0565	$3.80^{0.12}_{0.12}$	$3.26^{0.05}_{0.05}$E13	$1.39^{0.02}_{0.02}$E13	$0.408^{0.001}_{0.001}$	$0.233^{0.001}_{0.001}$	$2.08^{0.02}_{0.02}$E44	$1.87^{0.01}_{0.01}$E44	$7.86^{0.14}_{0.14}$E43	$3.09^{0.02}_{0.02}$E12	×	9
A1060 ...	0.0124	$3.10^{0.12}_{0.12}$	$9.96^{0.37}_{0.37}$E12	$4.12^{0.15}_{0.15}$E12	$0.186^{0.002}_{0.002}$	...	...	$1.89^{0.06}_{0.06}$E43	...	$2.39^{0.06}_{0.06}$E12	×	12
A1367 ...	0.0214	$3.50^{0.11}_{0.11}$	$2.19^{0.05}_{0.05}$E13	$6.13^{0.14}_{0.14}$E12	$0.312^{0.002}_{0.002}$	...	$4.48^{0.15}_{0.15}$E43	$2.80^{0.04}_{0.04}$E43	$3.59^{0.14}_{0.14}$E43	$3.81^{0.05}_{0.05}$E12		2
A1651 ...	0.0846	$6.30^{0.30}_{0.30}$	$6.39^{0.17}_{0.17}$E13	$2.40^{0.06}_{0.06}$E13	$0.522^{0.003}_{0.003}$	$0.288^{0.000}_{0.000}$	$2.46^{0.05}_{0.05}$E44	$2.09^{0.03}_{0.03}$E44	$1.25^{0.03}_{0.03}$E44	$7.82^{0.05}_{0.05}$E12	×	9
A1656 ...	0.0231	$8.21^{0.10}_{0.10}$	$8.74^{0.40}_{0.40}$E13	$3.12^{0.14}_{0.14}$E13	$0.610^{0.006}_{0.006}$	$0.286^{0.001}_{0.001}$	$2.30^{0.06}_{0.06}$E44	$1.87^{0.01}_{0.01}$E44	$1.41^{0.06}_{0.06}$E44	$8.94^{0.05}_{0.05}$E12		6
A1689 ...	0.1840	$9.23^{0.17}_{0.17}$	$1.23^{0.03}_{0.03}$E14	$5.08^{0.14}_{0.14}$E13	$0.704^{0.006}_{0.006}$	$0.425^{0.000}_{0.000}$	$6.65^{0.09}_{0.09}$E44	$6.04^{0.07}_{0.07}$E44	$2.90^{0.05}_{0.05}$E44	...	×	11
A1795 ...	0.0622	$5.34^{0.07}_{0.07}$	$5.57^{0.07}_{0.07}$E13	$2.32^{0.03}_{0.03}$E13	$0.521^{0.003}_{0.003}$	$0.286^{0.001}_{0.001}$	$3.35^{0.03}_{0.03}$E44	$3.00^{0.01}_{0.01}$E44	$1.26^{0.02}_{0.02}$E44	$4.80^{0.04}_{0.04}$E12	×	2
A2029 ...	0.0766	$8.70^{0.18}_{0.18}$	$1.05^{0.02}_{0.02}$E14	$4.24^{0.07}_{0.07}$E13	$0.653^{0.008}_{0.008}$	$0.351^{0.001}_{0.001}$	$5.57^{0.09}_{0.09}$E44	$5.03^{0.03}_{0.03}$E44	$1.90^{0.08}_{0.08}$E44	$8.12^{0.06}_{0.06}$E12	×	9
A2052 ...	0.0353	$3.03^{0.04}_{0.04}$	$1.81^{0.04}_{0.04}$E13	$7.38^{0.16}_{0.16}$E12	$0.297^{0.003}_{0.003}$	$0.148^{0.000}_{0.000}$	$8.13^{0.26}_{0.26}$E43	$7.18^{0.09}_{0.09}$E43	$3.30^{0.24}_{0.24}$E43	$3.19^{0.05}_{0.05}$E12	×	13
A2063 ...	0.0355	$3.68^{0.07}_{0.07}$	$2.33^{0.05}_{0.05}$E13	$8.79^{0.20}_{0.20}$E12	$0.313^{0.004}_{0.004}$	$0.141^{0.001}_{0.001}$	$6.81^{0.35}_{0.35}$E43	$5.63^{0.10}_{0.10}$E43	$3.72^{0.33}_{0.33}$E43	$3.34^{0.04}_{0.04}$E12	×	4
A2142 ...	0.0894	$8.68^{0.12}_{0.12}$	$1.38^{0.01}_{0.01}$E14	$5.04^{0.04}_{0.04}$E13	$0.787^{0.004}_{0.004}$	$0.430^{0.001}_{0.001}$	$6.65^{0.05}_{0.05}$E44	$5.52^{0.03}_{0.03}$E44	$3.28^{0.04}_{0.04}$E44	$7.20^{0.09}_{0.09}$E12	×	2
A2199 ...	0.0299	$4.10^{0.05}_{0.05}$	$2.94^{0.02}_{0.02}$E13	$1.19^{0.01}_{0.01}$E13	$0.356^{0.002}_{0.002}$	$0.187^{0.000}_{0.000}$	$1.28^{0.01}_{0.01}$E44	$1.13^{0.00}_{0.00}$E44	$5.03^{0.14}_{0.14}$E43	$4.25^{0.04}_{0.04}$E12	×	4
A2204 ...	0.1524	$7.21^{0.25}_{0.25}$	$1.16^{0.06}_{0.06}$E14	$4.29^{0.22}_{0.22}$E13	$0.723^{0.013}_{0.013}$	$0.400^{0.002}_{0.002}$	$8.45^{0.16}_{0.16}$E44	$7.55^{0.11}_{0.11}$E44	$3.08^{0.10}_{0.10}$E44	...	×	13
A2244 ...	0.0970	$7.10^{2.40}_{1.50}$	$6.89^{0.98}_{0.98}$E13	$2.60^{0.37}_{0.37}$E13	$0.529^{0.002}_{0.002}$	$0.275^{0.001}_{0.001}$	$2.65^{0.07}_{0.07}$E44	$2.24^{0.05}_{0.05}$E44	$1.19^{0.03}_{0.03}$E44	...	×	2
A2255 ...	0.0809	$6.87^{0.20}_{0.20}$	$7.17^{0.14}_{0.14}$E13	$2.23^{0.04}_{0.04}$E13	$0.598^{0.003}_{0.003}$	...	$1.65^{0.03}_{0.03}$E44	$1.13^{0.01}_{0.01}$E44	$1.27^{0.02}_{0.02}$E44	$8.70^{0.08}_{0.08}$E12		13
A2256 ...	0.0581	$7.51^{0.11}_{0.11}$	$8.70^{0.20}_{0.20}$E13	$3.20^{0.07}_{0.07}$E13	$0.639^{0.003}_{0.003}$	$0.323^{0.000}_{0.000}$	$2.69^{0.04}_{0.04}$E44	$2.14^{0.01}_{0.01}$E44	$1.77^{0.03}_{0.03}$E44	$1.01^{0.00}_{0.00}$E13		2
A2319 ...	0.0555	$9.12^{0.09}_{0.09}$	$1.40^{0.04}_{0.04}$E14	$4.45^{0.13}_{0.13}$E13	$0.833^{0.010}_{0.010}$	$0.393^{0.001}_{0.001}$	$4.84^{0.09}_{0.09}$E44	$3.66^{0.04}_{0.04}$E44	$3.09^{0.08}_{0.08}$E44	$1.28^{0.00}_{0.00}$E13		1
A2597 ...	0.0852	$3.60^{0.12}_{0.12}$	$2.79^{0.15}_{0.15}$E13	$1.17^{0.06}_{0.06}$E13	$0.386^{0.002}_{0.002}$	$0.217^{0.000}_{0.000}$	$2.19^{0.03}_{0.03}$E44	$2.01^{0.03}_{0.03}$E44	$6.85^{0.13}_{0.13}$E43	...	×	9

Table 3.1, cont.

Cluster	z	T_X (keV)	$M_{ICM,500}$ ($h_{70}^{-5/2}$ $M_\odot$)	$M_{ICM,2500}$ ($h_{70}^{-5/2}$ $M_\odot$)	R_{3E-14} (h_{70}^{-1} Mpc)	$R_{1.5E-13}$ (h_{70}^{-1} Mpc)	$L_{X,500}$ (h_{70}^{-2} $L_\odot$)	$L_{X,2500}$ (h_{70}^{-2} $L_\odot$)	$L_{XCS,500}$ (h_{70}^{-2} $L_\odot$)	$L_{NIR,500}$ (h_{70}^{-2} $L_\odot$)	CC	T_X Reference
A3112...	0.0703	$4.70^{0.24}_{0.24}$	$4.05^{0.24}_{0.24}$E13	$1.53^{0.09}_{0.09}$E13	$0.417^{0.002}_{0.002}$	$0.225^{0.000}_{0.000}$	$2.17^{0.03}_{0.03}$E44	$1.91^{0.02}_{0.02}$E44	$7.86^{0.21}_{0.21}$E43	$4.11^{0.08}_{0.08}$E12	×	9
A3158...	0.0590	$5.77^{0.10}_{0.05}$	$5.49^{0.12}_{0.12}$E13	$1.97^{0.04}_{0.04}$E13	$0.513^{0.004}_{0.004}$	$0.255^{0.001}_{0.001}$	$1.77^{0.03}_{0.03}$E44	$1.39^{0.02}_{0.02}$E44	$1.11^{0.02}_{0.02}$E44	$6.89^{0.05}_{0.05}$E12		13
A3266...	0.0545	$7.70^{0.48}_{0.48}$	$8.41^{0.30}_{0.30}$E13	$2.79^{0.10}_{0.10}$E13	$0.663^{0.003}_{0.003}$	$0.273^{0.001}_{0.001}$	$2.43^{0.04}_{0.04}$E44	$1.83^{0.01}_{0.01}$E44	$1.71^{0.04}_{0.04}$E44	$8.38^{0.06}_{0.06}$E12		9
A3391...	0.0550	$5.70^{0.42}_{0.42}$	$4.21^{0.21}_{0.21}$E13	$1.31^{0.07}_{0.07}$E13	$0.403^{0.003}_{0.003}$	...	$8.99^{0.35}_{0.35}$E43	$6.34^{0.13}_{0.13}$E43	$6.22^{0.29}_{0.29}$E43	$5.84^{0.09}_{0.09}$E12		9
A3526...	0.0101	$3.54^{0.08}_{0.08}$	$1.52^{0.03}_{0.03}$E13	$5.39^{0.09}_{0.09}$E12	$0.227^{0.003}_{0.003}$	...	...	$3.22^{0.07}_{0.07}$E43	...	$3.66^{0.16}_{0.16}$E12	×	1
A3532...	0.0553	$4.58^{0.12}_{0.10}$	$3.23^{0.09}_{0.09}$E13	$1.04^{0.03}_{0.03}$E13	$0.380^{0.005}_{0.005}$	...	$7.66^{0.26}_{0.26}$E43	$5.49^{0.10}_{0.10}$E43	$5.40^{0.22}_{0.22}$E43	...		11
A3558...	0.0477	$5.70^{0.12}_{0.12}$	$6.32^{0.10}_{0.10}$E13	$2.04^{0.03}_{0.03}$E13	$0.575^{0.007}_{0.007}$	$0.261^{0.001}_{0.001}$	$2.16^{0.04}_{0.04}$E44	$1.59^{0.01}_{0.01}$E44	$1.43^{0.04}_{0.04}$E44	$1.11^{0.01}_{0.01}$E13		3
A3562...	0.0502	$5.16^{0.16}_{0.16}$	$3.66^{0.10}_{0.10}$E13	$1.11^{0.03}_{0.03}$E13	$0.385^{0.005}_{0.005}$	$0.141^{0.000}_{0.000}$	$9.97^{0.32}_{0.32}$E43	$6.77^{0.09}_{0.09}$E43	$6.58^{0.29}_{0.29}$E43	$3.56^{0.09}_{0.09}$E12	×	13
A3571...	0.0397	$6.90^{0.18}_{0.18}$	$7.19^{0.21}_{0.21}$E13	$2.66^{0.08}_{0.08}$E13	$0.549^{0.005}_{0.005}$	$0.287^{0.001}_{0.001}$	$2.60^{0.05}_{0.05}$E44	$2.20^{0.02}_{0.02}$E44	$1.29^{0.05}_{0.05}$E44	...	×	9
A3667...	0.0530	$7.00^{0.36}_{0.36}$	$8.57^{0.23}_{0.23}$E13	$2.62^{0.07}_{0.07}$E13	$0.720^{0.007}_{0.007}$	$0.283^{0.001}_{0.001}$	$2.66^{0.06}_{0.06}$E44	$1.78^{0.02}_{0.02}$E44	$1.88^{0.05}_{0.05}$E44	$8.65^{0.06}_{0.06}$E12		9
A4038...	0.0281	$3.15^{0.03}_{0.03}$	$1.84^{0.11}_{0.11}$E13	$6.58^{0.40}_{0.40}$E12	$0.271^{0.001}_{0.001}$	$0.126^{0.000}_{0.000}$	$6.13^{0.15}_{0.15}$E43	$5.24^{0.07}_{0.07}$E43	$2.72^{0.12}_{0.12}$E43	$2.85^{0.06}_{0.06}$E12	×	13
A4059...	0.0456	$4.10^{0.18}_{0.18}$	$2.69^{0.08}_{0.08}$E13	$9.80^{0.30}_{0.30}$E12	$0.335^{0.001}_{0.001}$	$0.160^{0.000}_{0.000}$	$9.02^{0.20}_{0.20}$E43	$7.77^{0.10}_{0.10}$E43	$4.07^{0.15}_{0.15}$E43	$3.12^{0.10}_{0.10}$E12	×	9
0745-19..	0.1028	$7.21^{0.11}_{0.11}$	$1.13^{0.02}_{0.02}$E14	$4.44^{0.09}_{0.09}$E13	$0.708^{0.006}_{0.006}$	$0.396^{0.001}_{0.001}$	$9.28^{0.11}_{0.11}$E44	$8.44^{0.09}_{0.09}$E44	$2.86^{0.05}_{0.05}$E44	...	×	13
AWM7..	0.0172	$3.90^{0.12}_{0.12}$	$2.26^{0.08}_{0.08}$E13	$8.80^{0.32}_{0.32}$E12	$0.314^{0.002}_{0.002}$	$0.141^{0.000}_{0.000}$	$6.56^{0.21}_{0.21}$E43	$5.77^{0.06}_{0.06}$E43	$3.18^{0.20}_{0.20}$E43	$2.90^{0.06}_{0.06}$E12	×	8
Cygnus A	0.0570	$6.50^{0.36}_{0.36}$	$7.54^{0.36}_{0.36}$E13	$2.39^{0.12}_{0.12}$E13	$0.657^{0.015}_{0.015}$	$0.249^{0.002}_{0.002}$	$3.53^{0.15}_{0.15}$E44	$2.69^{0.04}_{0.04}$E44	$1.64^{0.14}_{0.14}$E44	...	×	9
MKW3S.	0.0430	$3.50^{0.12}_{0.12}$	$2.14^{0.15}_{0.15}$E13	$8.03^{0.57}_{0.57}$E12	$0.295^{0.004}_{0.004}$	$0.155^{0.000}_{0.000}$	$8.26^{0.32}_{0.32}$E43	$7.45^{0.10}_{0.10}$E43	$3.02^{0.30}_{0.30}$E43	$1.96^{0.08}_{0.08}$E12	×	9
Ophiuchus	0.0280	$9.80^{0.61}_{0.61}$	$1.04^{0.05}_{0.05}$E14	$4.26^{0.21}_{0.21}$E13	$0.610^{0.011}_{0.011}$	$0.339^{0.001}_{0.001}$	...	$3.40^{0.04}_{0.04}$E44	...	...	×	10
Tria Aust	0.0510	$9.50^{0.42}_{0.42}$	$1.26^{0.03}_{0.03}$E14	$4.53^{0.12}_{0.12}$E13	$0.730^{0.011}_{0.011}$	$0.370^{0.001}_{0.001}$	$3.97^{0.08}_{0.08}$E44	$3.19^{0.03}_{0.03}$E44	$2.36^{0.07}_{0.07}$E44	$1.20^{0.01}_{0.01}$E13		9

(1) Arnaud & Evrard 1999, (2) David et al. 1993, (3) Day et al. 1991, (4) Fukazawa et al. 1998, (5) Henriksen & Markevitch 1996, (6) Hughes et al. 1993

(7) Johnstone et al. 1992, (8) Markevitch & Vikhlinin 1997, (9) Markevitch et al. 1998, (10) Matsuzawa et al. 1996, (11) Reiprich & Böhringer 2002

(12) Tamura et al. 1996, (13) White 2000

3.2.1 X-ray Luminosity–Temperature Relation

We begin by examining the scaling relation constructed from $L_{X,500}$ (i.e., the X-ray luminosity projected within a distance corresponding to the virial radius r_{500}) and the emission-weighted mean temperature T_X (all temperature values given in this chapter are emission-weighted X-ray temperatures). The luminosity is measured in the 0.5–2 keV band. The virial radius r_Δ is the radius within which the mean density is Δ times the critical density of the universe; these radii are obtained from observed M_{vir}–T_X virial scaling relations. For r_{500} we use a mass–temperature relation obtained using clusters with masses greater than $3.6 \times 10^{13} M_\odot$ (Finoguenov et al. 2001), which gives

$$r_{500} = 0.447\ h_{70}^{-1}\ T_X^{0.527}\ \mathrm{Mpc}\ . \tag{3.1}$$

Note that in our analysis we use the emission-weighted mean temperature rather than cool core-corrected emission-weighted mean temperatures. The Finoguenov et al. (2001) relation is derived using temperature profiles measured with ASCA, but their emission-weighted mean temperatures have been corrected for cool core effects.

One CC cluster in our sample, A3526, has a value of r_{500} large enough that it extends beyond the edges of the PSPC image. Three other CC clusters (Ophiuchus, A426, and A1060) have values of r_{500} that become too large for the images when the temperature is scaled to account for cool core effects in the analysis presented in §3.3. We therefore exclude these four CC clusters from our analysis involving $L_{X,500}$ (and, below, from the analysis of the core-subtracted luminosity within r_{500}).

We consider X-ray luminosity uncertainties from three sources. First, we measure luminosity projected within a virial radius determined by the temperature, so there is an uncertainty in the radius due to the uncertainty ΔT_X in the measured cluster temperature T_X. We thus measure the luminosity projected within radii determined from temperatures $T_X + \Delta T_X$ and $T_X - \Delta T_X$, and average the absolute difference between these luminosities and the luminosity measured at the virial radius. There is also some uncertainty in the X-ray images; we use error images created as described in MME, and sum the error within the region of interest just as we do for the X-ray image counts. Finally, there is an uncertainty in the background, which we account for by raising and lowering the background level by 10%, measuring the luminosity at each level, and averaging the deviations from the value measured with the standard background level. The temperature-induced uncertainty, X-ray image uncertainty, and background uncertainty are added in quadrature to obtain the total uncertainty in the X-ray luminosity.

When we examine the deviation of a cluster from a scaling relation, we do so in one dimension only,

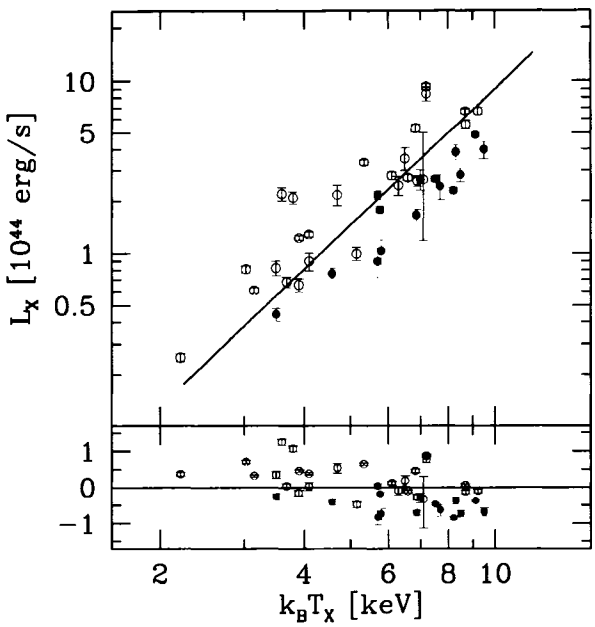

Figure 3.1 — X-ray luminosity projected within r_{500} (*top*), and deviation of clusters from the best fit relation (*bottom*). Open and filled markers correspond to CC and NCC clusters, respectively. The uncertainties include both the measurement uncertainty in the luminosity and an effective temperature contribution to the luminosity uncertainty as described in the text.

e.g., only for luminosity in the luminosity–temperature relation. We thus include a temperature component to the uncertainty in each observable, which we approximate using the best fit power law to the observed scaling relation. That is, for each observable $\mathcal{O}$ we determine the scaling relation exponent α (i.e., $\mathcal{O} \propto T_{\rm X}^{\alpha}$), and find a fractional uncertainty due to the temperature,

$$\frac{\sigma_{\mathcal{O}}}{\mathcal{O}} = \alpha \frac{\sigma_{T_{\rm X}}}{T_{\rm X}} \ , \tag{3.2}$$

which is added in quadrature to the measurement uncertainty.

Figure 3.1 shows the $L_{\rm X,500}$–$T_{\rm X}$ scaling relation, including uncertainties. One immediately notices that there is a separation of the CC and NCC populations on the relation, i.e., the CC clusters tend to lie above the best-fit line, and the NCC clusters lie below; this relationship has been observed before (e.g., Fabian et al. 1994; Markevitch 1998; McCarthy et al. 2004). One part of the separation is likely a simple temperature bias; that is, CC clusters have a cool central region that does not significantly affect the structure of the cluster outside that region, but whose relatively high density leads to a significant bias toward lower emission-weighted mean temperatures relative to clusters without a cool core. The remainder of the separation is due primarily to the higher central gas density in CC clusters, which leads to greater X-ray luminosity at a

Table 3.2. Raw and Intrinsic Scatter in Scaling Relations

	Observations						Simulations[a]
	Original Relations		With CC Temp. Scaling		3 Parameter ($\mathcal{O}$–T_X–I_0)		
Scaling Relation	σ_{raw}	σ_{int}	σ_{raw}	σ_{int}	σ_{raw}	σ_{int}	σ_{int}
$M_{ICM,500}$–T_X	0.19	0.17	0.18	0.17	0.16	0.15	0.20
$M_{ICM,2500}$–T_X	0.23	0.22	0.20	0.19	0.16	0.14	
$L_{X,500}$–T_X	0.53	0.53	0.34	0.33	0.26	0.24	
$L_{X,2500}$–T_X	0.69	0.67	0.39	0.39	0.36	0.34	
$L_{XCS,500}$–T_X	0.29	0.28	0.25	0.23	0.23	0.21	0.27
$R_{3\times10^{-14}}$–T_X	0.14	0.14	0.14	0.14	0.13	0.13	0.10
$R_{1.5\times10^{-13}}$–T_X	0.17	0.17	0.17	0.17	0.14	0.14	
$L_{NIR,500}$–T_X	0.19	0.19	0.17	0.17	0.19	0.19	
$R_{3\times10^{-14}}$–$M_{ICM,500}$	0.06	0.06					
$R_{3\times10^{-14}}$–$L_{XCS,500}$	0.06	0.05					
$R_{3\times10^{-14}}$–$L_{NIR,500}$	0.16	0.16					

[a]For simulations, $M_{ICM,500}$ is actual gas mass, not measured from mock observations, and the isophote for R_I is chosen to produce normalization similar to the observed $R_{3\times10^{-14}}$–T_X relation.

given temperature.

Because we will be examining the scatter about scaling relations and drawing conclusions about the effects of substructure on those relations, it is important to establish that the scatter is a real, intrinsic effect, and not due to measurement uncertainties. This is made plain qualitatively from the bottom portion of Figure 3.1, which shows the deviation from the best-fit relation; the uncertainties in L_X are clearly smaller than the intrinsic scatter in the relation. To address the issue quantitatively, we measure both the raw (i.e., RMS) scatter and the intrinsic scatter, which we express in terms of $\ln \mathcal{O}$, by finding the values of σ for which the reduced χ^2 value for a given relation is unity. We find the intrinsic scatter σ_{int} by adding a uniform value in quadrature to the measurement uncertainty for each cluster.

For the $L_{X,500}$–T_X relation, we find σ_{int}=σ_{raw}= 0.53 (these values are also listed in Table 3.2); that is, the intrinsic and raw scatter are the same to the precision given here, and so the intrinsic scatter is clearly much greater than the measurement uncertainties. We may thus be certain that the scatter about this relation is due to real structural differences between the clusters.

3.2.2 Other X-ray Scaling Relations

In addition to the luminosity projected within r_{500}, we measure $L_{X,2500}$, the luminosity projected within r_{2500}; studying relations at different radii gives us information about the effects of structural variations on

different scales within the cluster. To determine r_{2500} we use an M_{2500}-$T_{\rm X}$ relation derived from *Chandra* observations of relaxed intermediate-redshift clusters (Allen et al. 2001), which gives

$$r_{2500} = 0.227\ h_{70}^{-1}\ T_X^{0.503}\ \mathrm{Mpc}\ . \tag{3.3}$$

We also measure the core-subtracted X-ray luminosity ($L_{\rm XCS}$) within r_{500}. We exclude the luminosity projected within a radius corresponding to $0.20r_{500}$, which minimizes the effects of core structure (e.g., Neumann & Arnaud 1999). This radius corresponds to $0.13r_{200}$, where the virial radius r_{200} is calculated from r_{500} by using an NFW dark matter density profile with concentration parameter $c = 5$ (Navarro et al. 1997); the relationship is $r_{200} = 1.51r_{500}$.

We measure the ICM mass within r_{500} and r_{2500}. The masses are measured as discussed in MME, using the β-model parameters given in that paper (some clusters are fit with a double β-model), the emission-weighted mean temperature, and a measurement of the X-ray flux. We use the $M_{\rm ICM,500}$ uncertainties from MME as a starting point, but we adjust the temperature uncertainty contribution to reflect the newer and more accurate temperatures available for some clusters. We adopt the same fractional uncertainty for $M_{\rm ICM,2500}$ as for $M_{\rm ICM,500}$; the median fractional uncertainty is $\sim$3%.

We determine the isophotal size R_I of a cluster by measuring the area A_I enclosed by a particular isophote I and finding the effective radius given by $A_I = \pi R_I^2$. We measure R_I for two isophotes: 3×10^{-14} erg s^{-1} cm^{-2} arcmin^{-2} and 1.5×10^{-13} erg s^{-1} cm^{-2} arcmin^{-2}, in the 0.5–2 keV band. The lower isophote lies well outside the core region of the clusters, and so, like the luminosities and masses measured within r_{500}, reflects cluster structure in a way largely unaffected by core substructure. The higher isophote is more reflective of core structure. For some clusters in our sample the central surface brightness does not rise (or barely rises) above the brighter isophote; these eight clusters are excluded from all analysis at this isophote.

When measuring the isophotal size we include a background uncertainty of 10%, calculate R_I with the higher and lower uncertainty, and take the average of the deviations from the standard background value to obtain the uncertainty in R_I. PSPC also has a $\sim$10% uncertainty in its effective area. However, changing the effective area tends to simply shift the entire cluster population up or down in isophotal size, and does not affect the deviation of individual clusters from the relations; hence, we ignore this particular uncertainty. In the soft X-ray band the conversion from PSPC counts s^{-1} to physical flux is approximately independent of cluster temperature, and so temperature uncertainties do not lead to uncertainties in the measured isophotal size.

Each observable derives from a different integral over cluster structure:

$$\langle T_{\rm X} \rangle = \frac{1}{L_{\rm X}} \int n_e^2 \frac{\mu_e}{\mu_{\rm H}} \Lambda(T) T d^3x \tag{3.4}$$

$$L_{\rm X} = \int n_e^2 \frac{\mu_e}{\mu_{\rm H}} \Lambda(T) d^3x \tag{3.5}$$

$$M_{\rm ICM} = \int \mu_e m_p n_e d^3x \ , \tag{3.6}$$

where $\Lambda(T)$ is the emissivity of the ICM gas, and the other symbols have their usual meanings. Isophotal size derives from cluster structure in a somewhat more complex way; see Mohr et al. (2000) for a discussion. Thus by studying multiple observables, we are not simply increasing the size of our parameter space; we are, in fact, looking at several different ways of quantifying the structure of clusters. By focusing on crude observables like these we are able to work in a regime where the measurement uncertainties are small compared to the intrinsic scatter.

The scaling relations for $M_{\rm ICM,500}$, $R_{3\times10^{-14}}$, and $L_{\rm XCS,500}$ are shown in Figure 3.2; in Figure 3.3 we plot relations for $M_{\rm ICM,2500}$, $L_{\rm X,2500}$, and $R_{1.5\times10^{-13}}$. For clarity we do not show measurement uncertainties; however, as shown for $L_{\rm X,500}$ in Figure 3.1 they are significantly smaller than the intrinsic scatter. The actual measurements of raw and intrinsic scatter are given for all relations in Table 3.2; the intrinsic scatter dominates the total scatter in all cases.

All X-ray relations indicate a separation between CC and NCC clusters. The non-core-subtracted luminosities show the largest effect; this is not surprising, because the luminosity is the observable most affected by the buildup of dense gas in cool cluster cores. The relations that are more sensitive to the ICM distribution on larger scales show less of an offset between CC and NCC clusters. In addition, these larger scale measurements (e.g., $M_{\rm ICM,500}$) show less scatter than relations at smaller scales (e.g., $M_{\rm ICM,2500}$). This is an interesting finding; it shows simply that core structural variations and temperature biases have a larger effect on relations measured in smaller regions around the core. This is an indication of the importance of core structure, which we discuss further below.

3.2.3 K-band Light–Temperature Relation

The X-ray observables provide information about the ICM. We now turn to a very different cluster property, the K-band galaxy light. The near-infrared (NIR) light traces stellar mass better than optical bands, and

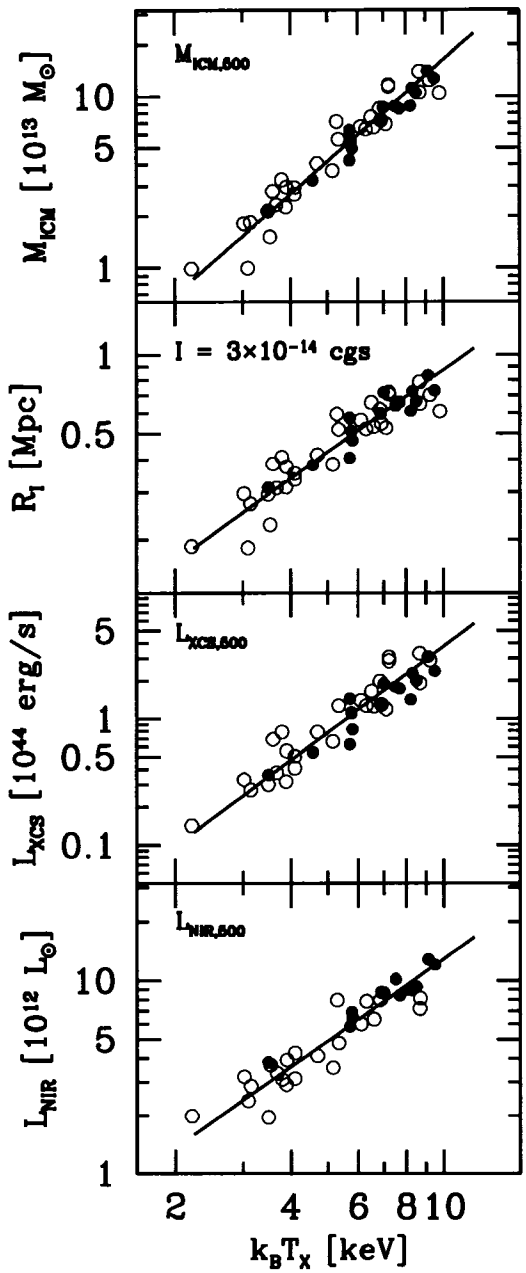

Figure 3.2 — From top to bottom, we show scaling relations for $M_{\rm ICM}$ within r_{500}, isophotal size for an isophote of 3×10^{-14} erg s^{-1} cm^{-2} arcmin^{-2}, the X–ray core subtracted luminosity projected within r_{500}, and the K-band luminosity projected within r_{500}, versus $T_{\rm X}$. The open and filled markers correspond to CC and NCC clusters, respectively.

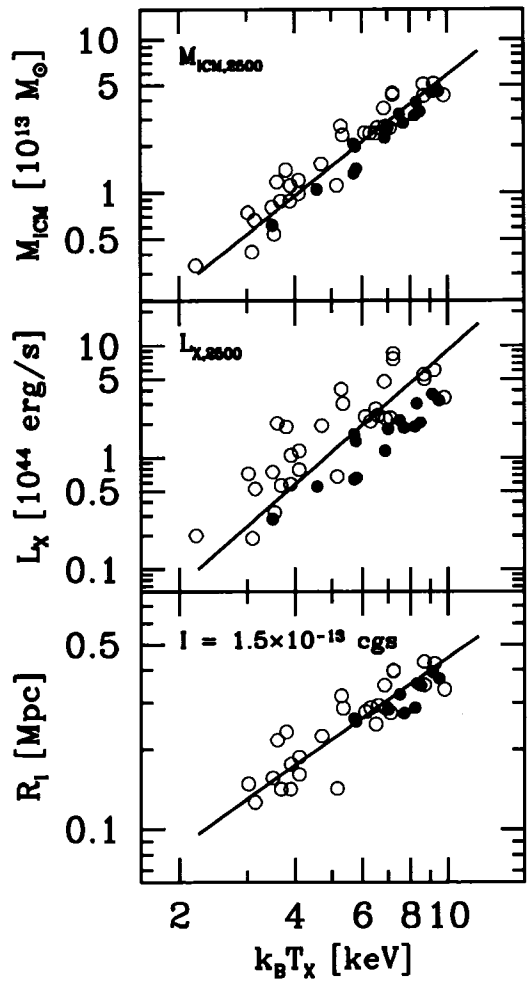

Figure 3.3 — Scaling relations for $M_{\rm ICM}$ within r_{2500}, X-ray luminosity projected within r_{2500}, and isophotal size for an isophote of 1.5×10^{-13} erg s^{-1} cm^{-2} arcmin^{-2}, versus $T_{\rm X}$. The open and filled markers correspond to CC and NCC clusters, respectively.

is well correlated with such properties as cluster binding mass (e.g., Lin et al. 2003, 2004). By comparing information from the X-ray and NIR observables, we hope to gain a better understanding of, for example, the true temperature bias introduced by cool cores. The K-band data we use is taken from Lin et al. (2004); these data are available for 34 of the clusters in our sample. The measurements of near-IR light are effectively a simple sum of the light from individual galaxies, and thus represent a very different measure of galaxy cluster properties than the X-ray observables discussed above.

At the bottom of Figure 3.2 we plot the K-band luminosity within r_{500}. Here visual inspection suggests less evidence for a separation between the CC and NCC populations than in the X-ray relations. As with the X-ray observables, the scatter in the relation is dominated by the intrinsic scatter, as shown by the values

for $\sigma_{\rm int}$ and $\sigma_{\rm raw}$ given in Table 3.2.

3.3 Cool Core and Non-Cool Core Populations

It is clear that the presence of cool cores affects all of the ICM-related scaling relations. As previously discussed, this is likely a result of various physical differences between CC and NCC clusters, which include a simple temperature bias effect. Because we want to examine merger-related scatter about the scaling relations, we must account for this separation of populations in a way that will allow us to compare CC and NCC clusters in a manner independent of cooling effects. One approach would be to treat these two populations individually, examining deviations from scaling relations in each. In this section we effectively take this approach by applying a correction to the CC population so that in the mean these clusters lie on the same scaling relation as the NCC population. Below we describe this approach as well as the amplitude of the offsets between the CC and NCC populations in each of the scaling relations. An alternative, more sophisticated approach will be presented in §3.4.

3.3.1 Aligning CC and NCC Populations

To begin with, we align the CC and NCC population scaling relations by scaling the mean temperature of all CC clusters by the same amount within a given relation. To find the appropriate scale factor for a relation, we increase $T_{\rm X}$ for the CC clusters by a range of factors (using the same factor for all CC clusters), re-measure the relevant observable at each temperature, and measure the reduced χ^2 for the entire sample at each scale factor. Because the measurement uncertainties are so small, we use a combination of measurement and intrinsic scatter, which reduces the dependence of the scale factor on outlier clusters. We measure χ^2 versus temperature scale factor, then find a value for the intrinsic scatter $\sigma_{\rm int}$ that makes the reduced $\chi^2 = 1$ at the χ^2 minimum. We then find the temperature scale factor that corresponds to the new χ^2 minimum, and so on, until the process converges. That is, for an observable $\mathcal{O}$, we find temperature scale factor λ and intrinsic scatter $\sigma_{\rm int}$ such that

$$\frac{\chi^2}{N_{\rm dof}} = \sum_i \frac{[\mathcal{O}_i(\lambda T_i) - \mathcal{O}_{\rm fit}(\lambda T_i)]^2}{\sigma_i^2 + \sigma_{\rm int}^2} = 1 \tag{3.7}$$

at the χ^2 minimum for $N_{\rm dof}$ degrees of freedom.

Because aligning the CC and NCC cluster populations decreases the total scatter in each scaling relation, we must verify that the intrinsic scatter in the relations remains significantly greater than the measurement uncertainty. We again examine $L_{\rm X,500}$, after scaling the CC cluster temperatures by a factor of 1.38,

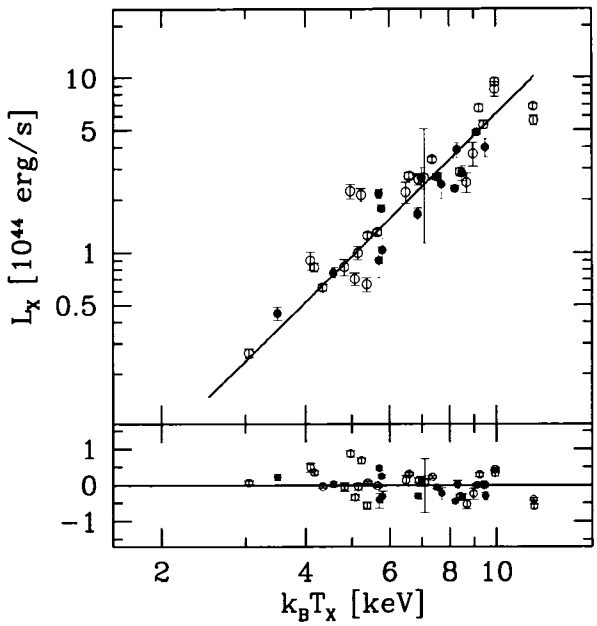

Figure 3.4 — X-ray luminosity projected within r_{500} (*top*), and deviation of clusters from the best fit relation (*bottom*), after scaling the CC cluster temperatures to align the CC and NCC cluster populations. Open and filled markers correspond to CC and NCC clusters, respectively. The uncertainties include both the measurement uncertainty in the luminosity and an effective temperature contribution to the luminosity uncertainty as described in the text.

determined by the method described. The resulting scaling relation is shown in Figure 3.4 (cf. the relation with non-scaled temperatures in Figure 3.1). Although the total scatter in the relation is now significantly less than in the original relation, it still is clearly larger than the luminosity measurement uncertainties. We quantify this as before, measuring the raw and intrinsic scatter, and find that $\sigma_{\rm int}$= 0.33 and $\sigma_{\rm raw}$= 0.34, again showing the dominance of the intrinsic scatter over measurement uncertainties (scatter measurements for CC temperature-scaled relations are given in Table 3.2).

A plot of χ^2 versus temperature scale factor for all of the X-ray and NIR scaling relations is shown in Figure 3.5; the derived scale factors, plus their uncertainties, are listed in order from highest to lowest scale factor in Table 3.3. Clearly, a greater scale factor is required to align the CC and NCC populations for parameters that measure a smaller, more core-dominated region of the cluster, as discussed in §3.2.2. Similar scale factors of ∼5% and ∼1%, respectively, will align the two populations for both $M_{\rm ICM}$ within r_{500} and $R_{3\times10^{-14}}$. There is a somewhat larger difference between temperature scale factors for $M_{\rm ICM}$ within r_{2500}, $R_{1.5\times10^{-13}}$, and the core-subtracted luminosity within r_{500} (∼19%, ∼10%, and ∼15%). A much greater scale factor is needed in either case for $L_{\rm X}$ (∼38% within r_{500}, ∼ 47% within r_{2500}). This demonstrates that the luminosity is affected by more than just the shift in temperature due to the presence of emission from a cool

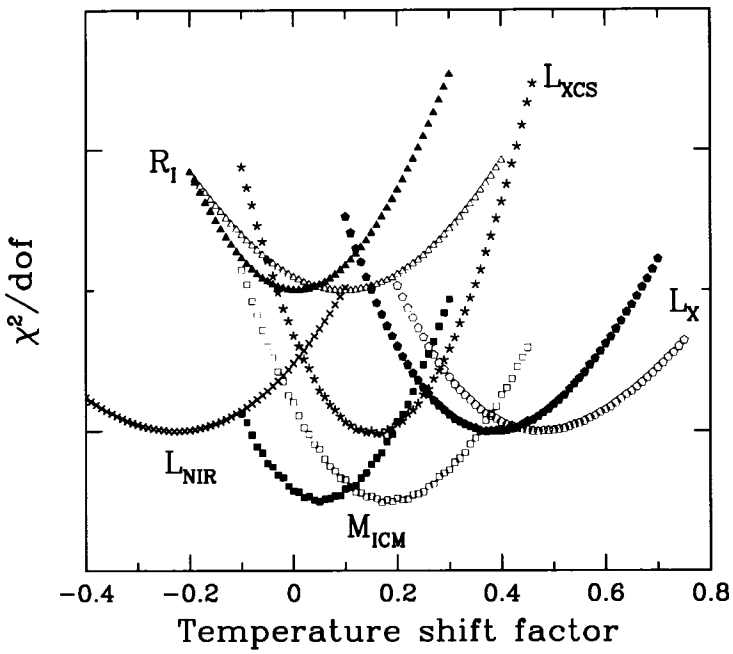

Figure 3.5 — Reduced χ^2 versus CC temperature scale factor for each of the eight observable–temperature scaling relations. Pentagons: Projected luminosity within r_{500} (filled) and r_{2500} (open). Squares: ICM mass within r_{500} (filled) and r_{2500} (open). Triangles: Isophotal size for isophotes of 3×10^{-14} erg s^{-1} cm^{-2} arcmin^{-2} and 1.5×10^{-13} erg s^{-1} cm^{-2} arcmin^{-2} (open). Stars: Projected core-subtracted luminosity within r_{500}. Crosses: Projected NIR light within r_{500}. Vertical axis units are reduced χ^2 value, but relations are offset vertically from one another for ease of viewing so vertical axis labels are not shown.

core.

3.3.2 Examining the CC Temperature Bias

Besides the cool core temperature bias, these scaling relations may be affected by cool core-related structural phenomena and merger-related phenomena that are in some way related to the presence or absence of cool cores. A cool, dense core results in a sharp central brightness peak that drives up the total luminosity of the cluster, adding to the separation between CC and NCC clusters on the L_X–T_X scaling relation. The increased central surface brightness also makes isophotal sizes larger and leads to higher measured gas masses in the central regions. However, idealized studies of mergers of spherical, isolated clusters suggest that both ICM temperature and X-ray luminosity may be boosted during mergers, and that clusters can be perturbed from scaling relation by the merger (Ricker & Sarazin 2001). If present, this behavior would also tend to separate the merging and non-merging (and hence NCC and CC) populations.

A good way of differentiating between these two effects is to examine a relation that has minimal temperature dependence. To examine the impact of cool core effects on scaling relations at large radii, we plot

Table 3.3. Cool Core Temperature Scale Factors

Scaling relation	T_X scale factor
$L_{X,2500}$–T_X	1.47 ± 0.07
$L_{X,500}$–T_X	1.38 ± 0.06
$M_{ICM,2500}$–T_X	1.19 ± 0.05
$L_{XCS,500}$–T_X	1.15 ± 0.04
$R_{1.5\times10^{-13}}$–T_X	1.10 ± 0.07
$M_{ICM,500}$–T_X	1.05 ± 0.04
$R_{3\times10^{-14}}$–T_X	1.01 ± 0.05
$L_{NIR,500}$–T_X	0.77 ± 0.08

$R_{3\times10^{-14}}$ versus $M_{ICM,500}$ as shown in Figure 3.6. Isophotal size is independent of temperature, and at a low isophote core effects should be of little importance. The ICM mass within a large radius will have only a slight dependence on core features, because only a small fraction of the cluster ICM mass lies within the core region. Though r_{500} depends on temperature, any bias effect this introduces is weak. Hence, a scaling relation composed of these two observables provides a test of how much the cool core bias affects the structure outside the cluster core. Indeed, the relation shows no particular suggestion of separation between the CC and NCC populations, and the total scatter in the relation is much smaller than for any of the previously discussed observable–temperature relations. This provides evidence that the primary contributor to the CC/NCC separation in the observables at large radii is indeed a simple temperature bias, and not structural changes related to the development or disruption of cool cores. This also gives us confidence that the offset between the CC and NCC populations is caused by the onset of a cooling instability within the cluster core rather than by shock-induced temperature and structural changes during mergers, which we would expect to be most apparent in observables that are sensitive to cluster structure outside the core (where relaxation timescales are the longest).

Adopting this perspective, we can take the scale factors for relations involving observables that are less core sensitive to estimate the scale of the temperature bias. For example, the $M_{ICM,500}$ and $R_{3\times10^{-14}}$ relations have scale factors of 1.04 ± 0.04 and 1.01 ± 0.05, respectively, suggesting that temperature biases are at the few percent level, and that it is indeed structural differences in the core that are driving the larger scale factors seen in the more core sensitive observables. Interestingly, the near-IR relation shows less evidence for a cool core-related separation. In fact, following the same procedure as for the X-ray relations indicates that a *negative* scale factor of $\sim$23% is required to align the CC and NCC populations. (This may be partly driven by a few outliers, but having no reason to discard these data points, we do not exclude them.) This suggests that the galaxy population in CC clusters contains systematically less light than the

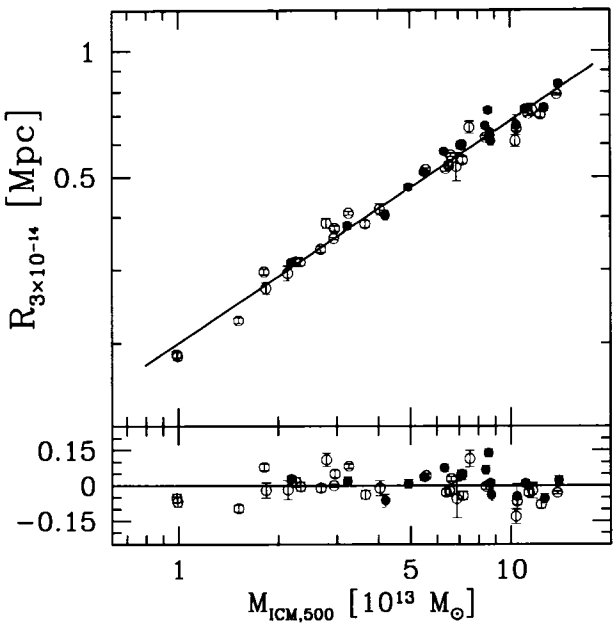

Figure 3.6 — $R_{3\times10^{-14}}$ plotted versus $M_{\rm ICM,500}$, along with the best-fit relation (*top*), and deviation in R_I from the best-fit relation (*bottom*). Open and filled markers correspond to CC and NCC clusters, respectively. Uncertainties are a combination of R_I measurement uncertainties and an effective uncertainty in R_I due to the mass uncertainty obtained using the scaling relation slope, as was done with temperature uncertainties for other relations.

galaxy population in NCC clusters, a result that deserves further attention.

3.3.3 Intrinsic Scatter in CC and NCC Populations

Having removed to first order, via temperature scaling of CC clusters, the separation between cluster populations, we can begin to study the effects of merging on scatter about scaling relations; because mergers are expected to disrupt cool cores, and because merging clusters are naively expected to have greater scatter about scaling relations, one would expect to observe greater scatter in NCC clusters. We therefore measure the intrinsic scatter in the temperature-scaled CC population and the NCC population separately as a test of overall structural differences between them. That is, we measure the scatter of each (CC and NCC) population about the *same* best-fit scaling relation. These values are given for all eight $\mathcal{O}$–$T_{\rm X}$ scaling relations in Table 3.4. We use an F-test to quantify the significance of differences between CC and NCC scatter for a given relation; the table lists the percent significance level at which equality of the variances is rejected. Remarkably, we do not observe greater scatter in the NCC population; indeed, the CC population has significantly (i.e., $> 68\%$ significance) greater scatter than the NCC population in all but one scaling relation.

Table 3.4. Intrinsic Scatter in CC and NCC Subsamples

Scaling Relation	With CC Temperature Scaling			3 Paramter ($\mathcal{O}$–T_X–I_0)		
	CC σ_{int}	NCC σ_{int}	Diff. (%)[a]	CC σ_{int}	NCC σ_{int}	Diff. (%)[a]
$M_{ICM,500}$–T_X	0.20	0.09	99.6+	0.17	0.11	93.0+
$M_{ICM,2500}$–T_X	0.22	0.10	99.6+	0.17	0.08	99.7+
$L_{X,500}$–T_X	0.37	0.28	73.0+	0.28	0.18	90.7+
$L_{X,2500}$–T_X	0.44	0.31	83.6+	0.40	0.20	99.3+
$L_{XCS,500}$–T_X	0.24	0.24	5.3+	0.22	0.22	3.6-
$R_{3\times10^{-14}}$–T_X	0.15	0.10	91.9+	0.14	0.11	62.3+
$R_{1.5\times10^{-13}}$–T_X	0.19	0.10	95.1+	0.16	0.10	84.0+
$L_{NIR,500}$–T_X	0.21	0.09	99.3+	0.23	0.12	97.3+

[a]Percent likelihood that scatter measurements for CC and NCC subsamples are different; see text. Plus sign indicates that CC scatter value is higher than NCC scatter value.

The uniform CC temperature scaling method treats all CC clusters in exactly the same way. The greater scatter in the CC population, however, provides evidence of significant structural variation within that population—more variation, in fact, than in the NCC population. We are thus motivated to find a method to reduce CC/NCC separation that takes into account the variability of individual cluster structure. In the next section we present such a method.

3.4 Peak Surface Brightness as a Measure of Cool Core Strength

In this section we discuss another method of reducing cooling-related scatter in scaling relations: the use of peak surface brightness as an indication of cool core "strength". We include surface brightness as a third parameter in scaling relations, show that this parameter's contribution to the relation is significant in all X-ray observable–temperature relations, and demonstrate its usefulness in reducing cool core-related scatter.

3.4.1 Brightness Measurements

We use measurements of the peak surface brightness I_0 from MME. These values were obtained by fitting β models to azimuthally-averaged cluster surface brightness profiles. Clusters that appeared relaxed and displayed residuals consistent with a central emission excess were fit with a double β model, i.e., two models with the same β but different I_0 and core radius were summed and fitted together; the cluster I_0 is then the sum of the individual I_0 from each model. In Figure 3.7 we plot the central cooling time versus I_0 for the 45 clusters in our sample. There is a clear correlation between the two quantities, which is not surprising as

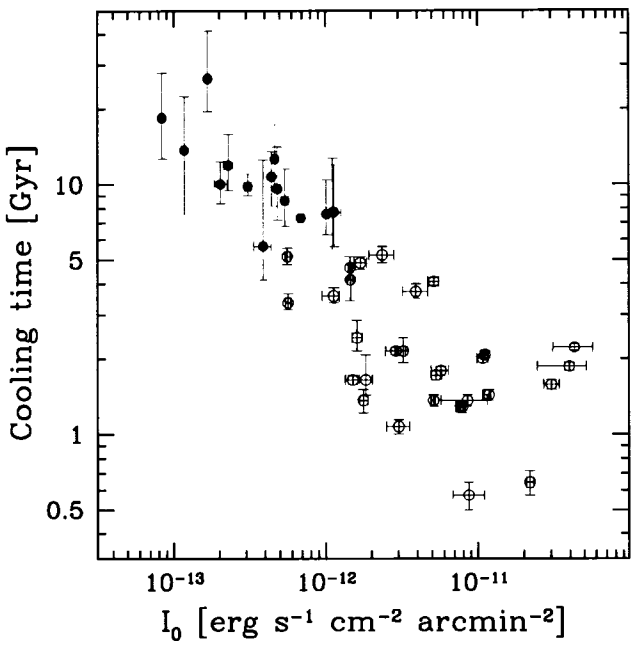

Figure 3.7 — Central cooling time from Peres et al. (1998) plotted versus peak surface brightness I_0. Open and filled markers correspond to CC and NCC clusters, respectively.

the central cooling time is derived from the central surface brightness profile. Note that the PSF corrected central surface brightness varies by a factor of ~500 for our flux limited cluster sample, suggesting that even in the low signal to noise regime it should be possible to differentiate the low and high surface brightness systems.

3.4.2 Observable–Temperature–Brightness Relations

We now test whether I_0 is a significant parameter by including it in the observable–temperature scaling relations. That is, for each observable $\mathcal{O}$ we assume a functional form $\mathcal{O} \propto T_X^\alpha I_0^\beta$ and solve for α, β, and the normalization. We first examine the X-ray luminosity projected within r_{500}. A plot of $L_{X,500}$ versus T_X is shown in Figure 3.8. In this figure we have divided the cluster sample into three subsamples based on I_0, and we plot the measured L_X–T_X–I_0 relation for a value of I_0 in the middle of each subsample; we also show the deviation in luminosity for each subsample. This plot shows qualitatively that the scatter about the L_X–T_X–I_0 is much smaller than about the L_X–T_X relation (c.f. the L_X–T_X relation in Fig. 3.1). Quantitatively, we find that the $L_{X,500}$–T_X–I_0 relation has a best-fit power-law dependence on I_0 with an exponent of 0.26 ± 0.03 (uncertainty is obtained from bootstrap resampling and refitting); the I_0 dependence is thus indeed significant. The raw and intrinsic scatter in $L_{X,500}$ about the relation are 0.26 and 0.24,

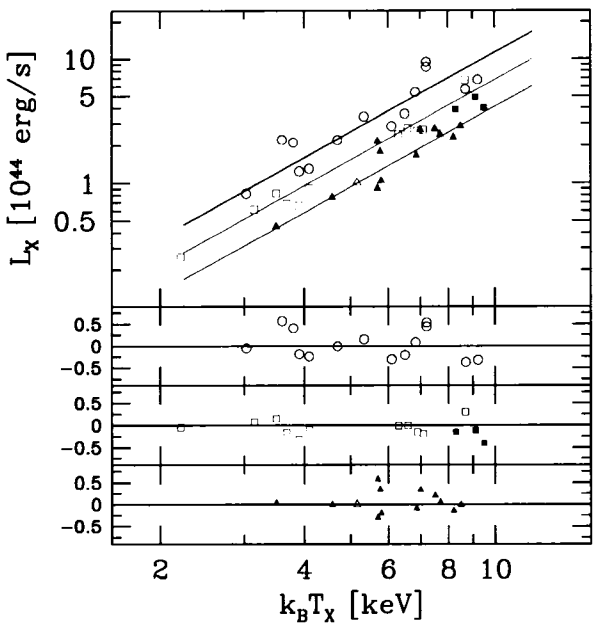

Figure 3.8 — X-ray luminosity projected within r_{500} plotted versus temperature (*top*), and deviation of clusters from the best fit L_X–T_X–I_0 relation calculated for three values of I_0 (*bottom*). For this plot the cluster sample was divided into three subsamples based on I_0; the circles, squares, and triangles are the clusters in the subsamples with the highest, middle, and lowest values of I_0, respectively. Open and filled markers correspond to CC and NCC clusters, respectively.

respectively, much lower than the corresponding values for the original L_X-T_X relation and also lower than for the L_X-T_X relation with CC temperature shifting (see Table 3.2). This dramatic reduction in scatter in the luminosity-related scaling relations suggests that it should be possible to use luminosity together with central surface brightness as a much more accurate cluster mass estimator than luminosity alone.

$\mathcal{O}$–T_X–I_0 scaling relation exponents for the rest of the relations are given in Table 3.5. All X-ray observables have a dependence on I_0 that is significant at greater than two standard deviations; L_{NIR} does not show any I_0 dependence. We conclude that the peak surface brightness does provide us with useful information about cluster structure. Its usefulness for our present purpose is clear given the extent to which scatter about scaling relations is reduced by its introduction. Table 3.2 gives measured raw and intrinsic scatter values for each of the eight observable–T_X–I_0 relations, and separate measurements of CC and NCC scatter are given in Table 3.4. For X-ray observables we find reduced scatter in the $\mathcal{O}$–T_X–I_0 relations compared to the original $\mathcal{O}$–T_X relations, and generally less than for the temperature-scaled relations. The exception is L_{NIR} which, having no dependence on I_0, does not show reduced scatter compared to the original L_{NIR}–T_X relation.

There have been several recent studies of the evolution of cluster scaling relations at intermediate and

Table 3.5. Best Fit Temperature and Brightness Scaling Parameters

Observable	T_X dependence	I_0 dependence	I_0 dependence (T_X bias removed)[a]
$M_{ICM,500}$	1.94 ± 0.09	0.06 ± 0.02	0.00 ± 0.03
$M_{ICM,2500}$	1.92 ± 0.08	0.10 ± 0.02	0.04 ± 0.03
$L_{X,500}$	2.13 ± 0.10	0.26 ± 0.03	0.20 ± 0.04
$L_{X,2500}$	2.33 ± 0.18	0.31 ± 0.03	0.24 ± 0.04
$L_{XCS,500}$	2.21 ± 0.10	0.10 ± 0.03	0.03 ± 0.04
$R_{3\times10^{-14}}$	1.03 ± 0.07	0.03 ± 0.01	0.00 ± 0.01
$R_{1.5\times10^{-13}}$	1.02 ± 0.08	0.07 ± 0.02	0.04 ± 0.02
$L_{NIR,500}$	1.41 ± 0.14	0.00 ± 0.03	-0.04 ± 0.03

[a]That is, the factor γ as defined in Eq. 3.8.

high redshift. Some studies have found positive evolution of cluster X-ray luminosity, consistent with that expected from self-similarity arguments (e.g., Vikhlinin et al. 2002; Maughan et al. 2006), but other observations are consistent with zero or somewhat negative evolution of L_X–T_X and M_{ICM}–T_X scaling relation normalizations (e.g., Borgani et al. 2001; Holden et al. 2002; Ettori et al. 2004b). Given the difference in normalizations for the CC and NCC populations, this may be partially explained by a simple change in the cool core fraction in the samples being compared, which will shift the normalization of the entire cluster population. It would thus potentially be useful to compare $\mathcal{O}$–T_X–I_0 relations at low and high redshift, as the inclusion of a parameter measuring cool core strength may reduce this evolution effect.

3.4.3 Temperature and Other Observable Biases

We can use this three parameter scaling relation approach to again estimate the scale of the temperature biases. Scaling relations involving properties that have low dependence on core structure should have little to no dependence on I_0. That all X-ray observable–temperature relations show a significant I_0 dependence can be taken as evidence for temperature biases in CC clusters; that is, the cool gas in CC cluster cores biases emission-weighted mean temperatures so that CC clusters appear to lie above scaling relations. We can attempt to quantify this bias in terms of I_0. We assume scaling relations of the form

$$\mathcal{O} = \mathcal{O}_0 T_X^\alpha I_0^\beta = \mathcal{O}_0 \left(\lambda(I_0) T_X\right)^\alpha I_0^\gamma \tag{3.8}$$

for each observable $\mathcal{O}$. If a scaling relation has no intrinsic dependence on I_0 (i.e., $\gamma = 0$), then $\lambda(I_0) \propto I_0^{\beta/\alpha}$. We assume that the $M_{ICM,500}$–T_X and $R_{3\times10^{-14}}$–T_X relations have no intrinsic I_0 dependence (see §3.3.2),

and so $\lambda(I_0) \propto I_0^{(0.03\pm0.01)}$. The temperature bias thus varies by ~20% over the range of I_0 in our sample; using the median values of I_0 for the CC and NCC populations (4.5×10^{-14} and 4.4×10^{-13} erg s^{-1} cm^{-2} arcmin^{-2}, respectively) gives an average CC temperature scale factor of 1.07 ± 0.02 (simply averaging the CC temperatures scale factors for $M_{\rm ICM,500}$ and $R_{3\times10^{-14}}$ from §3.3.1 gives 1.03 ± 0.03).

For the other scaling relations, $\gamma = \beta - (0.03 \pm 0.01)\alpha$. The values for γ, i.e., the dependence on I_0 when the temperature bias is removed, are given in the fourth column of Table 3.5. Not surprisingly, the X-ray luminosities still have by far the strongest I_0 dependence, which differs by a factor of four between the highest and lowest values of I_0 in our sample. The $M_{\rm ICM,2500}$ dependence on I_0 varies by ~30% over the sample. This suggests that the gas fraction varies significantly within r_{2500} depending on the strength of the cool core; variations of this scale will present challenges for those using cluster gas fractions of "relaxed" clusters to precisely study cosmology.

3.5 Substructure as a Source of Scatter

We now examine the relationship between substructure and the position of clusters on scaling relations. Having introduced two ways to remove the cool core temperature bias, we now attempt to examine the merger related structural differences as deviations by clusters from scaling relations. In this section, we review the substructure measurements, and then discuss how deviation from scaling relations depends on substructure. We then compare results from the observational sample to an ensemble of hydrodynamical simulations.

3.5.1 Substructure Measurements

High-resolution instruments such as *Chandra* reveal hydrodynamic phenomena such as cold fronts that are clearly related to merging. However, it is generally not necessary to directly observe such features to find evidence of merger-related activity. Relatively crude, low-order moments of the X-ray surface brightness distribution such as centroid variation and ellipticity have been shown to be effective at separating clusters with recent major mergers from more relaxed systems (Mohr et al. 1993; Evrard et al. 1993), although these measurements are essentially unaffected by mergers along the line of sight. These measurements do not require the high resolution of *Chandra*, and they were used to show that more than half of clusters display substructure in their ICM (Mohr et al. 1995).

The centroid variation w is a measure of the "center shift", or skewness of the photon distribution of a cluster. There are many ways to measure w; here, we measure within an isophote of 2×10^{-14} erg s^{-1}

cm^{-2} $arcmin^{-2}$, chosen as the lowest isophote that can be used for all of our cluster images. We measure the centroid of the portion of the cluster that has surface brightness above this isophote. We then examine the cluster at steadily brighter isophotes and measure the variance in the centroids measured for all these isophotes. The centroid variation w is the square root of this variance. We scale w to be in units of r_{500} for each cluster; using the fractional variation rather than the raw variation simply accounts for the fact that the size of cluster virial radii can vary by as much as a factor of $\sim$4 from low mass to high mass systems. Measuring the centroid variation using regions defined by isophotes rather than using circular annuli as in Mohr et al. (1993) can provide information that circular apertures may not; during mergers, clusters often do not have circular surface brightness distributions, and elongated structure may be missed or underemphasized by fixed circular apertures.

We determine the axial ratio η from the flux-weighted second moments of the photon distribution, using an aperture centered on the brightness peak. That is, we measure moments

$$M_{ij} = \sum I x_i x_j \ , \tag{3.9}$$

where the sum is carried out over all pixels within a chosen aperture, x_i are pixel coordinates (x or y) relative to the center of the aperture, and I is the measured intensity in the pixel. We measure η within an aperture of radius r_{500} for each cluster, except for four clusters for which r_{500} either is larger than our PSPC image or is close enough to the edge that background problems arise. In these cases we use apertures of radius r_{2500}. Using virial radii for the apertures provides a more physically meaningful scale for examining substructure than using a fixed metric radius. Diagonalizing the matrix obtained from equation (3.9) gives the lengths of the major and minor axes, from which we then obtain the axial ratio. While high ellipticity is not a certain indicator of cluster substructure, and is sometimes observed even in apparently relaxed clusters (e.g., Schuecker et al. 2001), hydrodynamical simulations show that during major mergers the ICM is typically highly flattened (Evrard et al. 1993; Pearce et al. 1994).

Another method to quantify cluster substructure makes use of "power ratios" (Buote & Tsai 1995). This involves measuring moments of the surface brightness distribution Σ within some radius $R_{\rm ap}$:

$$a_m(R_{\rm ap}) = \int_{R' \le R_{\rm ap}} \Sigma(\mathbf{x}')(R')^m \cos m\phi' \, d^2x' \ , \tag{3.10}$$

$$b_m(R_{\rm ap}) = \int_{R' \le R_{\rm ap}} \Sigma(\mathbf{x}')(R')^m \sin m\phi' \, d^2x' \ . \tag{3.11}$$

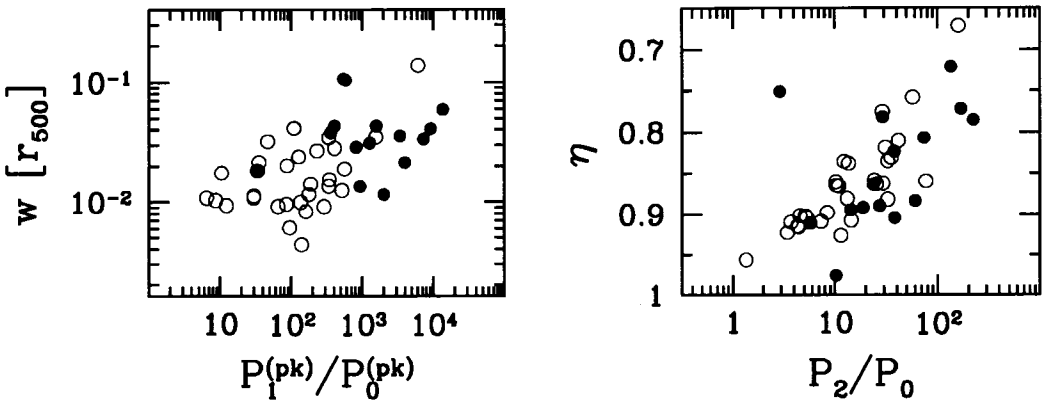

Figure 3.9 — Comparison of centroid variation w to the power ratio $P_1^{(pk)}/P_0^{(pk)}$ (*left*), and of axial ratio η to the power ratio P_2/P_0 (*right*), for the 45 clusters in the PSPC sample. Power ratio values are quoted in units of 10^{-7}; centroid variation is plotted in units of r_{500}. Open and filled markers are CC and NCC clusters, respectively.

The "powers" P_m are then given by:

$$P_0 = [a_0 \ln(R_{\rm ap})]^2 \tag{3.12}$$

for $m = 0$, and

$$P_m = \frac{1}{2m^2 R_{\rm ap}^{2m}}(a_m^2 + b_m^2) \tag{3.13}$$

for $m > 0$, where $R_{\rm ap}$ is the radius of the circular aperture in which the moments are measured. The quantities of interest are the ratios P_m/P_0; the division by P_0 normalizes the flux within the radius of interest, allowing comparison of cluster observations with different fluxes and exposure times. The quantity $P_1^{(pk)}/P_0^{(pk)}$, which is calculated within an aperture centered on the cluster surface brightness peak, is similar to the centroid variation w. Other ratios $P_{m>1}/P_0$ are measured within an aperture centered on the point where the centroid variation is at a minimum; the quantity P_2/P_0 is related to the axial ratio η.

Using a sample of PSPC observations, Buote & Tsai (1996) argue that certain relationships between power ratios may be viewed as evolutionary tracks. We seek here to find correlations between power ratios—mainly the simplest to interpret, $P_1^{(pk)}/P_0^{(pk)}$ and P_2/P_0—and the deviations of clusters from scaling relations. We break from their approach of using fixed metric radii and use an aperture that scales with the cluster mass or temperature; specifically, we study the power ratios within the same characteristic radii (r_{500} or r_{2500}) as we do with axial ratios. This provides a more physically meaningful scale for a cluster sample that spans more than an order of magnitude in mass. Figure 3.9 contains plots of centroid variation versus $P_1^{(pk)}/P_0^{(pk)}$ (*left*) and of axial ratio versus P_2/P_0 (*right*). The centroid variation w and the axial ratio η are correlated with the primary power ratio $P_1^{(pk)}/P_0^{(pk)}$ and P_2/P_0, respectively. Because neither pair of substructure

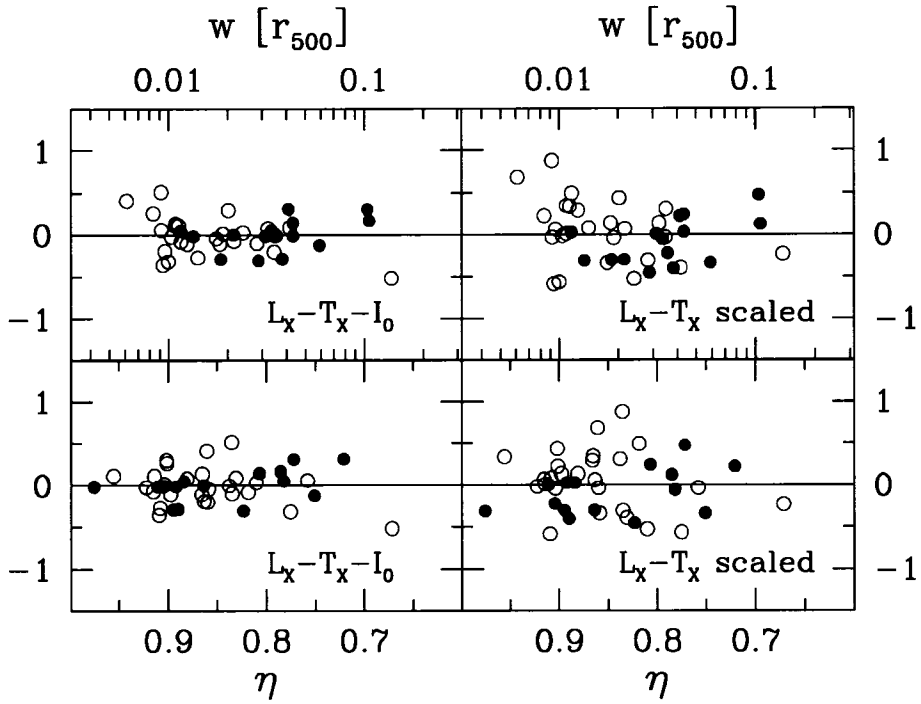

Figure 3.10 — Logarithmic (base-e) deviations of clusters from best-fit $L_{X,500}$–T_X–I_0 scaling relation (*left*) and best-fit $L_{X,500}$–T_X relation (*right*) versus centroid variation w (*top*) and axial ratio η (*bottom*). Open and filled markers are CC and NCC clusters, respectively. Centroid variations are given in units of r_{500}.

measurements is perfectly correlated, we benefit from using all four measurements.

3.5.2 Substructure and Scaling Relations: CC Temperature Scaling vs. $\mathcal{O}$–T_X–I_0 Relations

To test for merger-related scatter in scaling relations, we measure the scatter about scaling relations by subsamples of clusters, split according to the four substructure measures discussed above. We wish to minimize cool core related scatter, and we have discussed two methods of doing so in this chapter: uniform CC cluster temperature scaling, and use of peak surface brightness as a third parameter in observable–temperature scaling relations.

As shown above, the $\mathcal{O}$–T_X–I_0 relations generally have lower scatter than the CC temperature-scaled relations; however, one may wonder whether scatter information is being lost in the $\mathcal{O}$–T_X–I_0 relations. Qualitative comparisons suggests that this is not the case. We give one example here: in Figure 3.10 we plot the difference between the data and best-fit $L_{X,500}$–T_X–I_0 relation and the best-fit CC temperature-scaled $L_{X,500}$–T_X relation versus two substructure measures, centroid variation and axial ratio. It is clear that the L_X–T_X–I_0 relation is not masking any increase in scatter in high-substructure clusters. Similar results are

seen for other scaling relations; we thus choose to focus on the $\mathcal{O}$–T_X–I_0 scaling relations for our study of merger-related scatter below.

3.5.3 Substructure and Scaling Relations: Individual Cluster Relations

We now look for merger-related structural variations in all scaling relations. Figure 3.11 shows the natural logarithmic deviation of each data point from the best fit scaling relation for our sample plotted versus centroid variation, and Figure 3.12 shows the deviation versus axial ratio. The most obvious feature of these data is the semi-separation of CC and NCC clusters by substructure indicator; i.e., the CC clusters tend to have smaller centroid variations than the NCC clusters. This relationship between cool core status and axial ratio is not as striking, but is still present.

Figs. 3.11 and 3.12 show no qualitative evidence for an increase in scatter in clusters with higher substructure, and indeed suggest greater scatter in clusters with less substructure. There may be a trend for the most irregular clusters to lie above the scaling relation, but the small number of clusters involved (2–3) makes this very uncertain. Cluster deviations from scaling relations versus $P_1^{(pk)}/P_0^{(pk)}$and P_2/P_0 (not plotted here) likewise show no suggestion of higher scatter in clusters with greater substructure.

To quantitatively address the issue, we measure the intrinsic scatter in the scaling relations for subsamples grouped by centroid variation, axial ratio, $P_1^{(pk)}/P_0^{(pk)}$, and P_2/P_0. As before, we add a value for the intrinsic scatter $\sigma_{\rm int}$ in quadrature to the uncertainty in the observable due to measurement and temperature uncertainty, and find the value of $\sigma_{\rm int}$ that results in a reduced χ^2 value of unity for each scaling relation. We express $\sigma_{\rm int}$ in units of natural logarithm of the observable, i.e., the units of the vertical axes in Figs. 3.11 and 3.12.

We split the sample into two subsamples for each substructure measure; the split point for each is chosen to include roughly half the clusters in the sample. Specifically, we split the sample at $w = 0.02$, $\eta = 0.875$, $P_1^{(pk)}/P_0^{(pk)} = 300$, and $P_2/P_0 = 20$. Note that for the axial ratio η, a higher value corresponds to a more regular (spherical) cluster, whereas for the other substructure measures a higher value is, roughly speaking, a messier cluster. Table 3.6 contains the results; for ease of interpretation, a graphical representation of the same data is shown in Fig. 3.13. As in Table 3.4, we give the percent significance level at which equality of subsample variances is rejected.

Broadly speaking, we find greater scatter in clusters with less substructure; with 11 relations and four substructure measures, we find significantly (i.e., same scatter rejected at $> 68\%$ level) greater scatter in low substructure clusters in 13 cases, and in high substructure clusters in only four. This is remarkable, although it is not surprising in light of our earlier result (§3.3) that there is greater scaling relation scatter in the CC

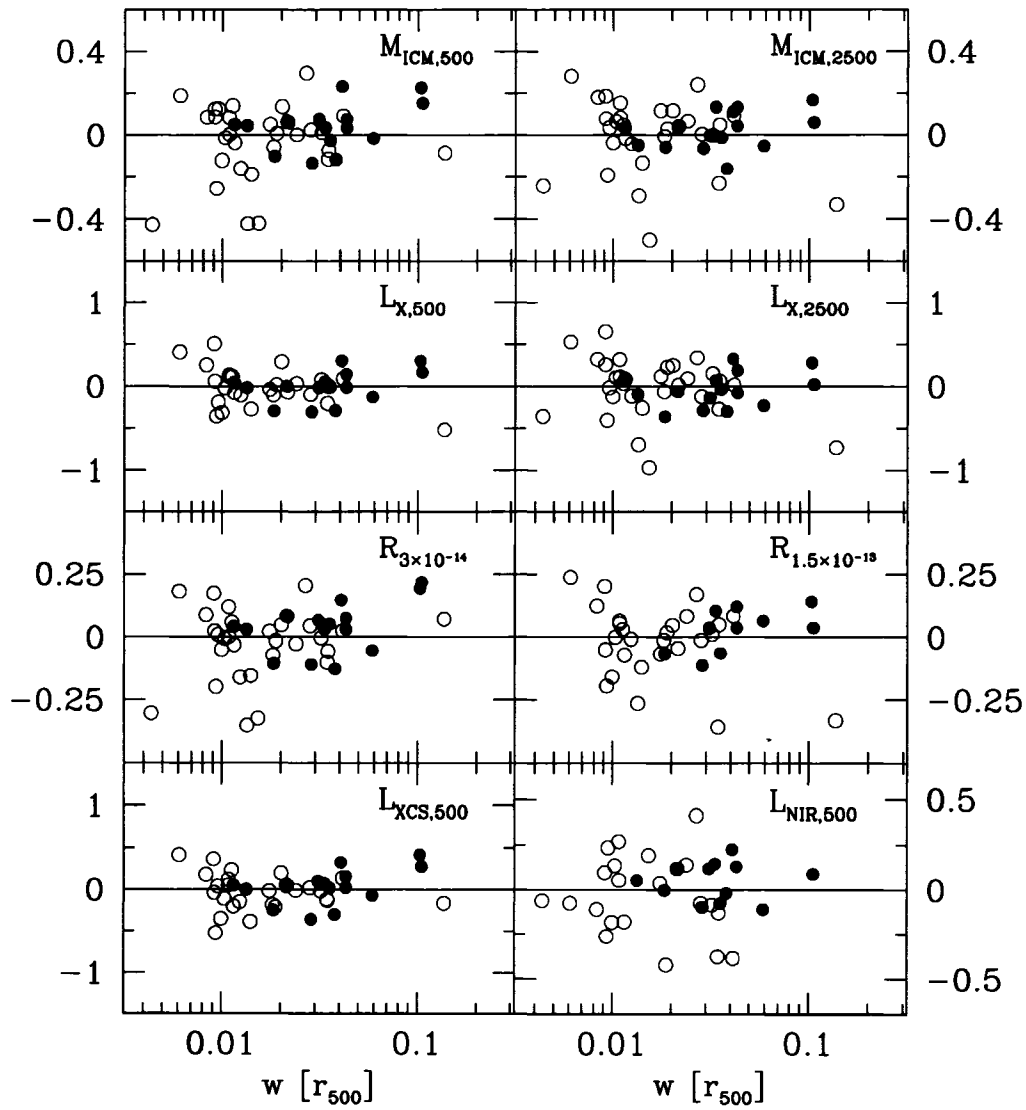

Figure 3.11 — Logarithmic (base-e) deviations of clusters from best fit scaling relations versus centroid variation w for each of the seven X-ray observable–temperature–brightness scaling relations and the NIR luminosity–temperature–brightness relation. Open and filled markers are CC and NCC clusters, respectively. Centroid variations are given in units of r_{500}.

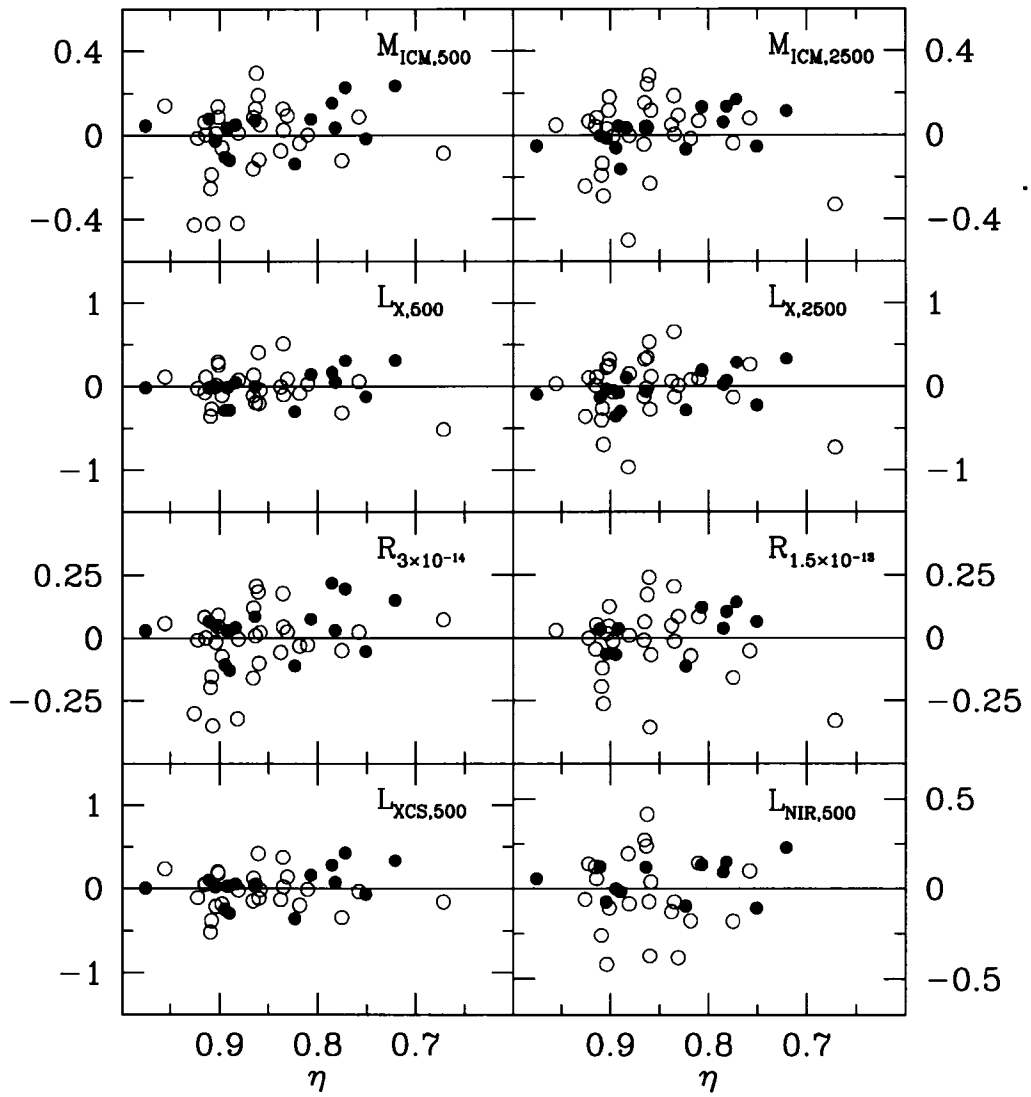

Figure 3.12 — Logarithmic (base-e) deviations of clusters from best fit scaling relations versus axial ratio η for each of the seven X-ray observable–temperature–brightness scaling relations and the NIR luminosity–temperature–brightness relation. Open and filled markers are CC and NCC clusters, respectively. Axial ratio increases to the left, i.e., ellipticity increases to the right.

Table 3.6. Intrinsic Scatter in Scaling Relations, Split By Substructure

Scaling Relation	$\sigma_{\rm int}$											
	Split by w			Split by η			Split by $P_1^{(pk)}/P_0^{(pk)}$			Split by P_2/P_0		
	L	H	Diff.(%)[a]	L	H	Diff.(%)[a]	L	H	Diff.(%)[a]	L	H	Diff.(%)[a]
Observational sample												
$M_{\rm ICM,500}$–$T_{\rm X}$–I_0	0.18	0.12	95.5+	0.18	0.13	79.2+	0.15	0.15	2.5-	0.15	0.15	8.4+
$M_{\rm ICM,2500}$–$T_{\rm X}$–I_0	0.18	0.11	96.1+	0.15	0.15	4.6-	0.14	0.15	17.9-	0.14	0.16	48.9-
$L_{\rm X,500}$–$T_{\rm X}$–I_0	0.32	0.18	98.4+	0.16	0.31	99.4-	0.31	0.17	99.1+	0.30	0.19	94.9+
$L_{\rm X,2500}$–$T_{\rm X}$–I_0	0.45	0.19	100.0+	0.32	0.38	57.8-	0.38	0.31	61.7+	0.41	0.28	91.6+
$L_{\rm XCS,500}$–$T_{\rm X}$–I_0	0.26	0.18	86.2+	0.19	0.24	69.9-	0.25	0.19	77.4+	0.24	0.20	57.7+
$R_{3\times10^{-14}}$–$T_{\rm X}$–I_0	0.16	0.10	93.1+	0.14	0.12	57.6+	0.12	0.14	51.9-	0.14	0.12	42.4+
$R_{1.5\times10^{-13}}$–$T_{\rm X}$–I_0	0.15	0.14	21.1+	0.09	0.17	98.3-	0.13	0.16	56.6-	0.13	0.16	65.4-
$L_{\rm NIR,500}$–$T_{\rm X}$–I_0	0.20	0.21	16.8-	0.18	0.22	57.0-	0.21	0.20	18.1+	0.19	0.22	43.9+
$M_{\rm ICM,500}$–$R_{3\times10^{-14}}$	0.06	0.05	37.1+	0.05	0.06	28.8-	0.05	0.06	82.3-	0.05	0.06	8.7-
$L_{\rm XCS,500}$–$R_{3\times10^{-14}}$	0.05	0.05	10.5-	0.05	0.06	28.2-	0.05	0.05	37.6-	0.05	0.05	15.1-
$L_{\rm NIR,500}$–$R_{3\times10^{-14}}$	0.19	0.14	72.2+	0.20	0.14	82.0+	0.16	0.17	14.7-	0.17	0.16	17.8+
Simulated cluster sample												
$M_{\rm ICM,500}$–$T_{\rm X}$	0.21	0.21	6.0+	0.21	0.20	10.9+	0.24	0.17	87.4+	0.22	0.19	39.5+
$L_{\rm XCS,500}$–$T_{\rm X}$	0.26	0.30	56.1-	0.25	0.30	59.3-	0.23	0.31	78.1-	0.27	0.29	29.4-
R_I–$T_{\rm X}$	0.09	0.11	62.6-	0.10	0.11	54.8-	0.11	0.10	12.4+	0.10	0.11	26.4-

Note. — L and H are low substructure (low w, $P_1^{(pk)}/P_0^{(pk)}$, and P_2/P_0, and high η) and high substructure, respectively.

[a]Percent likelihood that scatter measurements for low and high substructure subsamples are different; see text. Plus sign indicates that low substructure sample scatter is higher; minus sign indicates that high substructure sample scatter is higher.

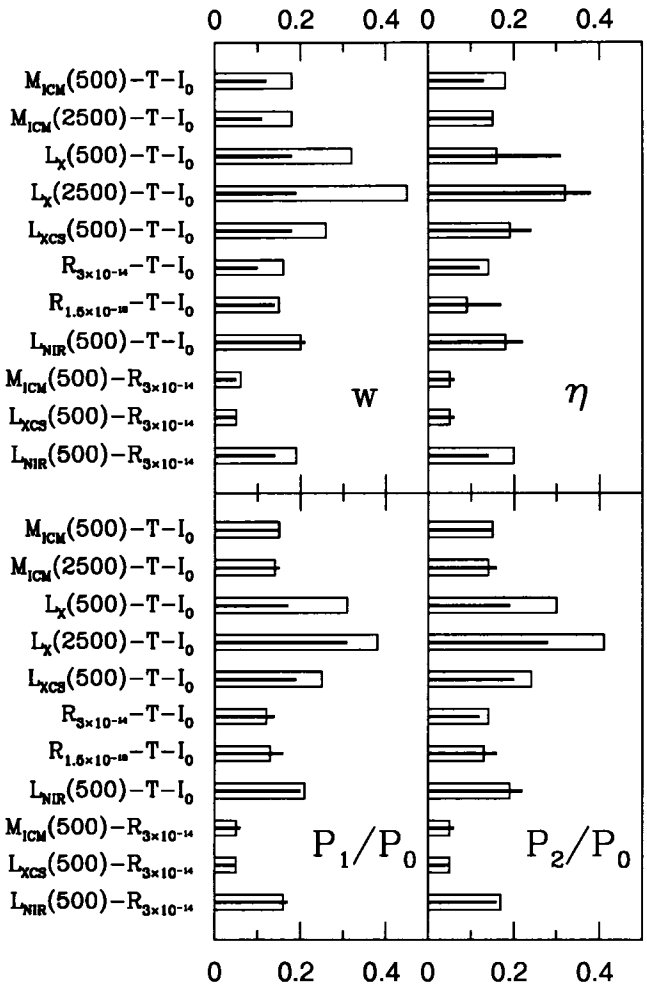

Figure 3.13 — Graphical representation of the observational sample data in Table 3.6. Open and closed bars are for low-substructure and high-substructure populations, respectively.

population than in the NCC population. One might suspect that a few outliers or a poor choice of splitting values could cause an apparent increase in scatter in lower substructure clusters, but an examination of Figure 3.11 does not support this. Indeed, while the scatter measurements suggest that clusters with higher ellipticity may have greater scatter, Figure 3.12 suggests that this is a result of a few outliers, and does not constitute a general trend to higher scatter in more elliptical clusters.

One way to minimize the effects of the cool cores is to examine observables that are least affected by the cool cores. We examine deviation in R_I from the $R_{3\times10^{-14}}$–$M_{\mathrm{ICM},500}$ scaling relation that was plotted in Figure 3.6. The emission-weighted mean temperature does not appear in this analysis, and these two observables are very insensitive to the core structure of the ICM. Deviations from this scaling relation are plotted versus centroid variation in Figure 3.14. Total scatter in this relation is smaller than for any of the

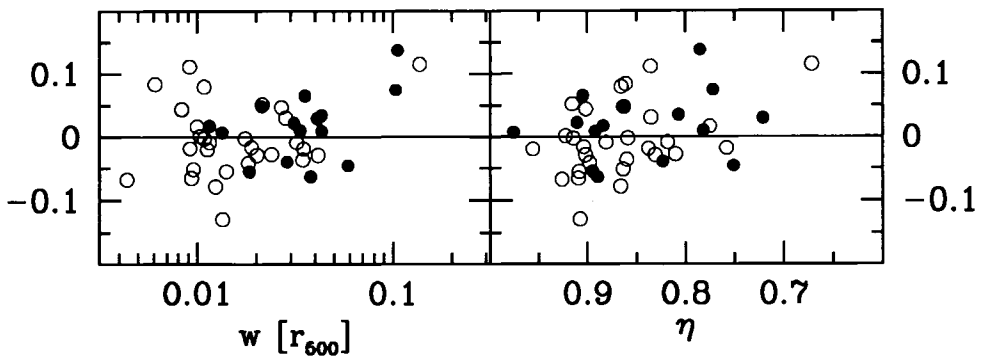

Figure 3.14 — As in Fig. 3.11, but for deviation in R_I from the $R_{3\times10^{-14}}$–$M_{\rm ICM,500}$ scaling relation.

observable–temperature relations, providing another indication that is it the core structure of clusters which varies most significantly within the population. The cluster deviation versus w provides some indication of higher scatter at lower substructure. We do see the same suggestion of a preferential boosting above the scaling relation for a few clusters at high w as for the observable–temperature relations discussed above. We also examine scaling relations constructed from $R_{3\times10^{-14}}$-$L_{\rm XCS,500}$ and $R_{3\times10^{-14}}$-$L_{\rm NIR,500}$; these, too, show little if any separation between CC and NCC populations, and exhibit little evidence for different scatter for populations with different levels of substructure.

In summary, the evidence clearly does not support our naive expectation that clusters with more substructure should exhibit higher scatter than their more relaxed counterparts.

3.5.4 Substructure and Multiple Scaling Relations

Although we have shown that the clusters with the most substructure do not preferentially deviate from individual scaling relations, it is possible that within the hyperspace defined by our broad range of observables these merging systems may have a tendency to lie somewhat further from the general population. We examine this possibility by combining cluster deviations from all the scaling relations and probing for greater combined deviations in systems with the most substructure. To do this we assume that the cluster behavior about a scaling relation is a probabilistic indication of the consistency of that cluster with the typical structure of the population. Specifically, we assume that the probability of finding a cluster at a given deviation is described by a Gaussian in log space centered on the relation with a full-width at half-maximum equal to $2.354\sigma_{\log\mathcal{O}}$, where $\sigma_{\log\mathcal{O}}$ is the intrinsic scatter of the population about the scaling relation. That is, we

calculate

$$P_{\mathcal{O}} = \frac{1}{\sqrt{2\pi}\sigma_{\log \mathcal{O}}} \exp\left[-\frac{1}{2}\left(\frac{\log \mathcal{O} - \log \mathcal{O}_{\rm fit}(T_{\rm X})}{\sigma_{\log \mathcal{O}}}\right)^2\right] \tag{3.14}$$

for an observable $\mathcal{O}$. We also calculate $P_{\rm total}$, a measure of the significance of deviation from multiple scaling relations together, by multiplying the individual probability amplitudes. If a cluster deviates slightly from three individual relations, for example, this should be reflected in $P_{\rm total}$. This approach assumes that the cluster behavior about each scaling relation is an independent indicator of its deviation from the whole population.

We find no correlation between deviation from scaling relations and substructure for any individual $\mathcal{O}$–$T_{\rm X}$ scaling relation, or for all observables measured together. The three highest substructure clusters noted in the previous discussion do indeed have low total probability densities, as expected, but this is also true of several other clusters over the entire range of substructure in our cluster sample. We conclude that there is no readily discernible relationship between substructure and deviation from scaling relations by individual clusters.

3.5.5 Hydrodynamical Cluster Simulations

Although simulated clusters do not exhibit the full complexity of real clusters, carrying out our analysis on a controlled sample of well-understood systems is an important component of our work. We use a simulated cluster ensemble consisting of 45 smoothed particle hydrodynamics simulations evolved in a ΛCDM cosmology; details of the techniques used and of this particular sample can be found in Bialek et al. (2001, 2002). These simulations have resolution sufficient to exhibit cluster merger features such as cold fronts (Bialek et al. 2002). They do not include any ICM cooling mechanism, and hence cool cores will be absent; this provides a good opportunity to examine the results that would be expected in our observational sample if we were able to completely remove the cool core effects. Lack of resolution and incomplete physical modeling make the central, core regions of simulated clusters unreliable, and so we choose to examine scaling relations that are less sensitive to these core regions.

We examine the projected *ROSAT*-band (0.5–2.0 keV) core-subtracted luminosity within r_{500}; that is, without the luminosity projected within $0.20r_{500}$, as in our observed cluster sample. We derive the scaling relation for $M_{\rm ICM,500}$ using the actual simulation data (i.e., not calculating $M_{\rm ICM}$ from mock observations). We measure the isophotal size in the *ROSAT* band corresponding to an isophote of 1×10^{-3} counts s^{-1} arcmin^{-2}; this instrumental isophote leads to isophotal sizes that approximately match the normalization of the observed $R_{3\times10^{-14}}$–$T_{\rm X}$ relation. This isophote generally lies well outside the core of the simulated clusters.

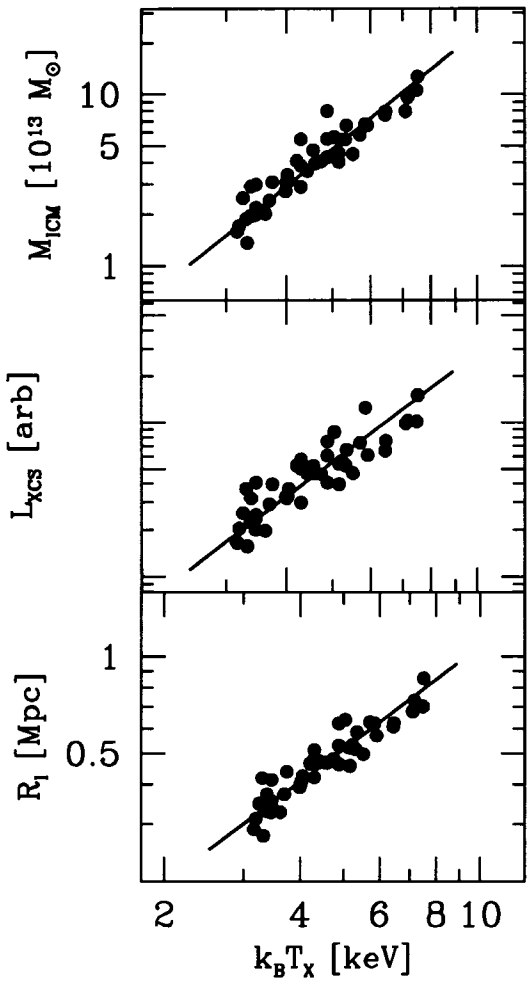

Figure 3.15 — Simulated scaling relations for $M_{\rm ICM}$ within r_{500}, core-subtracted X-ray luminosity projected within r_{500}, and isophotal size for an isophote of 1×10^{-3} counts s^{-1} arcmin^{-2}, versus $T_{\rm X}$.

Scaling relations for these three observables are shown in Figure 3.15. As we did for the observed scaling relations, in Figure 3.16 we plot the difference between each cluster and the best-fit relations versus the w and η substructure indicators. There is some suggestion here of a trend toward greater scatter at higher substructure. To quantify this, we calculate the intrinsic scatter as was done for the observations, both for the entire sample and for subsamples of roughly equal size; values of $\sigma_{\rm int}$ are shown in Table 3.6.

Looking at all four substructure measures, there is a tendency toward lower scatter in clusters with less substructure. However, in general the quantitative differences are rather small; significantly ($> 68\%$ significance) different subsample scatter is found in only two relations, and greater scatter in low substructure clusters in only one. We also calculate the probability amplitude for individual clusters by combining information from all scaling relations, as we did for the observations. This approach provides no suggestion

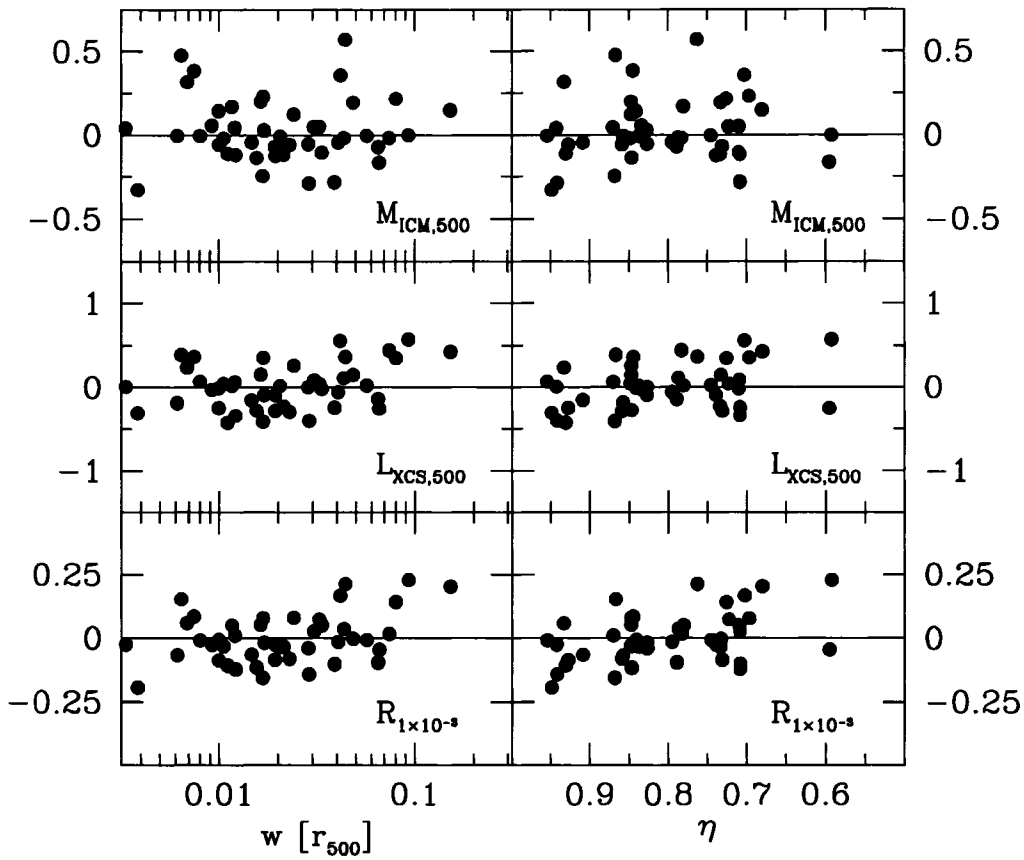

Figure 3.16 — Deviation in base-e logarithm of simulated clusters and from best-fit relations plotted versus centroid variation w and axial ratio η for each of the three simulated X-ray scaling relations. Centroid variation is given in units of r_{500}.

of greater or smaller deviation for clusters with less substructure. Thus, while the simulations do not show evidence for greater scatter in clusters with more substructure, they also do not show the tendency toward higher scatter in less messy clusters that we see in the observed cluster sample.

The scatter we measure in the simulated sample can be compared directly to the intrinsic scatter in the observed samples. Because of the lack of radiative cooling in the simulations, it is likely best to compare the simulation scatter to the cool core "corrected" observations (i.e., the scatter in the $\mathcal{O}$–T_X–I_0 relations). Agreement in the scatter of simulated and observed scaling relations would serve as one more indication (along with the slope and normalizations; Bialek et al. 2001) that the simulations are an accurate representation of real clusters. Interestingly, the scatter is greater for the simulations in mass (0.20:0.14) and luminosity (0.27:0.21), and smaller in isophotal size (0.10:0.13). The comparison is not entirely appropriate in the case of the ICM mass, because in the simulations we use the actual three dimensional ICM mass measured within r_{500}, and for the observations we calculate this through a deprojection. The bottom line

is that although these simulations with early and uniform preheating do a good job of reproducing the observed slopes and amplitudes of scaling relations, there is still clearly work to be done to match the scatter in observed scaling relations. The range of missing physics in the simulations includes radiative cooling, conduction, magnetic fields, feedback from AGN, galaxy formation, etc., and all of these must be considered together with the effects of finite spatial resolution. It is quite interesting to consider that some ingredients currently missing from simulations could actually reduce the scaling relation scatter—that is, reduce the cluster to cluster structural variations at a given mass.

3.5.6 Summary of Substructure Results

We have shown that clusters with greater substructure do not preferentially lie significantly farther from scaling relations than clusters with less substructure. In fact, in observed clusters, there is a tendency toward greater scatter about scaling relations in apparently more relaxed clusters. These findings contradict the naive expectation that cluster structure is greatly disturbed by merger events and so should increase scaling relation scatter.

Comparison of the observational and simulated cluster samples suggests that the greater scatter in more apparently relaxed clusters must be the result of processes not present in the simulations. Cool core-related phenomena are clearly the prime candidate for the higher scatter seen in observed clusters with less substructure, especially as our results show unquestionably higher scatter in CC clusters when compared to NCC clusters. AGN activity may also contribute, as AGN occur frequently in the cluster population and can produce radio cavities with associated energies of at least $\sim 10^{60}$ erg (Bîrzan et al. 2004).

However, even the simulations show only weak evidence of higher scatter in clusters with more substructure. We must conclude that either there are mechanisms which introduce a range of structural variations into apparently relaxed clusters, or that mergers simply do not perturb cluster structure to the extent expected and suggested by simulations of isolated clusters (Ricker & Sarazin 2001; Randall et al. 2002).

It may be suggested that the use of archival temperatures from different sources may introduce scatter or otherwise hide merger or cooling effects. Redoing the $L_{X,500}$ portion of our analysis with 43 of 45 temperatures taken from a single published source (White 2000) demonstrates that this is not the case; while quantitative scatter measurements can be sensitive to outliers, we find no evidence that the qualitative trends we report are affected by moderate shifts in cluster temperatures.

3.6 Conclusions

We examine the relationship between substructure and cool cores in galaxy clusters and the scatter about X-ray and near-IR scaling relations using emission-weighted, non-spatially resolved, non-cooling corrected temperatures. We separate clusters into CC and NCC subsamples according to their central cooling times, and we quantify substructure using the centroid variation, axial ratio, and power ratios $P_1^{(pk)}/P_0^{(pk)}$ and P_2/P_0. With these tools and a wide range of crude cluster observables and uncertainties, we examine a large number of galaxy cluster scaling relations in an approximately X–ray flux limited sample of 45 clusters. Our primary findings are:

1. There is an offset between CC and NCC populations on all observable–temperature scaling relations that we examine. This separation is partly due to an emission weighted mean temperature bias at around the 7% level. The offset must also be due to differences in the core structure of the two subsamples, because those scaling relations that are most sensitive to the cluster core show the largest offsets. This offset is not driven by recent mergers, because scaling relations involving observables that are sensitive primarily to the outer structure of clusters show larger scatter in the CC population.

2. We show that the central X–ray surface brightness can be used to characterize the "strength" of cool cores, and that introducing it as a third parameter in observable–temperature scaling relations greatly reduces the scatter about those relations. Thus, the central surface brightness provides a tool for studying the evolution of cluster scaling relations in a manner less sensitive to any change in the fraction of cool core clusters with redshift. In addition, the small scaling relation scatter when using the surface brightness means that crude cluster observables like the X–ray luminosity and temperature can provide more accurate virial mass estimates than are obtained without the third parameter.

3. Parameterized in terms of central surface brightness I_0, we find that the emission weighted mean temperature bias correction factor is proportional to $I_0^{(0.03\pm0.01)}$. Given the factor of $\sim$500 variation in I_0 within our sample, this implies a maximal differential correction across our sample of $\sim$ 20%. Using the median I_0 for the CC and NCC populations, we calculate an average CC temperature bias factor of 1.07 ± 0.02 for this sample.

4. We find that although CC clusters tend to exhibit less morphological substructure, they exhibit at least as much scatter as (and often more than) the NCC clusters. Thus, structural variations among CC clusters are at least as large as the structural variations among NCC clusters. This result has important implications for analyses which rely on the presence of a cool core to indicate that a cluster is relaxed.

5. Clusters with greater morphological substructure do not exhibit more scatter about scaling relations than clusters with lower substructure. In fact, we observe a trend toward higher scatter in clusters with less substructure. This may be partially due to the structural variations within cool cores, which are typically found in clusters that exhibit less substructure; however, even after using central surface brightness to reduce the systematic cool core effects, we find that the clusters with less substructure exhibit as much or more scatter as those with more substructure.

6. The differences between low and high morphological substructure clusters are modest in our study of hydrodynamical cluster simulations without cooling; there is only a weak indication that those clusters with higher substructure exhibit higher scatter.

7. As in the purely X–ray scaling relations, there is no relationship between deviation from the $L_{\rm NIR}$–$T_{\rm X}$ relation and cluster substructure. However, in the NIR relation there is a negative temperature scale factor required to align the CC and NCC populations, and a lack of any dependence on I_0 in a constructed $L_{\rm NIR}$–$T_{\rm X}$–I_0 relation. Because we know that emission-weighted mean temperatures are biased by the cool core gas in CC clusters, this suggests a difference between galaxy populations in CC and NCC clusters. A detailed study of differences in NIR properties of the galaxy population in CC and NCC clusters would clearly be interesting.

Together, these results from studies of real and simulated clusters indicate that cool core related phenomena (such as radiative cooling, AGN activity, and entropy injection at an earlier epoch), and not cluster merging, are the primary sources of scatter in scaling relations. Perhaps it should come as no surprise that X–ray observables that arise from emission, which is sensitive to the square of ICM density, are most perturbed by the detailed structure of the cluster core. However, the lack of a strong substructure related enhancement of scatter in scaling relations without sensitivity to the cluster core and in hydrodynamical simulations of clusters, is surprising. It suggests that perhaps all clusters retain departures from equilibrium at a significant enough level that even recent mergers do not perturb their structure enough to make them appear unusual. A young population with relaxation timescales that are comparable to the time since the last major merger would presumably exhibit this kind of behavior.

Reconciling these observations and our conclusions with high resolution hydrodynamical mergers of idealized clusters (e.g., Ricker & Sarazin 2001) requires a rarity of such large-scale mergers or perhaps additional physics within the ICM that suppresses the boosts. Note that correlated excursions in luminosity and temperature during a merger will not suffice as an explanation, because we have shown using 8 different observable–temperature scaling relations that there is no strong relationship between substructure and scal-

ing relation scatter. We have demonstrated here that lower resolution hydrodynamical simulations simply do not produce large deviations from the general cluster population even when there is evidence for significant substructure, either in individual clusters or in the high-substructure cluster population as a whole. Whatever the explanation, it is clear from reasonably large samples of real clusters that there are no outliers on the scale of those predicted by the high resolution, idealized cluster merger simulations.

Our result may be consistent with the scenario where NCC clusters evolve to become CC clusters in the absence of major mergers (e.g., Ota et al. 2006). However, the larger scatter we observe for CC clusters in all scaling relations raises important questions. In particular, even after using the central surface brightness to correct for CC effects, we still observe higher scatter about the CC relations (see Table 3.4). Moreover, we see the larger scatter in CC clusters even in scaling relations that involve observables that are not sensitive to the core structure (i.e., faint isophotal size, ICM mass within r_{500}, and NIR light). Thus, if CC clusters evolve from NCC clusters because of an absence of mergers, then the observations require some other source of scatter or variation in cluster structure to be present throughout the cluster virial region.

Alternatively, cool cores may arise through a scenario that is driven by something other than the recent merger history of the cluster. McCarthy et al. (2004) suggest that variations in entropy injection into the intracluster medium could determine whether or not a cool core forms. This varied entropy injection would also contribute to structural variations or scatter in scaling relations. Because our cluster sample indicates that it is the CC clusters which exhibit the highest scatter around scaling relations (even those relations with little core sensitivity), it seems likely that this or some similar, non-merger driven scenario is responsible for the presence or absence of cool cores in clusters. Within this scenario the tendency for cool core clusters to exhibit less morphological substructure would be primarily due to the effects of the often dominant X-ray bright core, which would tend to bias axial ratios high and centroid variations low. That is, in cool core clusters a morphological substructure indicator is in large part reflecting the characteristics of the bright, symmetric core.

It will be quite interesting to return to this question of the dual nature of galaxy clusters—youthful as indicated by the high frequency of morphological substructure, yet strikingly regular as indicated by scaling relations—with new tools and larger samples extending over a wider range of redshift. Of particular interest will be the additional leverage afforded by the new generation of high signal to noise Sunyaev-Zel'dovich effect observations, which should be dramatically less core-sensitive than X–ray observations. With the tens of thousands of clusters expected in dedicated surveys, it should be possible to quantify with high significance any subtle, merger related trends that may be present.

This work makes use of data products from the Two Micron All Sky Survey, which is a joint project of the University of Massachusetts and the IPAC/Caltech, funded by NASA and the NSF.

Chapter 4

Evolution of the Intracluster Medium Between 0.2 < z < 1.3 in a Chandra Sample of 70 Galaxy Clusters

We study the evolution of the intracluster medium (ICM) with a uniformly analyzed sample of 70 galaxy clusters spanning $0.18 < z < 1.24$ and observed with *Chandra*. We find that X-ray luminosity and ICM mass at a fixed temperature evolve with redshift in a manner inconsistent with either the standard self-similar model of cluster formation or a model that assumes no evolution of cluster structure. Both luminosity and ICM mass evolve more slowly than the self-similar prediction, i.e., clusters have lower luminosity and ICM mass at fixed emission-weighted temperature than expected at higher redshifts. We find that evolution in these two observables can be modeled by a simple evolution in the cluster gas mass fraction, evolving as $(1+z)^{-0.39\pm0.13}$ when measured using core-subtracted observables. Excluding cluster cores from measurements results in more positive evolution than when the entire cluster is used, indicating that the fraction of clusters with cool cores increases with time, or that cool cores become more developed over time in those clusters that have them; this is supported by direct study of the redshift dependence of central surface brightness, which increases in scatter and magnitude at low redshift. We find that isophotal size–temperature relations evolve differently according to which isophote is used, indicating evolution in the distribution of the ICM. We show that constraints on the evolution of the gas fraction and isophotal size–temperature relations constraints can be combined to measure cluster distances, and thus to constrain cosmological parameters in a way complementary to other techniques. Scatter in scaling relations is considerably reduced by using either core-subtracted quantities or three-parameter relations including the central surface brightness; in addition, scatter decreases at higher redshifts. Our results provide constraints for simulations attempting to model cluster physics, and indicate some difficulties for cosmological studies that assume constant cluster gas fractions, while pointing toward other potentially more robust uses of clusters for cosmological applications.

4.1 Introduction

Scaling relations among bulk properties of galaxy clusters provide a powerful means to test models of the large-scale structure and evolution of the universe. These correlations among properties such as X-

ray luminosity, intracluster medium (ICM) mass, mean ICM temperature, and cluster virial mass reflect gravitational and non-gravitational processes involved in the formation of structure in an expanding universe. Scaling relations also provide the means to readily estimate masses of clusters from much more easily measured properties such as luminosity, an essential component of cosmological studies that use X-ray observations to determine the redshift evolution of the cluster mass function.

Simple models of cluster formation via gravitational collapse predict particular forms for the redshift evolution of cluster scaling relations (Kaiser 1986). Adding additional cluster physics such as radiative cooling of the ICM, and energy injection by active galactic nuclei (AGN), supernovae, and star formation, modifies these predictions (e.g., Cavaliere et al. 1998; Ettori et al. 2004a; Muanwong et al. 2006; Kay et al. 2007). Observational studies of scaling relation evolution are required to properly constrain models of cluster evolution and to understand the effects of non-gravitational processes on the scaling relations that will be used to study cosmology. X-ray studies of the ICM are complementary to studies of the evolution of the cluster galaxy population (e.g., de Propris et al. 1999; Lin et al. 2006), helping to constrain the overall evolution of cluster baryons and their distribution in various forms within clusters.

Several studies of X-ray scaling relation evolution have been carried out in recent years (e.g., Vikhlinin et al. 2002; Ettori et al. 2004b; Kotov & Vikhlinin 2005; Maughan et al. 2006; Morandi et al. 2007; Branchesi et al. 2007), but no clear consensus has emerged. In this paper we will address scaling relation evolution using a systematic analysis of a *Chandra* sample of 70 clusters covering $0.18 < z < 1.24$, the largest sample yet used for this purpose.

Our study addresses two difficulties which may affect scaling evolution measurements. The first arises from the fact that radiative cooling of the ICM leads to the development of cool, dense (and hence very luminous) cores in many clusters; these relatively small cores bias cluster measurements such as X-ray temperature and luminosity to an extent that they are not representative of the overall cluster structure. This introduces significant scatter into scaling relations; indeed, there is evidence that cool core clusters, which are traditionally regarded as "relaxed", actually exhibit greater structural variation than non-cool core clusters, which are often thought to have recently undergone major mergers (O'Hara et al. 2006). Studies of scaling relations commonly attempt to "correct" for the impact of cool cores on cluster properties by one of several methods, such as simply leaving clusters with evidence for strong cool cores out of the sample (e.g., Arnaud & Evrard 1999), or excising central regions within a fixed metric radius (e.g., Morandi et al. 2007) or a fraction of the virial radius (e.g., Maughan et al. 2007), and perhaps "correcting" measured luminosity by some factor determined from a model of the cluster surface brightness distribution (e.g., Vikhlinin et al. 2002). In this paper we measure temperatures with and without cores defined as fractions of the virial

radius, and we also measure luminosities with and without the same core. By using relations both with and without core subtracted quantities, we can examine the effects that core development has on cluster scaling relation slopes and evolution.

The other issue usually faced by scaling relation studies is the use of scaling relation slopes and normalizations from low-redshift studies carried out with different instruments. The relatively small fields of view of *Chandra* and *XMM-Newton* make measurements of local samples quite challenging with those instruments; hence, studies using older X-ray instruments are used as references for $z = 0$ relations. Unfortunately, differences in spectral and imaging results among X-ray instruments are well established, making such approaches subject to instrument-related systematics; indeed, even the same instrument has produced results differing by the author, as calibrations change and varying reduction and analysis methods are adopted. By using a large sample (70 clusters), we can avoid the use of outside references for scaling relation parameters or the direct inclusion of data from other samples, in favor of a single, homogeneously analyzed sample. While this approach is not entirely new—for example, Branchesi et al. (2007) studied evolution using their own 17 cluster sample both with and without the inclusion of data from other studies; and Morandi et al. (2007) studied a homogeneously reduced 24 cluster sample—the size of our sample leads to significantly smaller uncertainties on scaling relation parameters than have otherwise been obtained.

In §4.2 we provide a brief overview of scaling relations and their predicted evolution, and in §4.3 we explain our data reduction and measurement procedures. We test for scaling relation evolution with respect to expectations from the self-similar theory and from a scenario of no evolution in cluster parameters in §§4.4 and 4.5, respectively, and provide an explanation for observed evolution in scaling relations via a simple evolution in the gas mass fraction §4.6. In §4.7 we examine the evolution of isophotal size, and discuss the implications for studying cosmology using size measurements, and in §4.8 we discuss the effectiveness of two different methods of reducing the scatter in measured scaling relations. In §4.9 we compare our results to previous observations and simulation results, and discuss some implications of our findings. Finally, we list our conclusions in §4.10.

We adopt the *WMAP* + LRG ΛCDM cosmology from Spergel et al. (2007), which combines the third year *WMAP* data with results from the SDSS luminous red galaxy survey (Eisenstein et al. 2005) to give $H_0 = 70.9$ km s^{-1} Mpc^{-1}, $\Omega_M = 0.266$, and $\Omega_\Lambda = 0.734$. All uncertainties are 68% confidence, unless specified otherwise.

4.2 Scaling Relation Background

The self-similar model (e.g., Kaiser 1986) describes formation of clusters via gravitational collapse of overdense regions in an expanding universe. In this model the ICM is heated by this gravitational collapse and the resulting shock heating, but no non-gravitational heating is assumed. As a result, clusters scale self-similarly, i.e., they scale only because of changes in their physical size at fixed mass due to density variation as the universe expands. With the assumptions of spherical symmetry, hydrostatic equilibrium, a constant gas fraction, and X-ray emission dominated by thermal bremsstrahlung, this leads to X-ray luminosity $L_{\rm X}$ and ICM mass $M_{\rm ICM}$ scaling with ICM temperature $T_{\rm X}$ and redshift as

$$L_{\rm X} \propto T_{\rm X}^2 E(z), \tag{4.1}$$

$$M_{\rm ICM} \propto T_{\rm X}^{3/2} E(z)^{-1}, \tag{4.2}$$

where $E(z)$ is the ratio of the Hubble parameter at redshift z to its present value. In a flat cosmology with matter density $\Omega_{\rm m}$, $E(z)$ has the form:

$$E(z) = H(z)/H_0 = \left[\Omega_{\rm m}(1+z)^3 + 1 - \Omega_{\rm m}\right]^{1/2}. \tag{4.3}$$

Predicting scaling laws for the isophotal size (i.e., the physical size of the region corresponding to the angular size of a particular X-ray isophote; see §4.3.5) requires additional assumptions about the ICM mass distribution. With the commonly used isothermal β model, isophotal size scales as

$$R_I \propto T_{\rm X}^{2/3}, \tag{4.4}$$

with no redshift dependence, when the cluster has a typical value of $\beta = \frac{2}{3}$ (Mohr et al. 2000).

Observational studies have found that scaling relations for all three of these observables ($L_{\rm X}$, $M_{\rm ICM}$, and R_I) in fact have a stronger dependence on temperature than predicted by self-similar models (e.g., Edge & Stewart 1991; Markevitch 1998; Mohr & Evrard 1997; Mohr et al. 1999). Explanations for this and other evidence of non-gravitational processes, such as the presence of entropy ramps in the central regions of clusters (e.g., Ponman et al. 2003), typically involve additional non-gravitational energy injection by active galactic nuclei (AGN), supernovae, and star formation (e.g., Bialek et al. 2001; Bower et al. 2001; Borgani et al. 2002; McCarthy et al. 2004; Kay et al. 2007); radiative cooling of the ICM, which leads to the formation of cool, dense cores in many clusters; and non-radiative cooling (e.g., Bryan 2000).

It is important to note that there are multiple ways to define radii for measuring cluster parameters, which result in different predicted redshift evolution for scaling relations. The expressions given above are correct for observables (L_X and M_{ICM}) measured within regions corresponding to fixed overdensities relative to the critical density. This is appropriate for our strategy in this paper, in which we choose to measure cluster properties within virial regions defined by local relations, and then test for consistency with the evolution scenarios described below. Another commonly used form for the redshift evolution of scaling relations (e.g., Ettori et al. 2004b; Branchesi et al. 2007; Morandi et al. 2007) uses densities defined from assumptions of virial equilibrium in a spherical collapse model. These densities have their own redshift evolution, leading to additional factors in the scaling relation evolution equations. In either case, it is common to parametrize additional redshift evolution beyond the self-similar predictions in terms of a simple power law with redshift, i.e., proportional to $(1 + z)$ raised to some power.

In this paper we discuss two models for cluster evolution. The first is "self-similar evolution", in which cluster observables scale as would be expected given purely gravitational influence as discussed above, i.e., $L_X \propto E(z)$ and $M_{ICM} \propto E(z)^{-1}$. The other is what we will refer to as "no evolution", meaning that cluster parameters, including virial radii, do not scale at all as the universe expands.

4.3 Data Reduction

4.3.1 The Cluster Sample

The data are drawn from the *Chandra* archive. The lower redshift limit of $z \sim 0.2$ reflects the difficulty in measuring cluster parameters out to at least r_{2500} for clusters closer than this, given the small *Chandra* field of view. The cluster sample is listed in Table 4.1, with the ID number of the *Chandra* observation used for each cluster.

Having been largely developed through cluster selection in archival *Einstein* IPC and *ROSAT* PSPC observations, our sample is essentially X-ray flux limited. However, as the sample is not derived from a single homogeneous survey at a fixed flux threshold, it might be worried that at higher redshifts we are including systematically more luminous (i.e., more massive) systems. In Figure 4.1 we plot the emission-weighted mean temperatures for our sample (measured as described in §4.3.3 below) versus redshift. Our sample spans a consistent range of T_X, and thus mass, over the full redshift range.

Table 4.1: Observation and Spectral Fitting Information

Cluster	z	ObsID	t_{exp}[a] (ks)	RA[b]	DEC[b]	T_X aperture (arcsec)	T_X (keV)	T_{XCS}, SS ev.[c] (keV)	T_{XCS}, no ev.[d] (keV)
A665	0.182	3586	29.6	08:30:50.2	+65:52:14	380	8.0 ± 0.2	8.1 ± 0.3	8.2 ± 0.3
A963	0.206	903	29.9	10:17:03.8	+39:02:42	195	7.0 ± 0.3	$6.8^{+0.4}_{-0.5}$	$6.8^{+0.4}_{-0.5}$
RX J0439.0+0520	0.208	527	9.6	04:39:02.3	+05:20:45	204	$4.3^{+0.4}_{-0.3}$	$4.0^{+0.9}_{-0.6}$	$4.0^{+1.1}_{-0.6}$
A1423	0.213	538	9.7	11:57:18.1	+33:36:45	256	6.0 ± 0.4	6.2 ± 0.7	$6.3^{+0.8}_{-0.7}$
ZwCl 2701	0.214	3195	18.3	09:52:49.3	+51:53:05	150	4.7 ± 0.2	5.8 ± 0.6	$6.0^{+0.7}_{-0.6}$
A773	0.217	5006	19.8	09:17:53.0	+51:43:37	257	8.3 ± 0.4	8.0 ± 0.6	$8.1^{+0.7}_{-0.6}$
A2261	0.224	5007	24.3	17:22:27.1	+32:07:56	275	$7.7^{+0.3}_{-0.2}$	7.3 ± 0.5	7.1 ± 0.5
ACO 2246	0.225	547	48.2	17:00:41.5	+64:12:53	103	$2.9^{+0.3}_{-0.2}$	$1.8^{+0.3}_{-0.2}$	$1.7^{+0.3}_{-0.2}$
A1682	0.226	3244	4.7	13:06:55.1	+46:33:01	254	$5.5^{+0.8}_{-0.4}$	$5.4^{+1.0}_{-0.6}$	$5.6^{+1.1}_{-0.6}$
A2111	0.229	544	10.2	15:39:39.6	+34:25:55	298	7.2 ± 0.7	$7.1^{+1.0}_{-0.9}$	$6.6^{+1.1}_{-0.6}$
A267	0.230	3580	19.9	01:52:42.1	+01:00:33	254	$7.1^{+0.4}_{-0.5}$	$6.8^{+1.1}_{-0.5}$	$7.1^{+0.9}_{-0.8}$
RX J2129.7+0005	0.235	552	9.9	21:29:40.1	+00:05:18	218	5.7 ± 0.3	$6.7^{+1.1}_{-0.6}$	$6.8^{+1.3}_{-0.6}$
RX J0439.0+0715	0.245	3583	19.2	04:39:00.8	+07:15:58	243	7.4 ± 0.6	$6.7^{+1.0}_{-0.7}$	$7.0^{+1.3}_{-1.0}$
A521	0.247	901	38.1	04:54:08.1	−10:14:21	360	6.0 ± 0.4	$5.4^{+0.5}_{-0.3}$	$5.4^{+0.4}_{-0.3}$
A1835	0.252	495	18.4	14:01:01.9	+02:52:41	187	8.2 ± 0.2	$16.3^{+3.3}_{-2.5}$	$16.1^{+3.6}_{-2.9}$
A68	0.255	3250	9.9	00:37:06.4	+09:09:27	260	$8.6^{+1.4}_{-0.8}$	$8.4^{+1.9}_{-1.6}$	$8.0^{+2.0}_{-1.6}$
MS 1455.0+2232	0.258	4192	91.6	14:57:15.1	+22:20:34	148	4.7 ± 0.1	5.6 ± 0.3	5.6 ± 0.3
MS 1006.0+1202	0.261	925	15.4	10:08:47.5	+11:47:34	234	6.1 ± 0.4	$6.6^{+1.1}_{-0.7}$	$6.6^{+1.4}_{-0.7}$
A697	0.282	4217	19.5	08:42:57.6	+36:21:55	276	$10.5^{+0.9}_{-0.5}$	11.9 ± 1.2	11.6 ± 1.3
A611	0.288	3194	24.3	08:00:56.8	+36:03:23	172	$8.9^{+0.7}_{-0.6}$	$11.8^{+3.6}_{-2.2}$	$12.5^{+3.3}_{-2.8}$
ZwCl 3146	0.291	909	43.7	10:23:39.6	+04:11:10	246	6.5 ± 0.1	$8.7^{+0.7}_{-0.4}$	$8.6^{+0.7}_{-0.5}$
A781	0.298	534	9.9	09:20:21.6	+30:30:20	264	$5.3^{+0.6}_{-0.4}$	$5.3^{+0.7}_{-0.4}$	$5.2^{+0.6}_{-0.4}$
MS 1008.1-1224	0.301	926	28.6	10:10:32.2	−12:39:23	196	6.4 ± 0.4	$6.5^{+0.9}_{-0.6}$	$6.6^{+1.0}_{-0.6}$
RXC J2245.0+2637	0.304	3287	14.6	22:45:04.9	+26:38:02	150	5.9 ± 0.3	$7.1^{+1.2}_{-0.9}$	$6.7^{+1.3}_{-0.8}$
A1300	0.308	3276	13.7	11:31:55.3	−19:54:46	268	$8.8^{+0.7}_{-0.6}$	$9.4^{+1.0}_{-0.9}$	$9.1^{+1.0}_{-0.9}$

Table 4.1, cont.

Cluster	z	ObsID	t_{exp}[a] (ks)	RA[b]	DEC[b]	T_X aperture (arcsec)	T_X (keV)	T_{XCS}, SS ev.[c] (keV)	T_{XCS}, no ev.[d] (keV)
A2744.....	0.308	2212	22.1	00:14:15.3	−30:22:50	235	10.1±0.6	$9.2^{+0.7}_{-0.6}$	9.3±0.7
MS 2137.3-2353.....	0.313	5250	25.6	21:40:15.2	−23:39:38	148	5.0±0.2	5.0±0.5	$5.2^{+0.3}_{-0.6}$
A1995.....	0.318	906	10.0	14:52:58.6	+58:02:58	191	$8.1^{+1.0}_{-0.8}$	$6.0^{+1.0}_{-0.8}$	$5.7^{+1.1}_{-0.8}$
ZwCl 1358+6245....	0.327	516	20.0	13:59:51.4	+62:30:53	185	$9.1^{+0.9}_{-0.8}$	...	...
A1722.....	0.328	3278	14.6	13:20:08.3	+70:04:34	203	$9.1^{+1.5}_{-1.2}$	$13.2^{+6.4}_{-4.2}$	$10.6^{+7.4}_{-2.9}$
RXC J0404.6+1109.	0.355	3269	21.8	04:04:33.7	+11:08:25	321	$5.6^{+0.8}_{-0.7}$	$5.1^{+0.9}_{-0.6}$	$5.1^{+1.0}_{-0.6}$
RX J1532.9+3021...	0.362	1649	8.1	15:32:54.0	+30:21:04	128	6.1±0.3	$8.1^{+1.6}_{-1.2}$	$7.5^{+1.6}_{-1.1}$
A370.....	0.373	515	53.9	02:39:54.5	−01:34:47	184	$8.7^{+0.5}_{-0.4}$	8.1±0.5	7.8±0.5
ZwCl 1953.....	0.374	1959	21.0	08:50:08.4	+36:04:35	214	7.6±0.5	$6.5^{+0.6}_{-0.5}$	6.2±0.5
RXC J0949.8+1707.	0.383	3274	14.3	09:49:52.4	+17:07:10	246	$7.8^{+0.7}_{-0.6}$	$8.1^{+1.2}_{-1.1}$	7.5±1.2
ClG J1416+4446....	0.400	541	29.9	14:16:28.4	+44:46:42	128	3.8±0.3	$4.5^{+0.7}_{-0.5}$	$4.3^{+0.8}_{-0.5}$
RXC J2228.6+2036.	0.412	3285	19.8	22:28:32.1	+20:37:23	244	8.1±0.5	$7.9^{+0.8}_{-0.7}$	$8.4^{+1.4}_{-0.8}$
MS 0302.7+1658....	0.426	525	10.0	03:05:31.7	+17:10:05	82	$3.6^{+0.5}_{-0.4}$	$2.8^{+0.7}_{-0.5}$	$2.7^{+0.5}_{-0.4}$
MS 1621.5+2640....	0.426	546	30.0	16:23:35.0	+26:34:26	197	$6.4^{+0.6}_{-0.5}$	$6.4^{+0.8}_{-0.7}$	$6.3^{+0.8}_{-0.7}$
MACS J0417.5-1154.	0.440	3270	11.9	04:17:33.5	−11:53:58	270	9.4±0.7	$11.4^{+1.9}_{-1.6}$	$10.6^{+2.3}_{-1.3}$
RXC J1206.2-0848..	0.440	3277	23.4	12:06:12.2	−08:48:05	236	11.4±0.9	$12.5^{+1.7}_{-1.5}$	$12.7^{+2.1}_{-1.8}$
ClG J0329-0212.....	0.450	6108	39.5	03:29:41.6	−02:11:46	127	5.9±0.2	$6.8^{+1.1}_{-0.6}$	$7.2^{+1.0}_{-0.8}$
RX J1347.5-1145....	0.451	3592	57.7	13:47:30.7	−11:45:11	167	$13.4^{+0.5}_{-0.3}$	$13.6^{+1.7}_{-0.9}$	$12.8^{+1.3}_{-1.1}$
ClG J1701+6414....	0.453	547	48.2	17:01:24.0	+64:14:11	108	4.7±0.3	$5.3^{+0.9}_{-0.5}$	$5.1^{+0.8}_{-0.6}$
3C 295.....	0.461	2254	79.8	14:11:20.2	+52:12:08	128	5.7±0.2	$5.4^{+0.6}_{-0.5}$	$5.1^{+0.7}_{-0.5}$
ClG J1621+3810....	0.461	6172	29.8	16:21:25.0	+38:10:07	118	$6.8^{+0.6}_{-0.4}$	$7.4^{+1.4}_{-1.3}$	$8.2^{+2.4}_{-1.7}$
ClG J1524+0957....	0.516	1664	50.1	15:24:39.8	+09:57:46	112	4.8±0.4	$4.6^{+0.6}_{-0.5}$	$4.9^{+0.7}_{-0.6}$
MS 0451.6-0305.....	0.539	902	32.3	04:54:11.9	−03:00:56	147	9.7±0.8	$8.5^{+1.1}_{-0.8}$	$8.3^{+1.4}_{-1.0}$
MS 0015.9+1609....	0.541	520	67.4	00:18:33.7	+16:26:17	197	9.7±0.5	$9.9^{+0.7}_{-0.6}$	$10.1^{+0.9}_{-0.8}$
ClG J1149+2223....	0.544	3589	20.0	11:49:35.7	+22:24:04	177	9.8±0.8	$9.1^{+1.0}_{-0.9}$	$9.0^{+1.2}_{-0.9}$

Table 4.1, cont.

Cluster	z	ObsID	t_{exp}[a] (ks)	RA[b]	DEC[b]	T_X aperture (arcsec)	T_X (keV)	T_{XCS}, SS ev.[c] (keV)	T_{XCS}, no ev.[d] (keV)
ClG J1423+2404....	0.545	4195	103.6	14:23:47.8	+24:04:41	156	$5.4^{+0.2}_{-0.1}$	5.0±0.3	4.6±0.3
ClG J1354-0221.....	0.546	5835	37.5	13:54:17.2	−02:21:50	94	$4.1^{+0.8}_{-0.3}$	$4.0^{+1.1}_{-0.9}$	$3.9^{+1.2}_{-1.0}$
ClG J0717+3745....	0.548	4200	59.1	07:17:31.3	+37:45:35	244	$11.5^{+0.7}_{-0.8}$	$10.3^{+0.8}_{-0.6}$	9.9±0.6
ClG J1120+2326....	0.562	1660	69.3	11:20:57.5	+23:26:34	128	$4.2^{+0.6}_{-0.3}$	4.7±0.7	3.9±0.4
ClG J2129-0741.....	0.570	3595	19.9	21:29:26.2	−07:41:28	166	$11.8^{+2.8}_{-2.4}$	$9.0^{+2.7}_{-1.2}$	$8.9^{+3.5}_{-1.5}$
MS 2053.7-0449.....	0.583	1667	44.5	20:56:21.3	−04:37:49	69	$4.0^{+0.5}_{-0.2}$	$3.6^{+0.8}_{-0.5}$	$3.2^{+0.8}_{-0.5}$
ClG J0647+7015....	0.584	3584	19.9	06:47:50.6	+70:14:54	160	$15.0^{+3.8}_{-2.7}$	...	...
ClG J0542-4100.....	0.634	914	48.6	05:42:49.6	−40:59:58	118	$6.4^{+0.8}_{-0.7}$	$5.4^{+1.0}_{-0.6}$	$6.2^{+1.2}_{-1.0}$
ClG J1419+5326....	0.640	3240	9.1	14:19:12.2	+53:26:09	59	$4.1^{+0.8}_{-0.6}$	$3.4^{+0.8}_{-0.7}$	$3.1^{+1.6}_{-0.8}$
ClG J0744+3927....	0.686	6111	49.5	07:44:52.8	+39:27:27	118	9.6±0.9	$11.7^{+2.2}_{-2.0}$	$10.4^{+3.2}_{-2.1}$
ClG J1221+4918....	0.700	1662	78.3	12:21:25.9	+49:18:28	138	$6.5^{+0.8}_{-0.6}$	$6.4^{+1.0}_{-0.7}$	$6.1^{+0.9}_{-0.8}$
ClG J1113-2615.....	0.730	915	62.5	11:13:05.0	−26:15:40	79	$3.7^{+0.6}_{-0.5}$	$2.8^{+0.6}_{-0.4}$	$2.6^{+0.6}_{-0.4}$
ClG 1137+6625.....	0.782	536	27.6	11:40:22.4	+66:08:16	98	$5.9^{+1.2}_{-0.9}$	$6.1^{+2.5}_{-1.7}$	$6.4^{+4.4}_{-2.2}$
RX J1350.0+6007...	0.804	2229	58.3	13:50:48.3	+60:07:11	98	$4.1^{+0.8}_{-0.6}$	$4.3^{+1.6}_{-0.8}$	$4.5^{+2.1}_{-1.2}$
RX J1317+2911.....	0.805	2228	111.3	13:17:21.8	+29:11:19	69	$3.8^{+1.7}_{-0.9}$	$3.3^{+3.1}_{-1.1}$	$2.2^{+3.0}_{-0.5}$
RX J1716+6708.....	0.813	548	51.2	17:16:49.1	+67:08:24	108	$6.4^{+0.9}_{-0.8}$	$5.6^{+1.2}_{-0.8}$	$6.4^{+2.3}_{-1.4}$
ClG J1056-0337.....	0.826	512	66.7	10:56:59.5	−03:37:34	118	$9.2^{+1.5}_{-1.2}$	$8.7^{+1.8}_{-1.1}$	$8.6^{+2.3}_{-1.5}$
ClG J1226+3332....	0.890	3180	31.6	12:26:58.0	+33:32:46	108	$12.2^{+1.8}_{-1.7}$	$13.6^{+4.0}_{-3.2}$	$10.3^{+5.1}_{-3.1}$
ClG J1415+3611....	1.030	4163	89.2	14:15:11.2	+36:12:03	79	$6.8^{+1.0}_{-0.7}$	$6.2^{+1.8}_{-1.1}$	$6.0^{+1.5}_{-1.6}$
ClG J1252-2927.....	1.235	4198	162.5	12:52:54.4	−29:27:16	69	$5.7^{+1.4}_{-1.0}$	$5.3^{+1.6}_{-1.0}$	$5.2^{+2.4}_{-1.3}$

[a]Exposure time after light curve filtering.

[b]Coordinates given are center of spectral extraction aperture.

[c]Core-subtracted temperature measured assuming self-similar evolution of r_Δ.

[d]Core-subtracted temperature measured assuming no evolution of r_Δ.

4.3.2 X-ray Data Reduction

The data reduction is carried out using the standard *Chandra* analysis software CIAO, version 3.3, with CALDB version 3.2.1, and the spectral fitting package XSPEC, version 11.3.1. We generate new level 2 events files from the level 1 files obtained from the *Chandra* archive, so that all observations are reduced in a uniform manner. The following reduction procedure is applied to each cluster.

Light curves are extracted for back-illuminated chips 5 and 7 individually, and for front-illuminated chips 0–3 and 6 combined. Light curves are extracted and binned in time using the recommended criteria for each chip.[1] Flares are excluded using the CIAO task "LC_CLEAN" based on the median value of the light curve. The exposure times after filtering are given in Table 4.1.

Cosmic ray events are identified with the CIAO tool "ACIS_RUN_HOTPIX". A new level 1 events file is then generated using the latest gain file, and charge transfer inefficiency (CTI) and time-dependent gain variation corrections are applied as appropriate. Standard bad columns and hot pixels are excluded. Events with ASCA grades of 0, 2, 3, 4, and 6 are used. A level 2 events file is then created from the filtered level 1 events file. Where the observation was made in very faint (VF) mode, we carry out the extra background event flagging that this enables.

We attempt to use background data from the actual data sets, extracting the background from regions well away from target cluster or other emission. For some clusters, however, emission fills most of the detector, and in these cases we extract the background spectrum from the Markevitch blank-sky data.[2] To account for small differences in the particle background between these statistical backgrounds and each individual observation, the blank-sky sets' exposure times are scaled by the ratio of counts in the 7–12 keV energy band in the data and blank-sky observations. Before using either background method point sources are identified by the iterative method described in Sanderson et al. (2005) and checked by visual inspection, and then excluded. Even when emission-free regions are available, if the spectral fit is worse with the local background than with the blank-sky background, we use the latter. In total, we use the blank-sky backgrounds for 41 of the 70 clusters in our sample.

4.3.3 Spectral Fitting

Cluster spectra are extracted in regions with maximum radius chosen by eye to be where the cluster emission merges into the background; the center coordinates and radii of our extraction regions are given in Table 4.1. Choosing apertures based on the X-ray surface brightness distribution might result in smaller apertures

[1] http://cxc.harvard.edu/ciao/
[2] http://cxc.harvard.edu/contrib/maxim/acisbg/

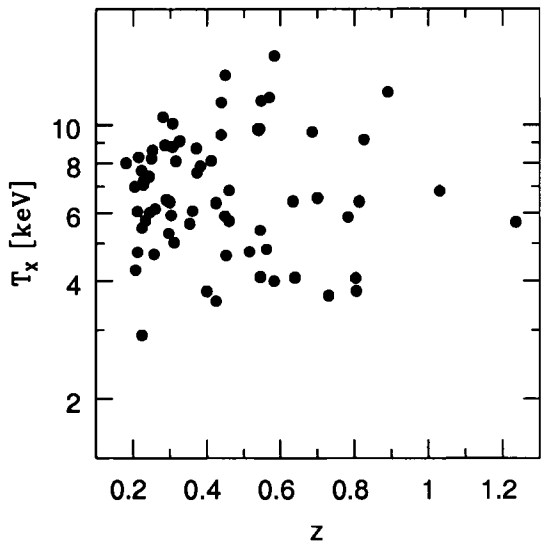

Figure 4.1 — Measured emission-weighted mean temperature T_X plotted versus redshift for the clusters in our sample.

relative to the physical size of clusters that are cooler or lie at higher redshifts, and thus will tend to have observations with fewer total counts. However, Figure 4.2, which plots the ratio of the spectral extraction radius to r_{500} for each cluster versus cluster mean temperature (*left*) and redshift (*right*), suggests that this is not the case. The mean ratio of aperture radius to r_{500} is 0.84 ± 0.20 (RMS), with no apparent temperature or redshift dependence.

We generate weighted response matrix files (RMFs) using the CIAO tool MKACISRMF when the data allow; otherwise we use the older tool MKRMF.

We fit to the cluster spectra a single-temperature APEC model with a component for galactic absorption. We use fit N_H values when they are reasonable (i.e., within a few standard deviations of the galactic value), and not pegged to zero; otherwise, we fix N_H to the galactic value (Dickey & Lockman 1990). In total, we fit N_H for 18 of the 70 clusters. We generally extract spectra in energy bands of 0.7–9 keV for ACIS-I, and 0.5–9 keV for ACIS-S. In a few cases we use an upper limit of 7 keV when there is clearly spurious, non-background emission above this value; in no case does this change the measured temperature at greater than the 1–2% level. We use Cash statistics (Cash 1979), which are preferable to χ^2 statistics when the S/N is low. In our sample the use of Cash statistics generally results in a best-fit temperature that is a few percent higher than that measured with χ^2 statistics.

We measure the core subtracted temperature T_{XCS} by extracting spectra with the same maximum radius as described above, but excluding the inner $0.2r_{500}$; the core subtracted temperature and the $0.2r_{500}$ exclusion radius are measured iteratively until convergence. (Our definition of r_{500} is given in §4.3.5.) For two clusters,

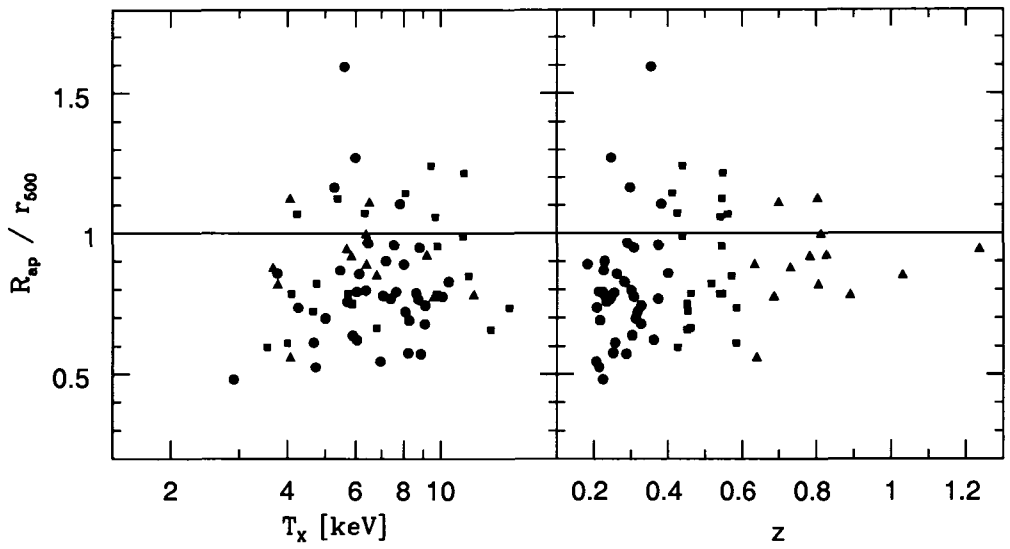

Figure 4.2 — The ratio of our spectral extraction radius to r_{500} (defined as described in §4.3.5) for each cluster, plotted versus the measured non-core subtracted temperature (*left*) and versus redshift (*right*). Markers correspond to $z < 0.4$ (circles), $0.4 < z < 0.6$ (squares), and $z > 0.6$ (triangles).

ZwCl 1356+6245 and CLG J0647+7015, the iteration does not converge to a reasonable value when the core is excluded, and so we do not measure core subtracted quantities for these two.

Our measured values for the temperature of the entire cluster, and for $T_{\rm XCS}$ measured assuming self-similar evolution and assuming no evolution, are given in Table 4.1.

4.3.4 Comparison with Published Temperatures

Though calibrations continue to improve, measurements of the same cluster by different instruments, and by different methods with the same instruments, lead to temperature measurements that differ. To check the accuracy of our own temperature measurements, we compare our values to those obtained in two other recent *Chandra* studies.

Balestra et al. (2007) (hereafter Ba07) studied 56 clusters over a redshift and temperature range similar to our own; our samples have 38 clusters in common. Our data reduction and spectral fitting processes differ from theirs in several small ways: Ba07 use local backgrounds exclusively, while we, as described above, use blank-sky backgrounds when local backgrounds are not possible or give worse spectral fits; they always fix the value of $N_{\rm H}$ to galactic, while we allow it to float when the value obtained thereby is reasonable; they use a spectral extraction band of 0.6–8 keV, versus our 0.5– or 0.7–9 keV; and they include a spectral component to compensate for Ir-M edge residuals, a correction that has been taken into account in the more recent calibration files which we use. Because clusters are not isothermal, the emission-weighted mean temperature

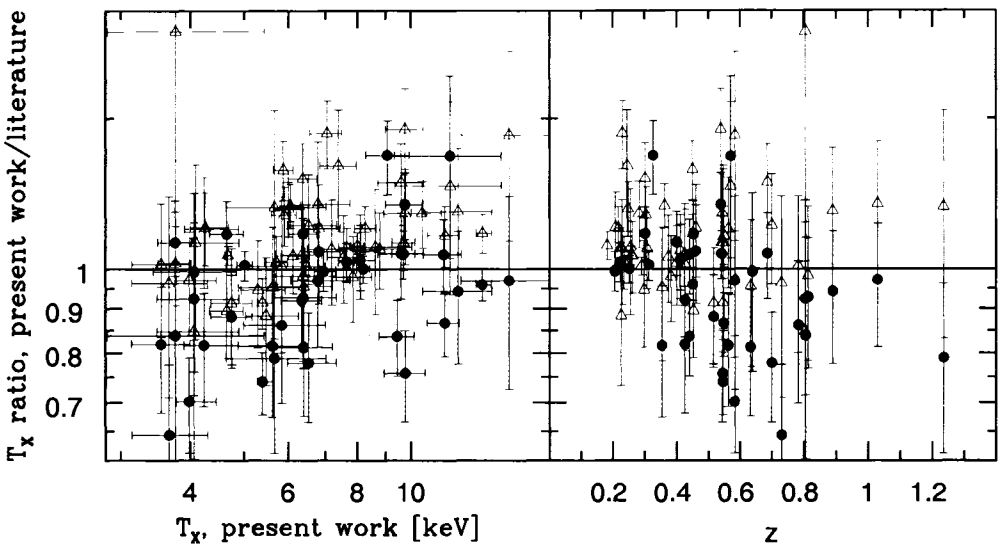

Figure 4.3 — The ratio of our measured cluster temperatures to published temperatures (vertical axis), plotted versus our temperature (*left*) and versus redshift (*right*). Published temperatures are from Maughan et al. (2007) (triangles) and Balestra et al. (2007) (circles).

is affected by the choice of energy band. Most importantly, Ba07 use spectral extraction regions determined via a method intended to maximize the S/N, which results in the use of extraction radii up to a factor of two smaller than ours. Their resulting extraction regions have a clear redshift trend, with radii as small as $\sim$0.3 r_{500} at high redshift.

Maughan et al. (2007) (hereafter Ma07) measured temperatures for 115 clusters, of which 53 are in common with our sample. Differences between our analyses include their use of a 0.6–9.0 keV spectral fitting band; their fixing $N_{\rm H}$ to the galactic values; and their use of blank-sky backgrounds in some cases where we use local backgrounds, plus an additional soft X-ray background component. Ma07 also use a different method for determining the spectral extraction region, measuring all spectra out to a radius of r_{500} as determined from an iterative procedure using a mass–$Y_{\rm X}$ relation, where $Y_{\rm X}$ is the product of the temperature and gas mass (Kravtsov et al. 2006).

To examine the difference between our temperatures and those of these two studies, we compare the error-weighted ratio of our temperatures to theirs. Overall, our temperatures are *lower* than those of Ba07 by a weighted average of $(3 \pm 1)\%$, and *higher* than those of Ma07 by $(6 \pm 1)\%$. To examine whether we can reproduce their values, we remeasured the temperatures of five clusters using methods similar to those of Ba07 and Ma07; i.e., we used their reported aperture radii, spectral extraction bands, and spectral models. We fixed $N_{\rm H}$ in all cases for this comparison, but did not change our choice of background strategies. As can be seen in Table 4.2, these changes resulted in generally higher temperatures when using the methods closer

Table 4.2. Comparison of Temperature Measurements

Cluster	z	Our T_X (keV)	Balestra et al. (2007)		Maughan et al. (2007)	
			They (keV)	We[a](keV)	They (keV)	We[a](keV)
MS 0451.6-0305	0.54	9.8 ± 0.8	$8.2^{+0.4}_{-0.3}$	10.5 ± 0.7	$6.7^{+0.6}_{-0.5}$	8.1 ± 0.4
ClG J1149+2223	0.54	9.8 ± 0.8	$12.9^{+1.2}_{-1.0}$	$9.9^{+1.0}_{-0.8}$	$8.4^{+0.9}_{-0.7}$	$8.7^{+0.9}_{-0.6}$
ClG J1120+2326	0.56	$4.2^{+0.6}_{-0.3}$	5.2 ± 0.5	$4.4^{+0.4}_{-0.3}$	$3.8^{+0.4}_{-0.3}$	3.2 ± 0.3
ClG J1113-2615	0.73	$3.7^{+0.6}_{-0.5}$	$5.7^{+0.9}_{-0.6}$	$5.0^{+0.9}_{-0.8}$	$3.8^{+0.9}_{-0.7}$	3.1 ± 0.4
RX J1317+2911	0.81	$3.8^{+1.7}_{-0.9}$	$4.5^{+1.4}_{-1.0}$	$4.4^{+0.9}_{-1.0}$	$2.0^{+0.7}_{-0.5}$	$3.3^{+1.5}_{-0.8}$

[a]Our measurement of the cluster temperature using the same aperture and similar methods as the literature sources; see text.

to those of Ba07, and generally lower temperatures when using methods closer to those of Ma07, thus at least partially explaining the sources of systematic differences between our measurements and those of these two papers. Note that this does not mean that our temperatures necessarily came to agree more closely with theirs; for MS 0451.6-0305, for example, our initial temperature was higher than that of Ba07, and these changes resulted in an even higher temperature.

The overall hotter temperatures that we measure relative to Ma07 may be attributable to variations in ICM temperature with radius. As shown in §4.3.3, our spectral extraction radii average $(0.84 \pm 0.20)r_{500}$, while Ma07 uses uniform radii of r_{500}. The ICM temperature generally decreases with radius at these radii (e.g., Vikhlinin et al. 2005; Pratt et al. 2007), and so we would expect our measured temperatures to be systematically slightly higher than those of Ma07.

However, the differences between our temperature measurements and those of the other two studies are not uniform; there are dependences on temperature and, for Ba07, redshift. The left panel of Figure 4.3 shows the ratio of our temperatures to the literature values versus our temperature. In the case of the Ma07 comparison, the ratio is clearly greater at higher temperatures; a one-dimensional least-squares fit of a straight line shows that the ratio increases as $(0.14^{+0.12}_{-0.19}) \log T_X$ for Ba07, and as $(0.22^{+0.05}_{-0.09}) \log T_X$ for Ma07. The latter trend may again result from Ma07's choice of r_{500} as an extraction radius; extraction regions hotter clusters may include more background-dominated area, leading to temperature systematics as parts of the spectrum are deweighted by background noise.

The right panel of Figure 4.3 shows the dependence of temperature ratio on redshift. There is no evidence for a redshift dependence when comparing to Ma07; the ratio varies as $(0.02 \pm 0.09)z$. For Ba07, however, the ratio varies as $(-0.31^{+0.09}_{-0.08})z$, showing a clear negative dependence on redshift. This is almost certainly

a result of Ba07's use of extraction regions that feature a trend toward smaller fractions of the virial radius at higher redshift.

The differences between our measured temperatures and those from the literature underscore the difficulties inherent in comparing cluster parameters measured using differing instruments, instrumental calibrations, and methods. This calls into question the reliability of results obtained from directly combining data from multiple studies (e.g., Branchesi et al. 2007), and suggests that caution should be taken when comparing more processed results, such as the low-redshift slopes and normalizations often combined with new measurements of higher-redshift clusters to test for scaling relation evolution (e.g., Vikhlinin et al. 2002; Ettori et al. 2004b; Kotov & Vikhlinin 2005).

4.3.5 Imaging Analysis

We extract X-ray images and use the spectral fit to obtain the conversion factor from counts to physical units in the rest frame 0.5–2 keV band. Because the flattening of statistical backgrounds using the exposure map generated for a particular observation results in a spatially inhomogeneous background image, we fit a flat background to the regions outside of the cluster emission using the same technique used to determine the surface brightness profile, described below. The results of this fitting are checked by examining radial brightness profiles and via simple comparison of total counts in regions well outside of cluster emission.

As our observations do not in general contain enough photons to do a deprojection analysis, particularly at high redshift, we fit the standard spherical isothermal β model (Cavaliere & Fusco-Femiano 1978) to the cluster emission:

$$I(r) = I_0 \left[1 + \left(\frac{r}{R_c}\right)^2\right]^{-3\beta+1/2}, \tag{4.5}$$

with central brightness I_0, core radius R_c, and power-law index β. In what are traditionally considered "cool core" clusters, i.e., where there is a central emission excess due to the formation of a cool dense core, we fit a double β model (Ikebe et al. 1996, 1999; Mohr et al. 1999) with both components having the same center coordinates and index β, so that the total surface brightness is the sum of the two, i.e.,

$$I(r) = \sum_{i=1}^{2} I_{0,i} \left[1 + \left(\frac{r}{R_{c,i}}\right)^2\right]^{-3\beta+1/2}. \tag{4.6}$$

We fit these surface brightness profiles to the two-dimensional surface brightness images, and find the best fit and one σ confidence intervals for each parameter using Cash statistics. In a few cases cases (A521, A1682, and A2744) there are prominent clumps or subclusters separate from the main body of the cluster,

Table 4.3: β Model Parameters

Cluster	Fit aperture (arcsec)	β	I_1 (cgs[a])	$R_{c,1}$ (arcsec)	I_2 (cgs[a])	$R_{c,2}$ (arcsec)
A665.....	394	0.62±0.01	1.9±0.0 E-12	$65.6^{+1.4}_{-1.3}$	...	...
A963.....	197	0.55±0.00	6.6±0.1 E-12	$21.1^{+0.5}_{-0.4}$	...	...
RX J0439.0+0520...	148	$0.67^{+0.04}_{-0.02}$	$3.0^{+0.5}_{-0.4}$E-12	$28.0^{+3.7}_{-3.3}$	5.4±0.4 E-11	$5.4^{+0.5}_{-0.4}$
A1423.....	187	0.46±0.01	$7.2^{+0.6}_{-0.5}$E-12	10.5±0.8	...	...
ZwCl 2701.....	153	0.58±0.01	1.5±0.0 E-11	12.3±0.3	...	...
A773.....	256	0.60±0.01	2.6±0.1 E-12	$41.2^{+1.4}_{-1.5}$	...	...
A2261.....	148	$0.55^{+0.01}_{-0.00}$	1.2±0.0 E-11	$18.1^{+0.6}_{-0.5}$	...	...
ACO 2246.....	148	0.52±0.01	3.7±0.3 E-12	$9.0^{+0.8}_{-0.7}$	...	...
A1682.....	177	$0.56^{+0.06}_{-0.04}$	1.0±0.1 E-12	$49.2^{+9.7}_{-7.5}$	...	...
A2111.....	295	0.58±0.02	1.2±0.1 E-12	$48.7^{+3.1}_{-3.2}$	...	...
A267.....	276	0.62±0.01	3.3±0.1 E-12	33.3±1.2	...	...
RX J2129.7+0005...	157	0.60±0.01	7.4±0.9 E-12	$23.4^{+2.3}_{-2.0}$	$6.2^{+0.6}_{-0.3}$E-11	4.1±0.4
RX J0439.0+0715...	256	0.61±0.01	$6.0^{+0.2}_{-0.1}$E-12	$26.1^{+0.8}_{-1.1}$	...	...
A521.....	295	0.75±0.00	5.5±0.2 E-13	122.0±2.4	...	...
A1835.....	167	0.73±0.01	5.7±0.2 E-12	$44.8^{+1.2}_{-1.4}$	1.1±0.0 E-10	8.9±0.2
A68.....	246	$0.75^{+0.03}_{-0.02}$	2.3±0.1 E-12	$53.0^{+3.3}_{-3.0}$	...	...
MS 1455.0+2232....	148	0.61±0.00	6.4±0.1 E-11	8.9±0.1	...	...
MS 1006.0+1202....	216	0.70±0.02	1.7±0.1 E-12	$48.0^{+2.8}_{-2.5}$	...	...
A697.....	256	0.64±0.01	3.7±0.1 E-12	$46.6^{+1.6}_{-1.5}$	...	...
A611.....	172	0.60±0.01	8.4±0.3 E-12	18.4±0.6	...	...
ZwCl 3146.....	246	$0.68^{+0.01}_{-0.00}$	1.6±0.1 E-11	23.8±0.6	1.2±0.0 E-10	5.4±0.1
A781.....	226	$1.47^{+0.36}_{-0.24}$	6.9±0.3 E-13	$157.2^{+28.0}_{-21.2}$	...	...
MS 1008.1-1224.....	197	0.65±0.02	2.4±0.1 E-12	35.0±1.8	...	...
RXC J2245.0+2637.	148	0.66±0.02	8.5±0.8 E-12	$21.3^{+2.2}_{-1.6}$	$4.1^{+0.6}_{-0.5}$E-11	$4.1^{+0.6}_{-0.5}$
A1300.....	207	0.49±0.01	$4.9^{+0.3}_{-0.2}$E-12	$22.1^{+1.2}_{-1.3}$	...	...
A2744.....	406	1.10±0.04	1.8±0.0 E-12	$112.5^{+4.3}_{-3.8}$	...	...
MS 2137.3-2353.....	138	0.64±0.01	$3.9^{+1.2}_{-0.9}$E-11	10.2±1.1	1.1±0.0 E-10	$3.3^{+0.5}_{-0.6}$
A1995.....	216	0.82±0.03	3.5±0.1 E-12	$43.5^{+2.2}_{-2.1}$	...	...
ZwCl 1358+6245....	157	$0.66^{+0.03}_{-0.01}$	2.8±0.2 E-12	$31.4^{+2.4}_{-1.8}$	$4.0^{+0.2}_{-0.4}$E-11	$3.8^{+0.4}_{-0.2}$
A1722.....	148	$0.64^{+0.05}_{-0.03}$	$2.1^{+0.4}_{-0.6}$E-12	$30.7^{+7.9}_{-3.9}$	$2.9^{+1.2}_{-0.8}$E-12	$7.2^{+4.4}_{-2.5}$
RXC J0404.6+1109.	128	$0.46^{+0.04}_{-0.03}$	1.0±0.1 E-12	$28.6^{+5.9}_{-4.9}$	...	...
RX J1532.9+3021...	118	0.61±0.01	1.1±0.0 E-10	$7.8^{+0.2}_{-0.3}$	...	...
A370.....	187	0.81±0.02	1.7±0.0 E-12	$59.4^{+2.1}_{-2.0}$	...	...
ZwCl 1953.....	246	0.65±0.01	4.5±0.2 E-12	$30.9^{+1.3}_{-1.4}$	...	...
RXC J0949.8+1707.	153	0.63±0.02	6.0±0.3 E-12	$27.8^{+1.9}_{-1.8}$	...	...
ClG J1416+4446....	148	$0.58^{+0.03}_{-0.02}$	$3.0^{+0.5}_{-0.7}$E-12	$16.6^{+3.3}_{-2.4}$	$2.3^{+0.9}_{-0.6}$E-11	$1.9^{+0.8}_{-0.5}$

Table 4.3, cont.

Cluster	Fit aperture (arcsec)	β	I_1 (cgs[a])	$R_{c,1}$ (arcsec)	I_2 (cgs[a])	$R_{c,2}$ (arcsec)
RXC J2228.6+2036 .	172	0.64±0.02	5.3±0.2 E-12	$31.0^{+1.8}_{-1.7}$	...	...
MS 0302.7+1658	98	0.54±0.02	$1.5^{+0.3}_{-0.2}$E-11	$6.9^{+1.2}_{-1.0}$	...	...
MS 1621.5+2640	197	0.67±0.03	1.3±0.1 E-12	$41.6^{+3.6}_{-2.9}$	...	...
MACS J0417.5-1154.	192	0.65±0.02	4.4±0.3 E-12	$48.4^{+2.8}_{-3.3}$	1.1±0.1 E-10	5.2±0.3
RXC J1206.2-0848 ..	197	0.60±0.01	1.7±0.1 E-11	$19.1^{+0.7}_{-0.6}$	...	...
ClG J0329-0212	118	0.52±0.00	1.2±0.1 E-10	$3.8^{+0.1}_{-0.2}$	...	...
RX J1347.5-1145	189	0.65±0.00	4.5±0.2 E-11	$16.7^{+0.4}_{-0.5}$	3.9±0.1 E-10	3.7±0.1
ClG J1701+6414	148	0.58±0.02	$1.1^{+0.2}_{-0.1}$E-12	$29.4^{+3.1}_{-3.4}$	$2.9^{+0.5}_{-0.3}$E-11	2.7±0.3
3C 295	118	0.63±0.01	$9.3^{+1.7}_{-1.4}$E-12	$13.1^{+1.4}_{-1.3}$	1.3±0.1 E-10	$2.7^{+0.2}_{-0.1}$
ClG J1621+3810	108	0.60±0.02	$7.6^{+2.0}_{-1.6}$E-12	$14.8^{+2.5}_{-2.0}$	$9.2^{+1.2}_{-1.0}$E-11	$2.5^{+0.4}_{-0.3}$
ClG J1524+0957	128	$0.95^{+0.14}_{-0.10}$	1.1±0.1 E-12	$56.2^{+8.2}_{-6.6}$	...	...
MS 0451.6-0305	459	0.85±0.02	9.2±0.2 E-12	37.9±1.1	...	...
MS 0015.9+1609	216	0.70±0.01	6.5±0.2 E-12	$37.5^{+1.1}_{-1.0}$	...	...
ClG J1149+2223	295	0.65±0.02	4.3±0.2 E-12	$40.9^{+2.5}_{-2.2}$	...	...
ClG J1423+2404	98	0.65±0.01	4.2±0.4 E-12	$22.0^{+1.4}_{-1.0}$	2.3±0.0 E-10	3.7±0.1
ClG J1354-0221	157	$0.76^{+0.12}_{-0.08}$	$8.3^{+1.0}_{-0.8}$E-13	$39.8^{+8.3}_{-6.6}$	...	...
ClG J0717+3745	187	0.82±0.02	4.7±0.1 E-12	$65.6^{+2.5}_{-2.2}$	...	...
ClG J1120+2326	148	$1.74^{+0.54}_{-0.31}$	$9.9^{+0.5}_{-0.4}$E-13	$88.4^{+18.5}_{-12.6}$	...	...
ClG J2129-0741	166	$0.62^{+0.02}_{-0.01}$	1.1±0.1 E-11	18.6±1.2	...	...
MS 2053.7-0449	89	$0.63^{+0.05}_{-0.04}$	$3.9^{+0.5}_{-0.4}$E-12	$15.6^{+2.5}_{-2.1}$	...	...
ClG J0647+7015	148	0.63±0.02	1.3±0.1 E-11	$18.4^{+1.3}_{-1.2}$	...	...
ClG J0542-4100	112	0.58±0.03	2.9±0.2 E-12	$22.5^{+2.7}_{-2.4}$	...	...
ClG J1419+5326	118	0.60±0.03	$1.9^{+0.4}_{-0.3}$E-11	$7.3^{+1.2}_{-1.1}$	...	...
ClG J0744+3927	148	0.56±0.01	4.4±0.2 E-11	8.5±0.4	...	...
ClG J1221+4918	157	$0.73^{+0.04}_{-0.03}$	2.5±0.1 E-12	$35.7^{+2.8}_{-2.6}$	...	...
ClG J1113-2615	98	$0.73^{+0.08}_{-0.06}$	4.3±0.5 E-12	$15.8^{+2.8}_{-2.5}$	...	...
ClG 1137+6625	98	$0.65^{+0.04}_{-0.03}$	$1.5^{+0.2}_{-0.1}$E-11	$12.4^{+1.4}_{-1.3}$	...	...
RX J1350.0+6007 ...	148	$0.61^{+0.05}_{-0.04}$	2.3±0.3 E-12	$21.4^{+3.9}_{-3.1}$	...	...
RX J1317+2911	89	$0.84^{+0.40}_{-0.20}$	$5.3^{+1.9}_{-1.2}$E-13	$29.4^{+13.8}_{-9.8}$	$4.8^{+2.1}_{-1.2}$E-12	$4.3^{+2.4}_{-1.6}$
RX J1716+6708	148	$0.68^{+0.04}_{-0.03}$	8.3±0.6 E-12	$17.3^{+1.9}_{-1.7}$	...	...
ClG J1056-0337	197	0.67±0.00	5.8±0.3 E-12	31.9±0.9	...	...
ClG J1226+3332	128	0.68±0.02	3.3±0.2 E-11	14.5±1.0	...	...
ClG J1415+3611	98	$0.75^{+0.06}_{-0.04}$	9.5±1.2 E-12	18.1±2.4	$6.5^{+2.0}_{-1.4}$E-11	$2.5^{+0.6}_{-0.5}$
ClG J1252-2927	89	0.54±0.03	1.1±0.2 E-11	$8.8^{+1.6}_{-1.4}$	...	...

[a]Units of I_1 and I_2 are erg s^{-1} cm^{-2} $arcmin^{-2}$.

which are masked out before fitting. In two cases we fix the value for β: A521, a multiply-merging cluster (Ferrari et al. 2003), for which we find a somewhat stable value of $\beta = 0.75$, which we adopt over the values of $\beta > 3$ which are found by a full gridding analysis; and ClG J1056-0337, a merging system (Jee et al. 2005) for which we find only very high values of β, leading us to adopt the canonical $\beta = 0.67$. In both cases we then measure 2 σ uncertainties in the other fit parameters. The β model parameter fit results are listed in Table 4.3. The second, bright central component is, where used for a given cluster, listed as the second brightness and core radius components I_2 and $R_{c,2}$.

We measure several different cluster observables, each of which—X-ray luminosity, ICM mass, isophotal size, and mean ICM temperature—derives from the underlying cluster structure in a different way; by studying the evolution of multiple observables, we are examining the evolution of the ICM in multiple ways. Luminosity and ICM mass are measured within two different virial radii r_Δ, which permits us to examine evolution on different scales within a cluster. We determine r_{500} and r_{2500} from the cluster temperature using M_δ–T_X relations determined by Arnaud et al. (2005) using *XMM-Newton* observations of local galaxy clusters. We use their relations for clusters with $T_X > 3.5$ keV:

$$r_{500} = 1.129 \left(\frac{T_X}{5 \text{ keV}} \right)^{0.497} E(z)^{-1} \text{ Mpc}, \tag{4.7}$$

$$r_{2500} = 0.501 \left(\frac{T_X}{5 \text{ keV}} \right)^{0.503} E(z)^{-1} \text{ Mpc}. \tag{4.8}$$

Note that by using virial radii obtained in this manner, we are implicitly testing the evolution of these local mass–temperature relations along with our other observables. That is, our "self-similar evolution" scenario includes evolution of the r_Δ–T_X relations as written above, and the "no evolution" scenario includes no evolution (i.e., no $E(z)$ factor) in the r_Δ–T_X relations.

We measure the projected X-ray luminosity L_X in the rest frame 0.5–2 keV band from the images described above, within radii of r_{500} and r_{2500}; we also measure core subtracted luminosities L_{XCS} by excising the projected luminosity from the central $0.2r_{500}$. Luminosity measurements are centered on the cluster brightness peak, with the exception of A521, where we use the peak brightness of the main cluster, not the brighter infalling subcluster to the north of the cluster center (see, e.g., Ferrari et al. 2006); and ClG J1056-0337, where we use the western brightness peak, which has been identified as the "central" mass peak via weak lensing (e.g., Jee et al. 2005). Given the small field of view of Chandra, the virial radii r_Δ often extend beyond the image boundary; furthermore, some observations are not deep enough that there is signal measurable out to a given r_Δ. We thus establish for each cluster a maximum radius from the brightness peak at which either the detector edge is reached or the S/N falls close to unity; in a few cases the maximum

radius is determined by the presence of other structure, as in the cases of ACO 2246 and ClG J1701+6414, which lie a small angular distance from one another in the same observation. Then, if the radius r_Δ exceeds this established maximum radius for a given luminosity measurement, we do not carry out that measurement on that particular cluster; this is reflected in Tables 4.4 and 4.6, where luminosity measurements are not given in many cases. We include in the luminosity uncertainties contributions from the temperature used in calculating r_Δ, as well as a uniform 10% background uncertainty.

The X-ray luminosity within a given radius can be modeled analytically by an integral of the ICM density profile and X-ray emissivity out to that radius. We can therefore use a measurement of the actual luminosity together with the measured β model parameters and the cluster temperature to find the central ICM density, and hence ICM mass via an integral of the density function to a given radius of interest; for details see Mohr et al. (1999). We estimate uncertainties on $M_{\rm ICM}$ by including the statistical uncertainties on the β model fit; a uniform 10% background uncertainty in the luminosity measurement; and temperature uncertainties in r_Δ. The ICM mass measurement is not subject to the same maximum radius restriction as luminosity, as the luminosity within any given radius can be used to measure the central density; while larger luminosity measurement radii are of course preferable, it is not necessary to measure the flux out to a given r_Δ for an ICM mass measurement within that radius. Note that we do not similarly use the β model to extrapolate luminosity measurements out to a radius of interest; this is because we prefer to directly use projected luminosities without assumptions as to the structure of the cluster, but ICM mass cannot similarly be measured without such assumptions.

We measure the isophotal size R_I of a cluster by measuring the area A_I enclosed by an isophote I, and finding the effective radius given by $A_I = \pi R_I^2$. For these measurements we use images that have been adaptively smoothed using the CIAO task `csmooth`. We include the 10% background uncertainty in the R_I uncertainties by remeasuring at isophotes increased and decreased by the background uncertainty. In the 0.5–2 keV band we are using here, the conversion from X-ray counts to physical units varies slowly with cluster temperature, so we do not include temperature uncertainties in the isophotal size. We measure R_I at three different isophotes, 1.5×10^{-13}, 6×10^{-14}, and 3×10^{-14} erg s^{-1} cm^{-2} arcmin^{-2} (in the rest frame 0.5–2 keV imaging band), which, like using both r_{500} and r_{2500} for the luminosity and ICM mass, lets us study evolution of R_I on different scales within a cluster. Clusters can "fall off" an isophotal size–temperature scaling relation when the isophote used approaches the peak surface brightness of the cluster; we therefore exclude clusters when their measured isophotal size is less than $0.2r_{500}$, our adopted core exclusion region.

4.3.6 Fitting Procedures

For a given relation involving an observable $\mathcal{O}$, we fit the form

$$\mathcal{O} = A\left(\frac{T_{\rm X}}{6\ {\rm keV}}\right)^{\alpha}(1+z)^{\gamma}, \tag{4.9}$$

or, in log space,

$$\log\mathcal{O} = \log A + \alpha\log\left(\frac{T_{\rm X}}{6\ {\rm keV}}\right) + \gamma\log(1+z). \tag{4.10}$$

That is, we fit a power-law temperature dependence α, power-law redshift dependence γ, and A, the normalization at zero redshift and temperature 6 keV.

In this paper we use unweighted orthogonal fits, meaning that we minimize the sum of the square of the point-line orthogonal distances, i.e., the sum

$$\sum_i \left\{\frac{\log\mathcal{O}_i - [\log A + \alpha\log(T_{{\rm X},i}/6) + \gamma\log(1+z_i)]}{(1+\alpha^2)^{1/2}}\right\}^2. \tag{4.11}$$

Note that the form for redshift evolution assumed here is evolution of the normalization only, and so there is no factor of γ in the denominator. We determine 1 σ uncertainties via bootstrap sampling; the best-fit value given in this paper is the mode of a histogram constructed from the bootstrapping results, and the 1 σ confidence interval is constructed in the usual manner so as to contain 68.3% of the counts around this mode. We also give here the RMS scatter in the vertical dimension (e.g., in $L_{\rm X}$ in the $L_{\rm X}$–$T_{\rm X}$ relation) for the best-fit parameters; this one-dimensional scatter is a more intuitively understandable quantity than the orthogonal scatter, as it reflects the scatter in an observable ($L_{\rm X}$, $M_{\rm ICM}$, R_I) at a given temperature. We refer to this as the intrinsic scatter ($\sigma_{\rm int}$), as the measurement uncertainties are generally much smaller than the total scatter in these relations (e.g., O'Hara et al. 2006).

The question of which fitting method is "best" is still open, and rests to a large extent on whether one property (such as $T_{\rm X}$) is considered more fundamental than the other (such as $L_{\rm X}$); this often seems implicit in discussions of $L_{\rm X}$–$T_{\rm X}$, $M_{\rm ICM}$–$T_{\rm X}$, and other relations, and would imply that a one-dimensional least-squares fit, with temperature as the independent variable, might be appropriate. But if both observables are considered to be linked via another property of the system (such as cluster mass), then a orthogonal minimization fit, which treats both variables equally, may be more appropriate; we agree with this view, and so adopt orthogonal fitting in this paper.

Fits of mock scaling relations using both the orthogonal fitting method and an ordinary least-squares

(OLS) fit support this decision. A difficulty that arises in such tests is that assumptions must be made regarding the scatter in mock relations; e.g., if only scatter in the y direction is generated, then an OLS fit will doubtless give better results than an orthogonal fit. For example, Lopes et al. (2006) make the claim that orthogonal regression produces more accurate measurements of scaling relation slopes than the bisector method (discussed below), based on their own tests using mock data sets; however, as these data sets were generated using orthogonal scatter, such a result is entirely expected. Because of the difficulty in defining "correct" scatter, we test scenarios in which only scatter in the y direction is used, and in which equal scatter in both the x and y directions is used. That is, we generate a random x value, use an assumed scaling relation to find y, and then shift the values using normal random deviates in the y direction only, or in both the x and y directions. Note that using equal x and y scatter is *not* the same as using orthogonal scatter, and so an orthogonal relation should not be *a priori* assumed to give the correct result in such a case. In our testing we do not assume measurement uncertainties, but fit an intrinsic scatter in the y direction in the OLS fits so that the reduced χ^2 value is equal to unity. Again, in real scaling relations the scatter is generally dominated by intrinsic scatter, so this is a reasonable approach.

The results of our tests clearly indicate that the OLS method is a less robust approach than the orthogonal method. For example, when using only y direction scatter of 0.05 (i.e., the random deviates have a standard deviation in $\log_{10}$ space of 0.05), the orthogonal method gives a result that is 2% ($\sim 1\sigma$) high while the OLS method gives the correct result; but when using equal scatter of 0.05 in x and y, the orthogonal method gives the correct slope, while the OLS method gives a result that is $\sim$10% ($\sim 2\sigma$) too low. The results get worse for OLS more rapidly than for orthogonal fitting; e.g., scatter of 0.15 in y only gives an orthogonal slope that is 16% ($\sim 2.5\sigma$) high, but scatter of 0.10 in both dimensions gives an OLS result that is 51% ($\sim 8.5\sigma$) too low. The results are very similar when true orthogonal scatter is used, rather than random, but on average equal, scatter in each dimension.

Again, the exact origin of scaling relation scatter is unknown, so it is difficult to declare a "correct" way of testing fitting methods. There is undoubtedly some measurement scatter, however, and so scaling relations certainly have at least some scatter in both dimensions. For this reason, as well as the physical arguments given above, we adopt the orthogonal fit as our chosen method for this paper.

Besides orthogonal fitting, another approach that treats the two variables equally is the bisector method, in which OLS fits are done with each of the two variables as independent and dependent (i.e., y as a function of x, and x as a function of y), and the final result bisects the two individual fits. This is not appropriate for our work, because we fit observables as a function of both temperature and redshift, and it is unclear how the bisector method can be extended into three dimensions. Orthogonal fitting is clearly defined in

any number of dimensions; i.e., it seeks the shortest point-line distance in two dimensions, the shortest point-plane distance in three dimensions, and so forth. Also, each individual OLS fit in the bisector method is subject to the great dependence on the form of scatter as discussed above, and so the bisector method's utility for studying scaling relations is likewise questionable.

4.4 Tests of the Self-Similar Evolution Scenario

We now examine the evolution of scaling relations while assuming self-similar evolution, as discussed in the introduction. That is, we assume that r_Δ scales as $E(z)^{-1}$ when measuring L_X and M_{ICM}, and when determining the core subtraction radius for T_{XCS} and L_{XCS}; and we scale measured L_X and M_{ICM} values by factors of $E(z)$ and $E(z)^{-1}$, respectively. Our values for L_X and M_{ICM}, measured using the non-core subtracted temperature, are given in Table 4.4. We then test whether scaling relations evolve in a manner consistent with self-similar evolution.

4.4.1 Scaling Relations

The L_X–T_X and M_{ICM}–T_X scaling relations are plotted in Figures 4.4 and 4.5, respectively. In these figures the observables are scaled to $z = 0$ using the best-fit scaling relations. One qualitative feature of note is that the scatter is clearly smaller in the L_{XCS}–T_X relations than in their non-core subtracted counterparts; a similar, though smaller effect is visible in the ICM mass relations. This difference in scatter arises from biases in both temperature and the other observable in each relation induced as a result of cool core-related phenomena (e.g., Fabian et al. 1994; Markevitch 1998; O'Hara et al. 2006). Another interesting feature is the shallowness of the $L_{XCS,2500}$–T_{XCS} relation compared to the non-core subtracted $L_{X,2500}$–T_X relation. Best-fit scaling relation parameters are given in Table 4.5.

Studies of scaling relation evolution commonly fix the slopes to values measured from local samples, and fit only for an evolution factor. Because we are fitting all parameters simultaneously, we need to compare our measured slopes to those of local samples. Our $L_{X,2500}$–T_X relation and $L_{X,500}$–T_X relation have slopes of $2.75^{+0.28}_{-0.26}$ and $2.35^{+0.33}_{-0.24}$, respectively, which are significantly higher than the self-similar expectation $\alpha = 2$, as has been generally observed in low-redshift samples (e.g., Markevitch 1998); note that using luminosities from a fixed energy band as done here (rest frame 0.5–2 keV) gives a somewhat lower slope than the more commonly used bolometric luminosities, as shown by, e.g., Zhang et al. (2007). For the $M_{ICM,2500}$–T_X relation we find $\alpha = 1.82 \pm 0.08$, in good agreement with $\alpha = 1.91 \pm 0.16$ found by Ettori et al. (2002) using *BeppoSAX* data and a bisector fit; for the $M_{ICM,500}$–T_X relation we find $\alpha = 1.74 \pm 0.09$, in fair agreement

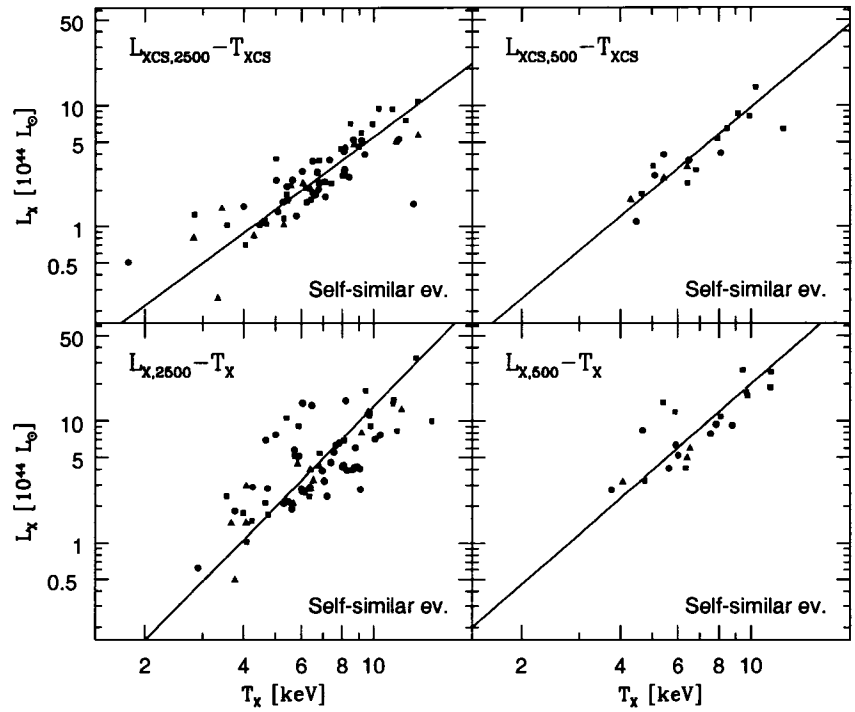

Figure 4.4 — Projected X-ray luminosity within r_{2500} (left) and r_{500}(right), with non-core subtracted (top) and core subtracted (bottom) quantities, plotted versus temperature. These quantities are measured assuming *self-similar evolution.* Luminosity values are scaled to $z = 0$ using the best-fit redshift scaling for each relation, and the best-fit slope is plotted for each relation. Markers correspond to $z < 0.4$ (circles), $0.4 < z < 0.6$ (squares), and $z > 0.6$ (triangles).

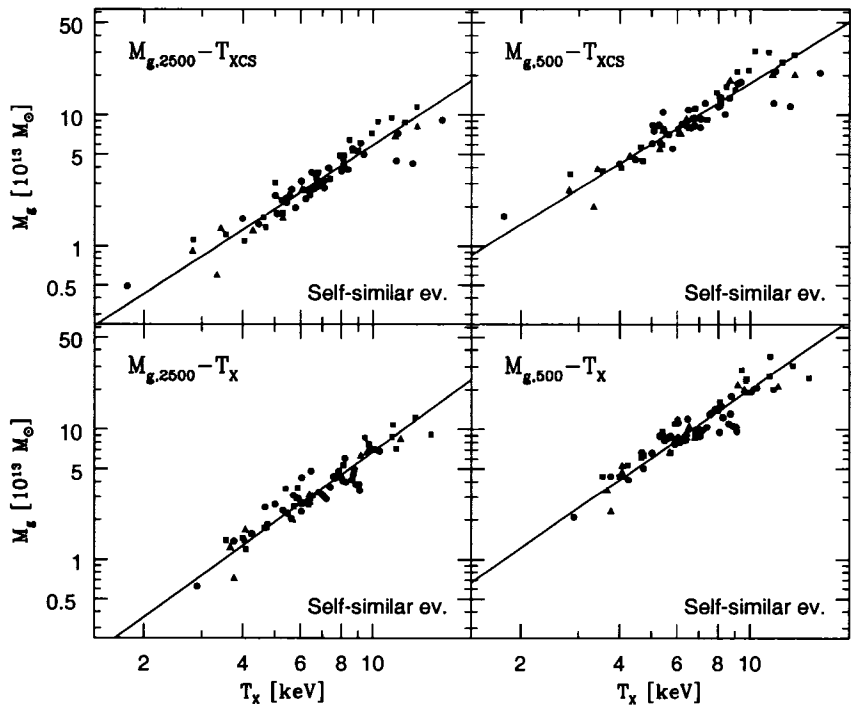

Figure 4.5 — Same as Figure 4.4, but for $M_{\rm ICM}$–$T_{\rm X}$ relations.

Table 4.4: Cluster Measurements Assuming Self-Similar Evolution

Cluster	$L_{X,2500}$ (10^{44} $L_\odot$)	$L_{X,500}$ (10^{44} $L_\odot$)	$M_{ICM,2500}$ (10^{13} $M_\odot$)	$M_{ICM,500}$ (10^{13} $M_\odot$)	$R_{1.5E-13}$ (Mpc)	R_{6E-14} (Mpc)	R_{3E-14} (Mpc)
A665	3.27±0.03	...	3.93±0.09	13.05±0.30	0.40±0.02	...	...
A963	2.95±0.03	...	2.86±0.08	9.27±0.27	0.33±0.02	...	...
RX J0439.0+0520	2.17±0.02	...	1.42±0.07	3.79±0.19	0.23±0.01	0.31±0.02	0.40±0.04
A1423	1.98±0.04	...	2.08±0.07	8.01±0.28	0.28±0.01	0.46±0.04	...
ZwCl 2701	2.10±0.01	...	1.58±0.07	4.63±0.21	0.24±0.01	0.34±0.02	...
A773	2.92±0.03	...	3.55±0.09	11.34±0.30	0.36±0.02	...	...
A2261	4.69±0.03	...	3.81±0.11	12.20±0.36	0.38±0.02	...	...
ACO 2246	0.46±0.01	...	0.56±0.04	1.91±0.15	...	0.21±0.01	...
A1682	1.61±0.09	...	2.01±0.08	7.55±0.31	0.32±0.02	0.52±0.05	...
A2111	1.77±0.05	...	2.59±0.08	9.03±0.29	0.31±0.01	0.49±0.03	0.66±0.06
A267	2.37±0.03	...	2.73±0.09	8.15±0.27	0.30±0.01	0.43±0.03	0.57±0.05
RX J2129.7+0005	4.26±0.03	...	2.75±0.11	8.13±0.33	0.34±0.02	0.49±0.04	0.63±0.07
RX J0439.0+0715	3.28±0.04	...	3.20±0.11	9.43±0.31	0.35±0.02	0.49±0.03	0.61±0.05
A521	2.00±0.07	3.43±0.07	2.38±0.10	10.80±0.44	0.43±0.03	0.68±0.08	0.82±0.11
A1835	10.50±0.05	...	5.35±0.16	13.56±0.42	0.44±0.02	...	...
A68	2.84±0.07	...	3.68±0.11	9.96±0.29	0.35±0.01	0.48±0.03	...
MS 1455.0+2232	4.95±0.01	5.45±0.04	2.20±0.12	6.05±0.33	0.30±0.02	0.41±0.04	...
MS 1006.0+1202	1.85±0.03	...	2.37±0.10	7.21±0.31	0.29±0.01	0.41±0.03	...
A697	5.32±0.09	...	5.96±0.16	18.56±0.50	0.51±0.02	0.71±0.05	0.88±0.07
A611	2.91±0.03	...	3.29±0.11	9.50±0.31	0.32±0.01	0.44±0.02	...
ZwCl 3146	9.16±0.02	...	4.19±0.19	10.77±0.48	0.41±0.03	0.56±0.05	...
A781	1.43±0.09	...	2.05±0.12	7.99±0.45	0.37±0.03	0.59±0.07	0.74±0.10
MS 1008.1-1224	1.93±0.03	...	2.44±0.11	7.44±0.35	0.33±0.02	0.45±0.03	0.56±0.05
RXC J2245.0+2637	3.47±0.02	3.85±0.05	2.54±0.13	6.82±0.35	0.30±0.02	0.41±0.03	0.51±0.04
A1300	4.04±0.09	5.55±0.11	4.28±0.15	15.90±0.56	0.46±0.02	0.69±0.05	...
A2744	4.74±0.10	...	6.10±0.19	17.12±0.52	0.58±0.03	...	...
MS 2137.3-2353	5.15±0.02	...	2.27±0.14	5.87±0.37	0.29±0.02	0.39±0.03	0.49±0.05
A1995	2.88±0.04	...	3.45±0.14	8.43±0.33	0.34±0.01	0.44±0.02	0.56±0.04
ZwCl 1358+6245	2.64±0.04	...	3.28±0.12	9.21±0.33	0.31±0.01	0.43±0.02	0.54±0.03
A1722	1.80±0.05	...	2.90±0.10	8.53±0.31	0.28±0.01	0.40±0.02	0.54±0.03
RXC J0404.6+1109	1.20±0.08	2.30±0.14	1.73±0.11	7.61±0.48	0.28±0.01	0.64±0.07	...
RX J1532.9+3021	8.84±0.03	...	3.62±0.22	9.81±0.59	0.36±0.02	0.50±0.04	0.64±0.07
A370	2.59±0.05	...	3.84±0.16	11.46±0.49	0.40±0.02	...	...
ZwCl 1953	3.43±0.06	4.31±0.09	3.68±0.18	11.27±0.56	0.39±0.02	0.56±0.04	0.71±0.07
RXC J0949.8+1707	4.08±0.07	5.11±0.09	4.05±0.20	12.40±0.61	0.41±0.02	0.57±0.04	0.76±0.07
ClG J1416+4446	1.10±0.02	1.44±0.05	1.14±0.12	3.78±0.40	0.24±0.01	0.34±0.03	0.44±0.05

Table 4.4, cont.

Cluster	$L_{X,2500}$ (10^{44} $L_\odot$)	$L_{X,500}$ (10^{44} $L_\odot$)	$M_{ICM,2500}$ (10^{13} $M_\odot$)	$M_{ICM,500}$ (10^{13} $M_\odot$)	$R_{1.5E-13}$ (Mpc)	R_{6E-14} (Mpc)	R_{3E-14} (Mpc)
RXC J2228.6+2036 .	4.15±0.08	5.66±0.08	4.43±0.23	13.92±0.71	0.50±0.03	0.69±0.06	0.82±0.08
MS 0302.7+1658	1.41±0.02	···	1.15±0.14	3.76±0.45	0.23±0.01	0.33±0.03	0.43±0.05
MS 1621.5+2640	1.41±0.05	2.09±0.09	2.15±0.14	7.60±0.51	0.32±0.02	0.48±0.04	0.70±0.08
MACS J0417.5-1154.	10.27±0.19	13.17±0.11	7.14±0.33	24.15±1.13	0.63±0.04	0.82±0.07	0.97±0.10
RXC J1206.2-0848 ..	8.02±0.10	9.47±0.11	7.24±0.28	21.76±0.84	0.54±0.03	0.73±0.05	0.92±0.07
ClG J0329-0212	5.23±0.03	5.92±0.09	2.89±0.22	9.37±0.72	0.37±0.02	0.52±0.05	0.65±0.07
RX J1347.5-1145	18.85±0.05	···	10.10±0.34	25.94±0.87	0.56±0.02	···	···
ClG J1701+6414	1.22±0.03	···	1.41±0.14	5.16±0.50	0.26±0.01	0.38±0.03	0.50±0.05
3C 295	2.91±0.01	···	2.06±0.17	5.62±0.45	0.27±0.01	0.36±0.02	0.46±0.04
ClG J1621+3810	3.09±0.03	···	2.68±0.18	7.99±0.54	0.31±0.01	0.46±0.03	0.59±0.05
ClG J1524+0957	0.92±0.04	1.47±0.08	1.47±0.16	5.28±0.57	0.29±0.02	0.43±0.04	0.52±0.06
MS 0451.6-0305	6.09±0.09	7.06±0.16	6.18±0.34	15.86±0.88	0.48±0.02	0.62±0.04	···
MS 0015.9+1609	5.76±0.08	7.61±0.11	6.14±0.34	19.43±1.08	0.55±0.03	···	···
ClG J1149+2223	4.78±0.14	7.07±0.14	5.66±0.32	20.17±1.12	0.56±0.03	0.86±0.08	1.08±0.12
ClG J1423+2404	5.54±0.02	6.23±0.10	2.75±0.28	7.91±0.80	0.34±0.02	0.49±0.05	···
ClG J1354-0221	0.53±0.03	···	0.94±0.13	3.58±0.48	0.20±0.01	0.33±0.03	0.44±0.05
ClG J0717+3745	7.78±0.23	11.13±0.13	8.51±0.41	29.57±1.41	0.68±0.04	0.88±0.07	···
ClG J1120+2326	0.78±0.05	···	1.22±0.16	4.41±0.58	0.26±0.02	0.37±0.03	0.43±0.04
ClG J2129-0741	4.22±0.17	···	5.56±0.27	16.45±0.80	0.42±0.01	0.63±0.03	0.80±0.05
MS 2053.7-0449	0.89±0.02	···	1.13±0.17	3.58±0.52	0.23±0.01	0.33±0.03	0.40±0.04
ClG J0647+7015	5.02±0.13	···	7.15±0.28	20.11±0.78	0.43±0.01	0.59±0.02	···
ClG J0542-4100	1.33±0.05	1.95±0.08	2.08±0.21	7.58±0.75	0.34±0.02	0.47±0.03	0.58±0.05
ClG J1419+5326	1.40±0.04	···	1.28±0.20	3.78±0.59	0.23±0.01	0.33±0.03	0.43±0.05
ClG J0744+3927	5.49±0.09	···	5.03±0.36	15.80±1.13	0.47±0.02	0.64±0.04	0.79±0.06
ClG J1221+4918	1.47±0.06	2.18±0.07	2.27±0.24	8.27±0.89	0.37±0.02	0.55±0.05	···
ClG J1113-2615	0.64±0.02	···	0.91±0.18	2.64±0.52	0.20±0.01	0.27±0.02	0.35±0.03
ClG 1137+6625	1.88±0.07	···	2.12±0.28	6.17±0.82	0.29±0.01	0.41±0.03	0.53±0.05
RX J1350.0+6007 ...	0.60±0.05	1.04±0.05	1.01±0.20	4.05±0.80	0.26±0.02	0.41±0.04	0.53±0.07
RX J1317+2911	0.20±0.02	···	0.52±0.11	1.77±0.38	···	0.21±0.01	0.32±0.03
RX J1716+6708	1.64±0.05	···	2.25±0.29	6.77±0.86	0.31±0.02	0.43±0.03	0.54±0.05
ClG J1056-0337	3.23±0.23	···	4.53±0.41	16.57±1.49	0.51±0.03	0.62±0.04	0.72±0.06
ClG J1226+3332	4.80±0.11	···	5.94±0.44	15.86±1.16	0.44±0.02	0.59±0.03	0.71±0.04
ClG J1415+3611	1.48±0.03	···	2.20±0.33	6.33±0.96	0.29±0.01	0.40±0.02	0.50±0.04
ClG J1252-2927	0.63±0.04	···	1.28±0.28	4.63±1.01	0.28±0.01	0.42±0.03	0.54±0.05

Table 4.5. Fit Parameters Assuming Self-Similar Evolution

Core Subtracted Relations					
Relation	α	A^{a}	γ	Diff. from 0 (%)[b]	$\sigma_{\rm int}$[c]
$L_{\rm XCS,2500}$–$T_{\rm XCS}$	$2.00^{+0.23}_{-0.19}$	$2.00^{+0.35}_{-0.30}$E44	$-0.86^{+0.38}_{-0.36}$	95–	0.28 ± 0.05
$L_{\rm XCS,500}$–$T_{\rm XCS}$	$2.26^{+0.29}_{-0.33}$	$3.02^{+1.35}_{-1.24}$E44	$-1.28^{+1.28}_{-0.86}$	69–	$0.21^{+0.08}_{-0.07}$
$M_{\rm ICM,2500}$–$T_{\rm XCS}$	$1.63^{+0.09}_{-0.08}$	$2.57^{+0.18}_{-0.17}$E13	$-0.35^{+0.20}_{-0.15}$	90–	$0.00^{+0.05}_{-0.00}$
$M_{\rm ICM,500}$–$T_{\rm XCS}$	1.56 ± 0.10	$7.94^{+0.06}_{-0.05}$E13	$-0.24^{+0.20}_{-0.18}$	74–	0.09 ± 0.04
Non-Core Subtracted Relations					
Relation	α	A^{a}	γ	Diff. from 0 (%)[b]	$\sigma_{\rm int}$[c]
$L_{\rm X,2500}$–$T_{\rm X}$	$2.75^{+0.29}_{-0.26}$	$3.24^{+0.75}_{-0.61}$E44	$-1.50^{+0.42}_{-0.49}$	99.4–	$0.60^{+0.08}_{-0.09}$
$L_{\rm X,500}$–$T_{\rm X}$	$2.35^{+0.33}_{-0.24}$	$6.03^{+3.75}_{-2.22}$E44	$-1.90^{+1.17}_{-1.11}$	90–	$0.39^{+0.12}_{-0.10}$
$M_{\rm ICM,2500}$–$T_{\rm X}$	1.82 ± 0.08	$2.69^{+0.19}_{-0.18}$E13	$-0.55^{+0.17}_{-0.15}$	99.4–	0.14 ± 0.02
$M_{\rm ICM,500}$–$T_{\rm X}$	1.74 ± 0.09	$8.32^{+0.59}_{-0.56}$E13	$-0.45^{+0.18}_{-0.16}$	98–	0.13 ± 0.02

[a]In units of $L_\odot$ for $L_{\rm X}$–$T_{\rm X}$ relations, $M_\odot$ for $M_{\rm ICM}$–$T_{\rm X}$ relations.

[b]Significance level at which γ differs from zero, as determined by bootstrap sampling and refitting; the sign indicates whether γ is positive (+) or negative (−).

[c]Intrinsic scatter in $L_{\rm X}$ or $M_{\rm ICM}$ at fixed temperature, expressed in base e.

with $\alpha = 1.98 \pm 0.11$ measured by Mohr et al. (1999) using *ROSAT* PSPC images and a mixture of *Einstein*, *Ginga*, and *ASCA* temperatures, with an unweighted orthogonal fit. Both of these are significantly higher than the self-similar expectation $\alpha = 1.5$.

In all cases, the scaling relations with core subtracted quantities have shallower slopes than the standard relations. Remarkably, the core subtracted relations have slopes consistent with the self-similar expectation to within 1σ, the sole exception being $M_{\rm ICM,2500}$–$T_{\rm XCS}$, which is consistent to within 2σ.

4.4.2 Evolution with Redshift

Figure 4.6 shows the ratio of observables ($L_{\rm X}$ and $M_{\rm ICM}$) to the $z = 0$ expectation, plotted versus redshift. That is, the vertical axis is the ratio of the observed value to the $z = 0$ self-similar prediction from the appropriate fit in Table 4.5 and the cluster temperature, i.e., $\mathcal{O}_i/\mathcal{O}_{\rm fit}(T_{{\rm X},i}, z = 0)$. Plotting in this way shows deviations from the self-similar redshift evolution prediction as a redshift dependence of the ratio $\mathcal{O}_i/\mathcal{O}_{\rm fit} = 0$; we also plot the best-fit value of γ for each relation, showing how the normalization of each scaling relation in fact evolves.

For each scaling relation, Table 4.5 includes the percent significance by which each relation differs from

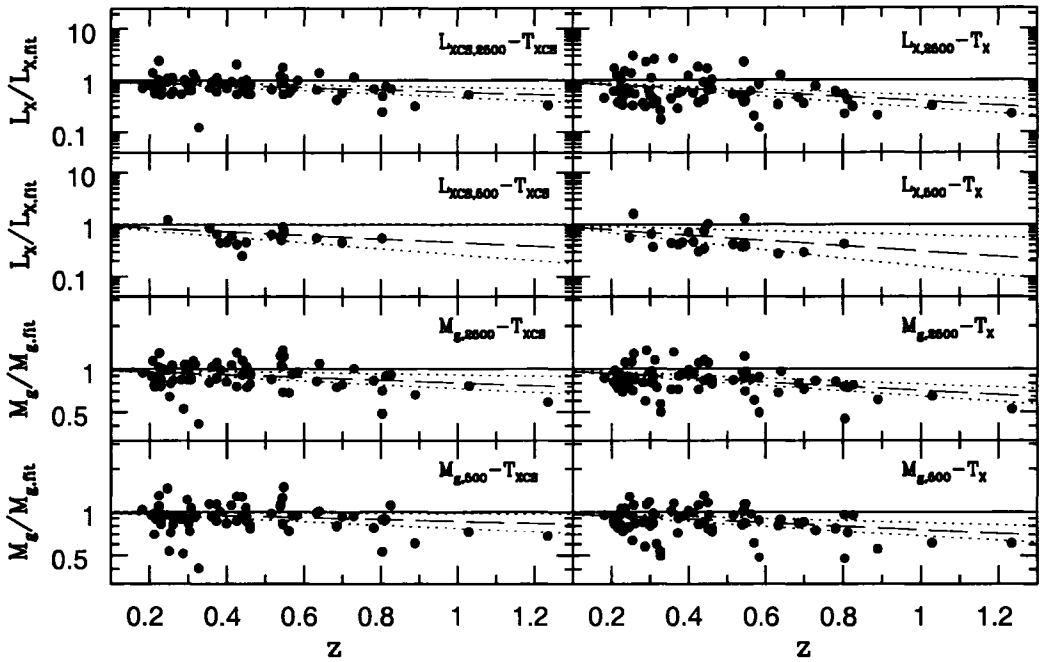

Figure 4.6 — Ratio of measured observable (luminosity or ICM mass) to the best-fit observable–temperature scaling relation, plotted versus redshift. These measurements assume *self-similar evolution.* The horizontal line ($\mathcal{O}/\mathcal{O}_{\rm fit} = 1$) corresponds to no evolution beyond the assumed self-similar evolution, i.e., $\gamma = 0$ in our notation. The dashed and dotted lines correspond to the best fit and 1σ boundaries on γ for each relation.

zero, i.e., the significance of its deviation from the self-similar prediction. Because the distributions of γ are not in general normal, this significance is determined using binned data to measure the probability density at $\gamma = 0$, and integrating to the same probability density on the other side of the peak value. Because we use binned data to estimate this parameter, it can be determined most precisely when γ is significantly different from zero; hence, we quote only at 1% precision for values less than 99%.

All luminosity– and ICM mass–temperature scaling relations have $\gamma < 0$ at greater than the 1σ level. There is clearly an overall tendency for relations to evolve more slowly than expected from the self-similar prediction, i.e., $\gamma < 0$. We can combine multiple probabilities by assuming independence of the scaling relations; though all of the measured properties are of course linked to some extent by their dependence on the underlying ICM structure, X-ray luminosity and ICM mass depend on that structure in very different ways, and the two virial radii which we use result in two rather different perspectives on cluster structure (i.e., r_{500} comes close to looking at the cluster as a whole, while r_{2500} measures a much smaller fraction that is more dependent on core structure and evolution). Combining the results for all four core subtracted relations by multiplying the given probabilities of consistency with zero gives a combined probability of $< 0.1\%$ that all four relations are consistent with the self-similar evolution scenario, ruling out pure self-similar evolution at greater than 3σ confidence. The same relations with non-core subtracted quantities have an even smaller

probability (i.e., $\ll 0.1\%$) of consistency with zero.

We draw your attention to the $z > 0.8$ clusters in our sample because of the special leverage they have on our evolution results. Examination of Figure 4.6 suggests no qualitative difference in the high-redshift population when compared to lower-redshift clusters. For these clusters to bias our results toward more negative evolution, it would require systematically selecting *underluminous* clusters, which is the opposite of what is expected.

The relations involving core subtracted quantities have more positive evolution than those involving non-core subtracted quantities. This could indicate a decrease in clusters with cool cores at higher redshifts, which is expected in the scenario wherein clusters form cool cores over time in the absence of major merging events. The evolution of the cool core fraction remains relatively unexplored; Bauer et al. (2005) found no evolution in the cool core fraction up to $z \sim 0.4$ using spatially resolved spectral analysis, but such an analysis is difficult to carry out at higher redshifts. Vikhlinin et al. (2006) used a measurement of the "cuspiness" of the surface brightness distribution to count cool cores in a sample of clusters at $z > 0.5$, and found a fourfold decrease in the cool core fraction from z=0 to z=0.5, which might support the concept of cool cores indicating a "relaxed cluster" that has not undergone recent major mergers. This concept is being increasingly challenged, however, by results from simulations that ascribe the presence or lack of a cool core to aspects of cluster formation history such as preheating (McCarthy et al. 2004) or early major mergers (Burns et al. 2007), and observational evidence that cool core and non-cool core cluster populations differ in characteristics beyond their morphological state (O'Hara et al. 2006). Burns et al. (2007) specifically studied the redshift evolution of the cool core fraction, and find no change in the fraction up to $z \sim 1$ in simulations that successfully reproduce other aspects of cluster and core structure. Our results here may support the classical notion of cool cores evolving over time, in support of the Vikhlinin et al. (2006) results. Alternatively, a constant cool core fraction could still produce an apparent negative evolution in scaling relation normalization simply because cool cores in those clusters that do have them will tend to grow over time; such a result was reported in simulations by Kay et al. (2007). We further discuss possible evolution in scatter in §4.8.

4.5 Tests of the No Evolution Scenario

We now examine the evolution of scaling relations while assuming no evolution, i.e., we assume no scaling in r_Δ when measuring L_X and M_{ICM}, and when determining the core subtraction radius for T_{XCS} and L_{XCS}; and we do not scale the measured values of L_X and M_{ICM} by any multiple of $E(z)$. Our measured values

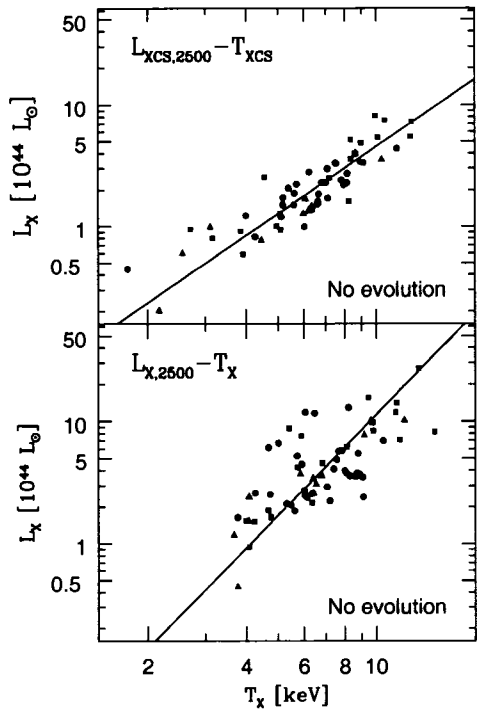

Figure 4.7 — Projected X-ray luminosity within r_{2500} (left) and r_{500}(right), with non-core subtracted (top) and core subtracted (bottom) quantities, plotted versus temperature. These quantities are measured assuming *no evolution*. Luminosity values are scaled to $z = 0$ using the best-fit redshift scaling for each relation, and the best-fit slope is plotted for each relation. Markers correspond to $z < 0.4$ (circles), $0.4 < z < 0.6$ (squares), and $z > 0.6$ (triangles).

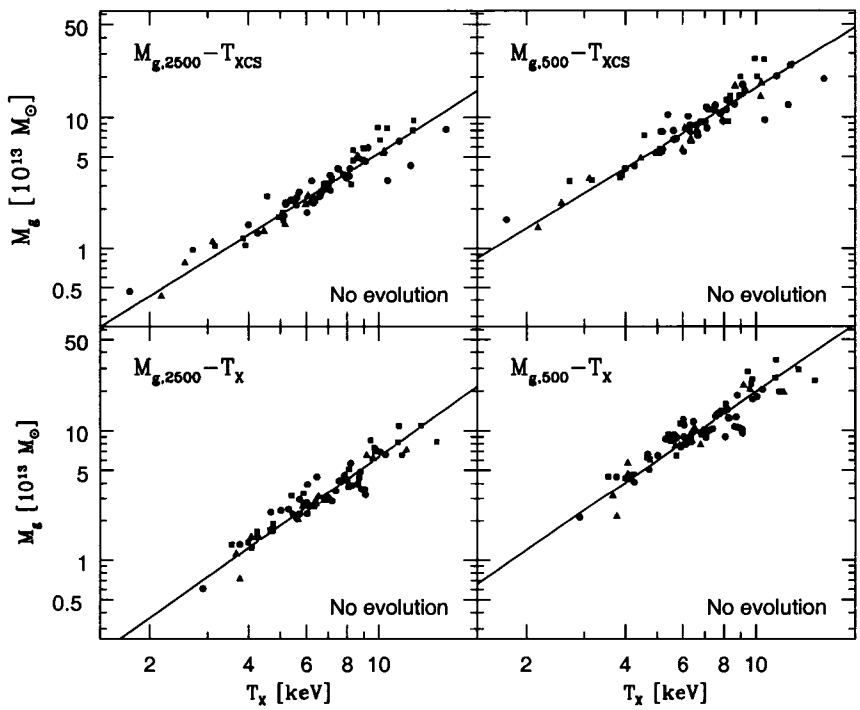

Figure 4.8 — Same as Figure 4.7, but for $M_{\rm ICM}$–$T_{\rm X}$ relations.

Table 4.6: Cluster Measurements Assuming No Evolution

Cluster	$L_{X,2500}$ (10^{44} $L_\odot$)	$M_{ICM,2500}$ (10^{13} $M_\odot$)	$M_{ICM,500}$ (10^{13} $M_\odot$)
A665	3.78±0.04	4.13±0.09	13.42±0.31
A963	...	2.99±0.09	9.63±0.28
RX J0439.0+0520	2.45±0.03	1.46±0.07	3.84±0.19
A1423	2.33±0.05	2.22±0.08	8.53±0.30
ZwCl 2701	2.38±0.02	1.64±0.07	4.76±0.21
A773	3.40±0.04	3.74±0.10	11.72±0.31
A2261	5.41±0.03	3.99±0.12	12.70±0.37
ACO 2246	...	0.59±0.05	2.01±0.16
A1682	1.95±0.08	2.17±0.09	7.94±0.33
A2111	2.11±0.06	2.78±0.09	9.43±0.30
A267	2.75±0.03	2.86±0.09	8.38±0.27
RX J2129.7+0005	4.91±0.03	2.87±0.12	8.37±0.34
RX J0439.0+0715	3.83±0.04	3.35±0.11	9.71±0.32
A521	2.58±0.09	2.71±0.11	11.42±0.47
A1835	12.13±0.06	5.50±0.17	13.62±0.42
A68	3.33±0.06	3.85±0.11	10.04±0.30
MS 1455.0+2232	5.74±0.01	2.27±0.13	6.20±0.34
MS 1006.0+1202	2.23±0.04	2.52±0.11	7.38±0.31
A697	6.48±0.08	6.38±0.17	19.24±0.52
A611	3.46±0.05	3.45±0.11	9.84±0.32
ZwCl 3146	10.85±0.02	4.32±0.19	10.88±0.49
A781	1.97±0.11	2.39±0.13	8.03±0.45
MS 1008.1-1224	2.41±0.04	2.61±0.12	7.69±0.36
RXC J2245.0+2637	4.16±0.03	2.65±0.14	6.94±0.36
A1300	5.09±0.09	4.71±0.16	17.25±0.60
A2744	...	6.67±0.20	16.77±0.51
MS 2137.3-2353	6.15±0.03	2.33±0.15	5.98±0.37
A1995	3.51±0.05	3.59±0.14	8.33±0.33
ZwCl 1358+6245	3.25±0.05	3.47±0.12	9.46±0.34
A1722	2.22±0.05	3.10±0.11	8.84±0.32
RXC J0404.6+1109	1.69±0.11	2.01±0.13	8.59±0.54
RX J1532.9+3021	10.90±0.04	3.78±0.23	10.15±0.61
A370	3.49±0.07	4.25±0.18	11.62±0.50
ZwCl 1953	4.48±0.06	4.02±0.20	11.78±0.58
RXC J0949.8+1707	5.30±0.08	4.42±0.22	13.00±0.63
ClG J1416+4446	1.48±0.03	1.27±0.13	4.06±0.43

Table 4.6, cont.

Cluster	$L_{X,2500}$ (10^{44} $L_\odot$)	$M_{ICM,2500}$ (10^{13} $M_\odot$)	$M_{ICM,500}$ (10^{13} $M_\odot$)
RXC J2228.6+2036 .	5.71±0.11	4.92±0.25	14.68±0.75
MS 0302.7+1658	···	1.27±0.15	4.09±0.49
MS 1621.5+2640	1.98±0.06	2.50±0.17	8.13±0.54
MACS J0417.5-1154.	14.27±0.22	8.17±0.38	25.86±1.21
RXC J1206.2-0848 ..	10.79±0.12	7.91±0.30	23.15±0.89
ClG J0329-0212	6.94±0.04	3.19±0.24	10.32±0.79
RX J1347.5-1145	24.62±0.06	10.58±0.35	26.60±0.89
ClG J1701+6414	1.71±0.03	1.64±0.16	5.69±0.55
3C 295	3.86±0.02	2.19±0.18	5.85±0.47
ClG J1621+3810	4.17±0.04	2.92±0.20	8.52±0.58
ClG J1524+0957	1.48±0.05	1.83±0.20	5.43±0.59
MS 0451.6-0305	8.82±0.11	6.74±0.37	15.49±0.86
MS 0015.9+1609	8.78±0.10	7.14±0.40	20.52±1.15
ClG J1149+2223	7.55±0.18	6.86±0.38	22.15±1.23
ClG J1423+2404	7.87±0.05	3.03±0.31	8.36±0.84
ClG J1354-0221	0.85±0.05	1.19±0.16	3.87±0.52
ClG J0717+3745	12.73±0.23	10.46±0.50	31.03±1.48
ClG J1120+2326	1.35±0.05	1.60±0.21	4.17±0.55
ClG J2129-0741	6.34±0.21	6.23±0.30	17.66±0.86
MS 2053.7-0449	1.37±0.03	1.31±0.19	3.88±0.57
ClG J0647+7015	7.34±0.16	7.89±0.31	21.30±0.83
ClG J0542-4100	2.29±0.08	2.59±0.26	8.68±0.86
ClG J1419+5326	2.13±0.05	1.44±0.23	4.12±0.65
ClG J0744+3927	8.90±0.13	5.86±0.42	18.02±1.29
ClG J1221+4918	2.69±0.07	2.97±0.32	9.09±0.97
ClG J1113-2615	1.02±0.04	1.06±0.21	2.73±0.54
ClG 1137+6625	3.23±0.10	2.46±0.33	6.65±0.89
RX J1350.0+6007 ...	1.31±0.07	1.41±0.28	4.90±0.97
RX J1317+2911	0.38±0.04	0.68±0.15	1.87±0.40
RX J1716+6708	2.96±0.08	2.70±0.34	7.26±0.92
ClG J1056-0337	6.67±0.16	6.14±0.55	19.02±1.71
ClG J1226+3332	8.67±0.17	6.71±0.49	16.52±1.21
ClG J1415+3611	3.03±0.08	2.68±0.41	6.53±0.99
ClG J1252-2927	···	1.90±0.41	6.25±1.36

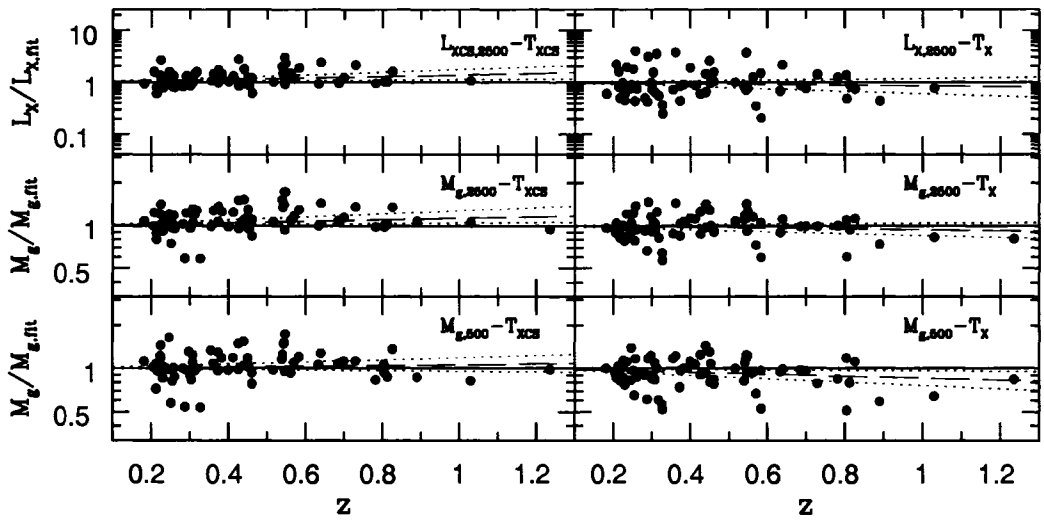

Figure 4.9 — Ratio of measured observable (luminosity or ICM mass) to the best-fit observable–temperature scaling relation, plotted versus redshift. These measurements assume *no evolution*. The horizontal line ($\mathcal{O}/\mathcal{O}_{\rm fit} = 1$) corresponds to no evolution, i.e., $\gamma = 0$ in our notation. The dashed and dotted lines correspond to the best fit and 1σ boundaries on γ for each relation.

for $L_{\rm X}$ and $M_{\rm ICM}$ measured using the non-core subtracted temperature are given in Table 4.6. We do not measure $L_{\rm X,500}$ or $L_{\rm XCS,500}$ in this scenario, as only a handful of clusters have observations of sufficient exposure time and angular extent that we can measure out to the non-evolved r_{500}.

4.5.1 Scaling Relations and Their Evolution

The $L_{\rm X}$–$T_{\rm X}$ and $L_{\rm X}$–$M_{\rm ICM}$ relations are plotted in Figures 4.7 and 4.8, respectively. As in the self-similar evolution case, the slope of the luminosity–temperature relation decreases significantly when core-subtracted quantities are used, and the scatter likewise decreases for both the luminosity and the ICM mass relations. We give the scaling relation parameters from this scenario in Table 4.7, and plot the redshift evolution of the scaling relations in Figure 4.9.

The measured slopes and normalizations in this scenario are consistent with those measured in §4.4, including the tendency for core subtracted relations to have shallower slopes than non-core subtracted relations. Also in common between the two scenarios is the tendency for core subtracted relations to have more positive evolution than non-core subtracted relations.

Single non-core subtracted relations are generally consistent with negative evolution, and core subtracted relations are generally consistent with positive evolution. Combining all three core subtracted relations gives a combined consistency with $\gamma = 0$ (i.e., with the predictions of the no evolution scenario) of 1%; for the non-core subtracted relations, the value is 8%.

Table 4.7. Fit Parameters Assuming No Evolution

Relation	α	A^a	γ	Diff. from 0 (%)[b]	σ_{int}[c]
Core Subtracted Relations					
$L_{XCS,2500}$–T_{XCS}	$1.84^{+0.18}_{-0.14}$	$1.74^{+0.26}_{-0.22}$E44	$0.56^{+0.37}_{-0.35}$	88+	$0.24^{+0.04}_{-0.05}$
$M_{ICM,2500}$–T_{XCS}	1.57 ± 0.07	$2.40^{+0.17}_{-0.16}$E13	$0.20^{+0.20}_{-0.12}$	89+	0.00 ± 0.00
$M_{ICM,500}$–T_{XCS}	1.52 ± 0.08	$7.59^{+0.54}_{-0.51}$E13	$0.10^{+0.19}_{-0.17}$	41+	0.08 ± 0.04
Non-Core Subtracted Relations					
Relation	α	A^a	γ	Diff. from 0 (%)[b]	σ_{int}[c]
$L_{X,2500}$–T_X	$2.75^{+0.34}_{-0.25}$	$2.81^{+0.73}_{-0.58}$E44	-0.25 ± 0.56	36–	0.59 ± 0.09
$M_{ICM,2500}$–T_X	1.78 ± 0.08	$2.57^{+0.18}_{-0.17}$E13	$-0.10^{+0.17}_{-0.15}$	43–	0.13 ± 0.02
$M_{ICM,500}$–T_X	1.74 ± 0.10	$8.13^{+0.58}_{-0.54}$E13	$-0.25^{+0.19}_{-0.18}$	78–	0.14 ± 0.02

[a]In units of $L_\odot$ for L_X–T_X relations, $M_\odot$ for M_{ICM}–T_X relations.

[b]Significance level at which γ differs from zero, as determined by bootstrap sampling and refitting; the sign indicates whether γ is positive (+) or negative (−).

[c]Intrinsic scatter in L_X or M_{ICM} at fixed temperature, expressed in base e.

4.5.2 Summary of No Evolution Scenario Results

The core subtracted scaling relations rule out the "no evolution" scenario at 99% confidence; non-core subtracted relations give less certain results. As in the self-similar evolution scenario, the core subtracted relations have slopes that are consistent with self-similar expectations, and evolution that is positive with respect to the corresponding non-core subtracted relations. Together with the results from the self-similar evolution tests, these findings indicate that cluster scaling relations do evolve, but they evolve less rapidly than the self-similar expectation.

4.6 Testing Evolution of the ICM Fraction

One simple model for the evolution of cluster parameters such as L_X and M_{ICM} is a simple evolution of the gas mass fraction f_{ICM}, i.e., the ratio of the ICM mass to the total mass (baryons + dark matter) of a cluster. It is sometimes assumed in cosmological studies using clusters that f_{ICM} is constant with redshift if clusters are selected appropriately (e.g., Allen et al. 2004), but this assumption is difficult to test because of degeneracies between f_{ICM} measurements and cosmological parameters; Sadat et al. (2005) claim that f_{ICM} does indeed evolve with redshift. Simulations disagree on the baryon fraction evolution, with some claiming to see a negative evolution (e.g., Kay et al. 2007), while others find no evolution (e.g., Crain et al. 2007).

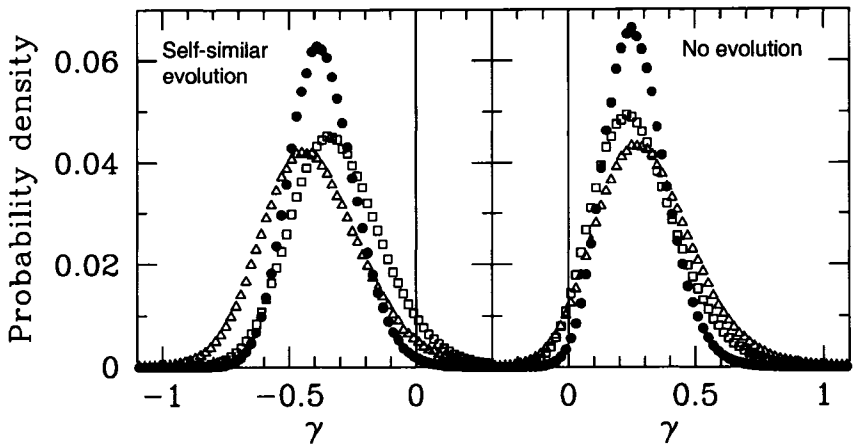

Figure 4.10 — Constraints on the evolution of $f_{\rm ICM}$ for the self-similar evolution (*left*) and no evolution (*right*) scenarios. Open triangles are from the fit to the $L_{\rm XCS,2500}$-$T_{\rm XCS}$ relation (with the values halved, as discussed in the text), open squares are from $M_{\rm ICM,2500}$-$T_{\rm XCS}$ relation, and filled circles are the normalized product of the two. The best-fit to the combined relations gives $\gamma_{f_{\rm ICM}} = -0.39 \pm 0.13$ in the self-similar evolution scenario, and $\gamma_{f_{\rm ICM}} = 0.25^{+0.12}_{-0.11}$ in the no evolution scenario.

We can test whether our data are consistent with an evolution in $f_{\rm ICM}$ by directly combining measured values of γ for individual scaling relations. X-ray luminosity varies proportional to the square of the ICM density, and ICM mass is directly proportional to the ICM density. Because we are working in log space, this means that we combine $\gamma_{M_{\rm ICM}}$ with $\gamma_{L_{\rm X}}/2$. We use the core subtracted relations for this test because these relations are presumably less biased by cluster structural changes in the core, and therefore more sensitive to general changes in the gas fraction.

First we examine the $L_{\rm XCS,2500}$– and $M_{\rm ICM,2500}$–$T_{\rm XCS}$ relations measured in the self-similar evolution scenario. The left panel of Figure 4.10 shows histograms for the values of γ resulting from the bootstrap fitting of the $L_{\rm XCS,2500}$– and $M_{\rm ICM,2500}$–$T_{\rm X}$ relations (triangles and squares, respectively; the values of γ for luminosity have been divided by 2 as explained above); the vertical axis has been scaled so that the values represent the probability of γ falling in each bin. The circles are the product of the two individual distributions, renormalized so that the total probability is unity. The data give a best fit value of $\gamma_{f_{\rm ICM}} = -0.39 \pm 0.13$; the data are inconsistent with $\gamma_{f_{\rm ICM}} = 0$ (i.e., a constant gas fraction) at the 99.1% level.

The right panel of Figure 4.10 shows data calculated in the same way, but in the no evolution scenario. In this scenario we find the best-fit combined scaling to be $\gamma_{f_{\rm ICM}} = 0.25^{+0.12}_{-0.11}$, and inconsistent with $\gamma_{f_{\rm ICM}} = 0$ at the 98% level.

Our results are consistent with the evolution in $L_{\rm X}$ and $M_{\rm ICM}$ originating from a simple evolution in gas mass fraction. While we have not proven this scenario, it is encouraging to note that the values of $\gamma_{M_{\rm ICM}}$ and $\gamma_{L_{\rm X}}/2$ are quite similar in both scenarios, and evolution in $f_{\rm ICM}$ thus provides a consistent explanation

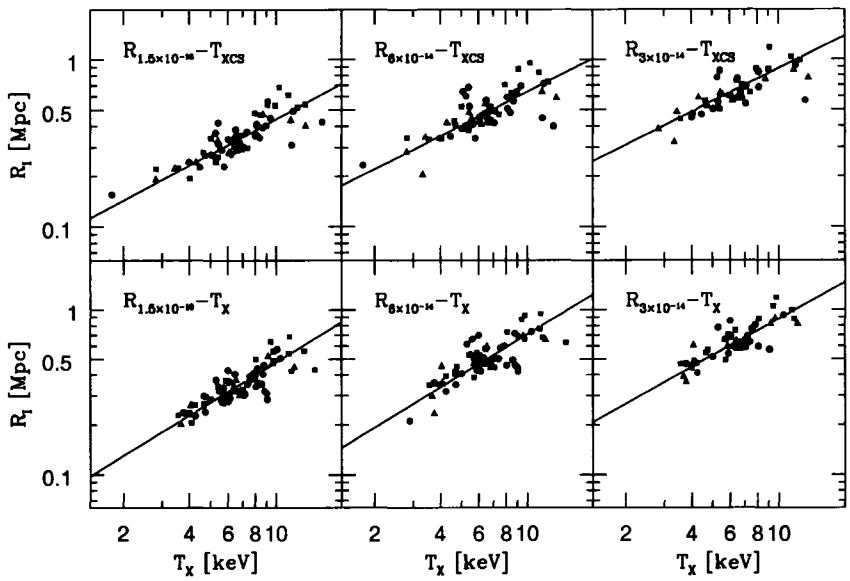

Figure 4.11 — Isophotal size–temperature relations for non-core subtracted (top) and core subtracted (bottom) temperature; the isophote used decreases from left to right. Size values are scaled to $z = 0$ using the best-fit redshift scaling for each relation, and the best-fit slope is plotted for each relation. Markers vary by redshift as in Figure 4.4.

for the evolution of these two rather different physical quantities. The most probable value $\gamma_{f_{\rm ICM}} \simeq -0.4$ in the self-similar evolution scenario suggests a decrease of ~25% in $f_{\rm ICM}$ between redshifts 0 and 1, which would bias distance measurements that assume constant $f_{\rm ICM}$ at the ~17% level ($d_A \propto f_{\rm ICM}^{2/3}$; e.g., Rines et al. 1999).

Note that we have measured the evolution of $f_{\rm ICM}$ specifically within the radius r_{2500}. We do not attempt a similar measurement at r_{500} because of a lack of luminosity measurements at that radius in the no evolution scenario, and the very large uncertainties on the $L_{\rm XCS,500}$–$T_{\rm XCS}$ relation in the self-similar evolution scenario. There is in both scenarios and in both core subtracted and non-core subtracted relations a tendency for $M_{\rm ICM,500}$ to evolve more slowly than $M_{\rm ICM,2500}$(though only at the 0.5–1σ level); this is consistent with observations and simulations which find that the evolution in $f_{\rm ICM}$ decreases with increasing radius, with evolution nearing zero at the virial radius (e.g., Sadat et al. 2005; Ettori et al. 2006).

4.7 Evolution of Isophotal Size

We now examine the evolution of isophotal size–temperature scaling relations. This is done separately from the previous "self-similar evolution" and "no evolution" because as discussed in §4.2, for clusters that are described by a β model with $\beta = \frac{2}{3}$, the two scenarios give the same result (Mohr et al. 2000). That is, under

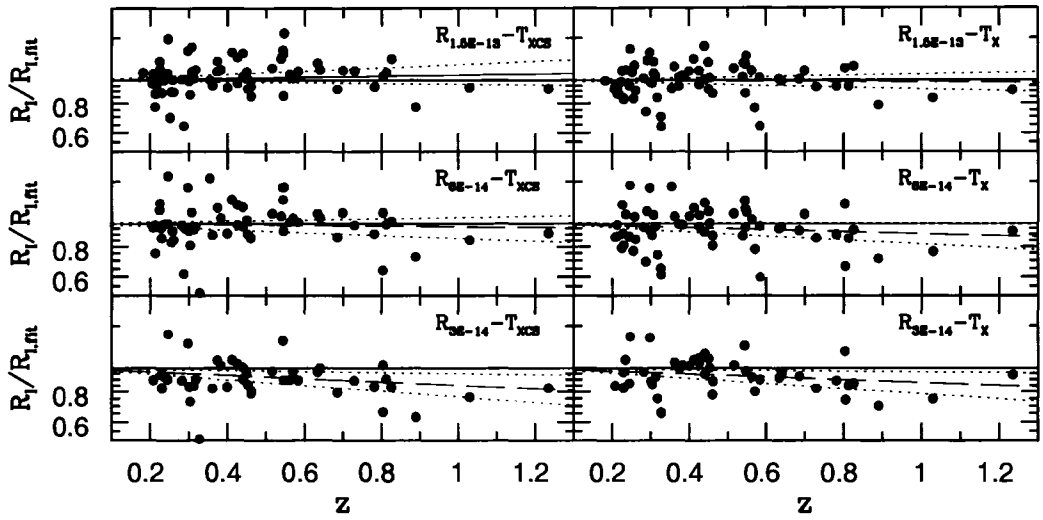

Figure 4.12 — Ratio of measured isophotal size to the best-fit size–temperature scaling relation, plotted versus redshift. These measurements assume no evolution. The horizontal line ($R_I/R_{I,\mathrm{fit}} = 1$) corresponds to no evolution, i.e., $\gamma = 0$ in our notation. The dashed and dotted lines correspond to the best fit and 1σ boundaries on γ for each relation.

these assumptions, the size–temperature relation does not evolve with redshift. While this potentially makes the size–temperature relation useful as a means to study the evolution of the angular diameter distance, and hence as a tool for studying cosmology, it makes it less useful for constraining the evolution of the ICM and cluster structure as we have done with luminosity and ICM mass relations.

4.7.1 Scaling Relations and Their Evolution

Size–temperature scaling relations are shown in Figure 4.11; as with the previous scaling relation plots, these have had the measured redshift evolution projected out. Best-fit scaling relation parameters are given in Table 4.8. The slopes of the relations using core subtracted temperatures are consistent with the theoretical value $\alpha = \frac{2}{3}$ (Mohr et al. 2000), and the relations with non-core subtracted temperature are somewhat higher. Our fit slope for the $R_{3\times10^{-14}}$-T_{X} relation is $0.74^{+0.08}_{-0.07}$, which differs significantly from the value $\alpha = 0.93 \pm 0.11$ found by Mohr et al. (2000) using *ROSAT* PSPC images and literature values for T_{X}.

Redshift evolution of the isophotal size relations is shown in Figure 4.12. For the fits to the entire sample, the isophotal size relations show little or no evolution in the isophote closest to the core, and a trend toward more negative evolution as the isophote used decreases, i.e., as one examines the cluster at distances further from the core.

Having shown in §4.6 that the evolution in L_{X} and M_{ICM} with respect to the self-similar expectation scan be modeled by a simple evolution in the gas fraction, we can check for consistency of that evolution

Table 4.8. Fit Parameters For Isophotal Size Relations

Core Subtracted Relations					
Relation	α	A (Mpc)	γ	Diff. from 0 (%)[a]	$\sigma_{\rm int}$[b]
$R_{1.5\times10^{-13}}$–$T_{\rm XCS}$	$0.70^{+0.07}_{-0.06}$	0.31 ± 0.02	$0.08^{+0.17}_{-0.14}$	42+	0.13 ± 0.02
$R_{6\times10^{-14}}$–$T_{\rm XCS}$	$0.66^{+0.09}_{-0.08}$	0.46 ± 0.03	$-0.05^{+0.15}_{-0.18}$	33–	0.16 ± 0.02
$R_{3\times10^{-14}}$–$T_{\rm XCS}$	0.65 ± 0.10	$0.63^{+0.05}_{-0.04}$	-0.26 ± 0.18	87–	$0.12^{+0.03}_{-0.02}$
Non-Core Subtracted Relations					
Relation	α	A (Mpc)	γ	Diff. from 0 (%)[a]	$\sigma_{\rm int}$[b]
$R_{1.5\times10^{-13}}$–$T_{\rm X}$	0.81 ± 0.07	0.32 ± 0.01	$-0.03^{+0.13}_{-0.11}$	13–	0.13 ± 0.01
$R_{6\times10^{-14}}$–$T_{\rm X}$	0.81 ± 0.09	0.47 ± 0.03	-0.16 ± 0.16	68–	0.16 ± 0.02
$R_{3\times10^{-14}}$–$T_{\rm X}$	$0.74^{+0.08}_{-0.07}$	$0.60^{+0.06}_{-0.04}$	-0.22 ± 0.17	79–	0.14 ± 0.02

[a]Significance level at which γ differs from zero, as determined by bootstrap sampling and refitting; the sign indicates whether γ is positive (+) or negative (−).

[b]Intrinsic scatter in R_I at fixed temperature, expressed in base e.

with the isophotal size results. The brightness at a given cluster radius r is related to the gas fraction $f_{\rm ICM}$ as $I(r) \propto f_{\rm ICM}^2$, and so it can be shown that for a cluster described by a spherical β model the measured isophotal size scales with $I(r)$ as $R_I \propto I(r)^{1/(6\beta-1)}$ (Mohr et al. 2000). Thus we expect

$$R_I \propto f_{\rm ICM}^{2/(6\beta-1)}, \tag{4.12}$$

which, for the standard value of $\beta = \frac{2}{3}$ (e.g., Jones & Forman 1984; Mohr et al. 1999), means that isophotal size should scale as $f_{\rm ICM}^{2/3}$. For our self-similar evolution measurement of $\gamma_{f_{\rm ICM}} = -0.39 \pm 0.13$, this would predict $R_I \propto (1+z)^{-0.26\pm0.09}$, in good agreement with the directly measured evolution of $\gamma = -0.26 \pm 0.18$ in the $R_{3\times10^{-14}}$–$T_{\rm XCS}$ relation, and of $\gamma = -0.05^{+0.15}_{-0.18}$ in the $R_{6\times10^{-14}}$–$T_{\rm XCS}$ relation. More positive evolution at higher isophotes may be an indication of structural changes as clusters evolve and the density profiles of clusters become more peaked toward the center.

4.7.2 Prospects for Cosmology Using Isophotal Size

As mentioned above, the predicted non-evolution of R_I with redshift makes these size measurements a promising source of angular diameter distances, which can be used to constrain cosmological parameters. Such an undertaking is beyond the scope of this paper, but we sketch here the basic ideas underlying such a measurement.

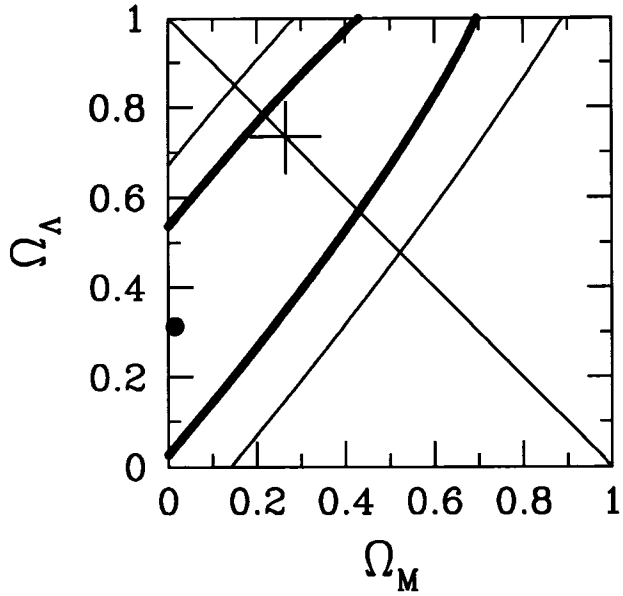

Figure 4.13 — Constraints on Ω_M and Ω_Λ from fitting the angular diameter distances determined from isophotal sizes. The thick and thin contours mark the boundaries of the 1 and 2σ confidence regions, respectively. The circle denotes the best fit $\Omega_M = 0.02$, $\Omega_\Lambda = 0.31$, and the cross marks our adopted cosmology for this paper, $\Omega_M = 0.266$, $\Omega_\Lambda = 0.734$.

If isophotal size indeed evolves in a manner predictable by the evolution in $f_{\rm ICM}$, then one can use a measured angular isophotal size θ_I, together with a physical isophotal size R_I for the same cluster predicted from a scaling relation, to determine the angular diameter distance, $d_A = R_I/\theta_I$; this can then be used to measure the cosmological parameters which determine $d_A(z)$. As a test, we use θ_I measured from our $R_{3\times10^{-14}}$ sample, and use the best-fit slope and normalization found for the $R_{3\times10^{-14}}$-$T_{\rm XCS}$ relation to predict $R_I(T_{\rm X}, z)$. Because we have found evolution in $L_{\rm X}$ and $M_{\rm ICM}$ which suggests evolution in $f_{\rm ICM}$, we adopt the best-fit $f_{\rm ICM}$ evolution $\gamma_{f_{\rm ICM}} = -0.39$ and its consequent isophotal size evolution $\gamma_{R_I} = -0.26$ in the size–temperature relation, as discussed above. Uncertainties in d_A are a combination of the temperature uncertainty and the measured intrinsic scatter in the $R_{3\times10^{-14}}$-$T_{\rm XCS}$ relation. Note that this is not truly an independent cosmological test, as the isophotal size–temperature relation is measured using physical sizes that are determined using angular diameter distances from an assumed cosmology, and because our measurements of the evolution in $L_{\rm X}$ and $M_{\rm ICM}$, and hence $f_{\rm ICM}$, likewise assume a particular cosmology. Our intention here, however, is simply to demonstrate the method, not to place new constraints on cosmology.

Figure 4.13 shows confidence intervals for the density parameters Ω_M and Ω_Λ (we fix H_0 to our assumed value of 70.9 km s^{-1} Mpc^{-1}). The uncertainties on both parameters are quite large; fully marginalized constraints are $\Omega_M = 0.02^{+0.49}_{-0.02}$, $\Omega_\Lambda = 0.31^{+0.59}_{-0.19}$. As can be seen from Figure 4.14, these data do not reach redshifts high enough to place tight constraints on cosmology; however, we do recover our input cosmology

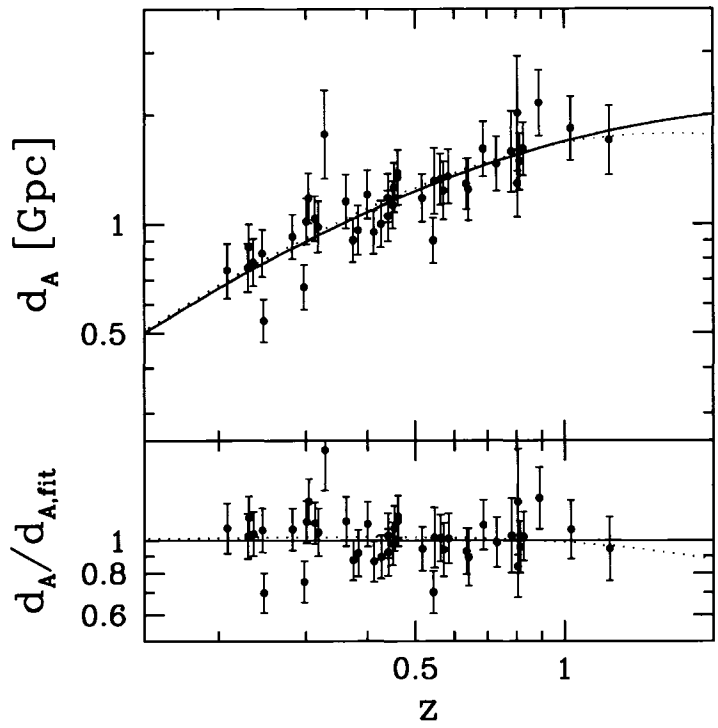

Figure 4.14 — Measured angular diameter distance d_A plotted versus redshift for the $R_{3\times10^{-14}}$ sample. The solid line shows $d_A(z)$ for the best-fit measured cosmology $\Omega_M = 0.02$, $\Omega_\Lambda = 0.31$, and the dotted line shows $d_A(z)$ for our adopted cosmology $\Omega_M = 0.266$, $\Omega_\Lambda = 0.734$.

within the 1σ confidence region.

This combination of the use of L_X–T_X and M_{ICM}–T_X relations to constrain the evolution of the ICM, and R_I–T_X relations to measure distances is an approach that deserves further attention. As X-ray surveys that include spectroscopic temperature measurements push to higher redshifts, the use of isophotal sizes to measure angular diameter distances as demonstrated here should provide a new source of cosmological measurements, complementary to other cluster methods and to CMB and supernova constraints.

4.8 Scatter in Scaling Relations

This paper has focused on the evolution of the normalization of observable–temperature scaling relations. Here we briefly discuss the *scatter* about those scaling relations, i.e., the variation in the ICM distribution from cluster to cluster at fixed temperature. Understanding the precise origins of scatter helps both in understanding cluster physics such as cool core development and merger effects, and in understanding sources of uncertainty in cosmological studies that use observables such as X-ray luminosity and temperature as proxies for cluster mass. As shown by O'Hara et al. (2006), the cluster central surface brightness I_0 is

Table 4.9. Scatter and Slope Comparisons, Core Subtracted vs. 3-Parameter

Relation	Standard Relation		Core Subtracted		3-Parameter		
	α	$\sigma_{\rm int}$	α	$\sigma_{\rm int}$	α	β	$\sigma_{\rm int}$
$L_{\rm X,2500}$–$T_{\rm X}$	$2.75^{+0.29}_{-0.26}$	$0.60^{+0.08}_{-0.09}$	$2.00^{+0.23}_{-0.19}$	0.28 ± 0.05	1.72 ± 0.13	0.39 ± 0.03	0.21 ± 0.03
$L_{\rm X,500}$–$T_{\rm X}$	$2.35^{+0.33}_{-0.24}$	$0.39^{+0.12}_{-0.10}$	$2.26^{+0.29}_{-0.33}$	$0.21^{+0.08}_{-0.07}$	1.72 ± 0.13	$0.28^{+0.06}_{-0.04}$	$0.15^{+0.02}_{-0.07}$
$M_{\rm ICM,2500}$–$T_{\rm X}$	1.82 ± 0.08	0.14 ± 0.02	$1.63^{+0.09}_{-0.08}$	$0.00^{+0.05}_{-0.00}$	1.70 ± 0.07	0.10 ± 0.02	0.07 ± 0.02
$M_{\rm ICM,500}$–$T_{\rm X}$	1.74 ± 0.09	0.13 ± 0.02	1.56 ± 0.10	0.09 ± 0.04	$1.70^{+0.10}_{-0.07}$	0.02 ± 0.02	0.12 ± 0.02
$R_{1.5\times10-13}$–$T_{\rm X}$	0.81 ± 0.07	0.13 ± 0.01	$0.70^{+0.07}_{-0.06}$	0.13 ± 0.02	0.89 ± 0.09	0.01 ± 0.02	0.13 ± 0.02
$R_{6\times10-14}$–$T_{\rm X}$	0.81 ± 0.09	0.16 ± 0.02	$0.66^{+0.09}_{-0.08}$	0.16 ± 0.02	0.82 ± 0.09	$-0.02^{+0.03}_{-0.02}$	0.16 ± 0.02
$R_{3\times10-14}$–$T_{\rm X}$	$0.74^{+0.08}_{-0.07}$	0.14 ± 0.02	0.65 ± 0.10	$0.12^{+0.03}_{-0.02}$	0.76 ± 0.08	-0.03 ± 0.02	0.13 ± 0.02

Note. — Scatter is given in base e.

strongly correlated with central cooling time and reflects the core structure of clusters. In this section we examine the use of I_0 to reduce scatter in scaling relations, and to examine the redshift evolution of cluster structure.

4.8.1 Reducing Scatter: Two Approaches

As shown in previous sections, the total scatter in scaling relations generally decreases when core-subtracted quantities are used, reflecting the separation in cool core and non-cool core populations that is observed in most scaling relations (e.g., Fabian et al. 1994; Markevitch 1998; McCarthy et al. 2004; O'Hara et al. 2006). O'Hara et al. (2006) demonstrated that central surface brightness I_0 can be used as a proxy for cool core "strength" in a three parameter ($\mathcal{O}$–$T_{\rm X}$–I_0) scaling relation, reducing the scatter in scaling relations that is introduced by biases to both the temperature and to the other observable ($L_{\rm X}$, $M_{\rm ICM}$, R_I) in the relation. With the data presented here we can compare the three-parameter approach to the use of core subtracted quantities, to determine whether either method results in lower scatter than the other.

Rather than using the β model values for I_0, as in O'Hara et al. (2006), we estimate I_0 by simply averaging the surface brightness within $0.05r_{500}$ of the brightness peak. Since our intention is to use I_0 to parametrize the development of cool cores, this method is likely to give more accurate results than the surface brightness fitting which, even when a double β model is used, may not accurately reflect the structure around the brightness peak of a non-spherically symmetric cluster. We fit a scaling relation of the form

$$\mathcal{O} \propto T_{\rm X}^{\alpha} I_0^{\beta} (1+z)^{\gamma}, \tag{4.13}$$

using the orthogonal fit (Eq. 4.11) appropriately modified for the additional parameter.

Table 4.9 gives the $T_{\rm X}$ dependence and intrinsic scatter for seven relations using non-core subtracted

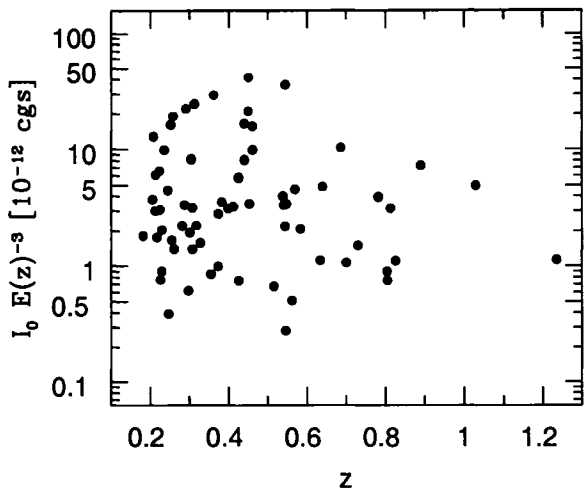

Figure 4.15 — Central surface brightness I_0 versus redshift. The values of I_0 have been scaled by $E(z)^{-3}$, as described in the text, and are given in cgs units, i.e., erg s^{-1} cm^{-2} arcmin^{-2}.

quantities (e.g., L_X–T_X), for the same relations using core subtracted quantities (e.g., L_{XCS}–T_{XCS}), and for the same relations adding the third parameter I_0 (e.g., L_X–T_X–I_0). The 3-parameter L_X relations have even lower intrinsic scatter than the core subtracted relations; for the M_{ICM} relations, the reverse is true. The scatter is little different between the different methods for the isophotal size relations, with perhaps slightly lower scatter in the core subtracted relations.

Interestingly, the slopes for the 3-parameter L_X relations are even lower than those of the core subtracted relations, and are $\sim 2\sigma$ lower than the self-similar expectation $\alpha = 2$. For the M_{ICM} and R_I relations, however, the 3-parameter slopes are consistent with those of the original relation, i.e., steeper than the core subtracted relations.

The M_{ICM} and R_I results by themselves would suggest that the three-parameter fit does not remove cool core-induced average temperature biases as completely as using core subtracted temperatures does; i.e., the brightness of a cluster's core is not a perfect indicator of the coolness of that core. The reduced scatter in the three-parameter L_X relations compared with the core subtracted relations, however, indicates that differences in cool core and non-cool core clusters persist outside the $0.2r_{500}$ core exclusion radius. Together, these results may lend some additional weight to the argument that cool core and non-cool core clusters differ in ways other than their apparent relaxation as determined by the development of a cool, dense core.

4.8.2 Evolution of Scatter

As mentioned in §4.4.2, we see a qualitative decrease in scatter at higher redshifts. Kay et al. (2007) found a decrease of a factor of ~3 in the luminosity–temperature relation in simulations, which they ascribe to

merger effects at lower redshift. However, observational studies have found that clusters are in fact more structurally disturbed at higher redshift (e.g., Jeltema et al. 2005). Further more, cool cores are nearly ubiquitous in the Kay et al. (2007) simulations at all redshifts, in contrast to observational results that find a fairly constant cool core fraction of ~50% up to $z = 0.4$ (Bauer et al. 2005); O'Hara et al. (2006) showed that cool core-related effects, and not mergers, are the primary contributors to scaling relation scatter at low redshift, and so clearly accurate simulation of core evolution is required if simulations are to constrain the evolution of this scatter.

One way of gauging the effects of cool core development on scaling relation scatter is to look at the evolution of the central surface brightness I_0. In Figure 4.15 we plot I_0, measured as described in §4.8.1, redshift. Like other cluster observables, I_0 should evolve with redshift as clusters grow and the average density drops with the cosmic expansion. Because I_0 is a measurement of the emission from a cluster along the line of sight through its center, i.e.,

$$I_0 \propto \int n_e^2 \, dr, \tag{4.14}$$

and density depends on redshift as as $E(z)^2$, and cluster radius depends on redshift as $E(z)^{-1}$, we expect $I_0 \propto E(z)^3$ if clusters evolve self-similarly. Thus the values of I_0 in Figure 4.15 are scaled by $E(z)^{-3}$, and if clusters evolve self-similarly we would expect no average change with redshift in $I_0 E(z)^{-3}$ as plotted.

Qualitatively, however, it appears that the clusters with the highest I_0 appear at low redshift, indicating a change in core structure at these redshifts. This is consistent with our findings that scaling relations with core subtracted quantities evolve faster with redshift than those with non-core subtracted quantities. Furthermore, the overall scatter appears to increase at lower redshifts, consistent with what we have found in observable–temperature relations, indicating a wider range of core and other structural variations as clusters develop. Together, these trends can be explained by an increasing cool core fraction, or an increase the the strengths of cool cores in those clusters that have them, at lower redshifts.

4.9 Discussion

Our study indicates that cluster evolution is inconsistent with the simple self-similar model of cluster formation via gravitational collapse with no other heating or cooling processes. There is a substantial body of observational work in this area already, so in this section we discuss the similarities and differences between our work and earlier studies of scaling relation evolution. The ultimate goal of such observations is to constrain models of cluster formation; predictions of how cluster evolution will be modified by non-gravitational

processes can be made both via simple analytical models (e.g., Voit 2005) and from detailed hydrodynamical simulations (e.g., Muanwong et al. 2006).

4.9.1 Luminosity–Temperature

The X-ray luminosity–temperature relation is by far the most studied cluster scaling relation, with several studies using *Chandra* or *XMM*. These studies have generally found evolution in L_X–T_X relations that is either consistent with the self-similar expectation (e.g., Vikhlinin et al. 2002; Lumb et al. 2004; Kotov & Vikhlinin 2005; Maughan et al. 2006) or more negative (e.g., Ettori et al. 2004b; Branchesi et al. 2007). An interesting exception is Morandi et al. (2007), who found positive evolution when using their entire 24 cluster sample, but marginally negative evolution when using only the 11 clusters which were identified as having cool cores.

Qualitative examination of the redshift scaling in our sample (Figures 4.6, 4.9, and 4.12) clearly indicates the need to include clusters at redshifts as high as possible. Of the other studies mentioned above, the only ones that extend to redshifts beyond $z = 0.8$ are Ettori et al. (2004b) and Branchesi et al. (2007), who find negative evolution with respect to self-similar, as we do; Vikhlinin et al. (2002), who see no evolution with respect to self-similar, but whose methods (e.g., measurement of luminosities within fixed 2 Mpc apertures) are quite different from later studies, making comparison difficult; and Maughan et al. (2006), whose result is only marginally consistent with the self-similar expectation.

The work of Branchesi et al. (2007) in particular is interesting to compare to ours, because they use a *Chandra* sample covering a similar redshift range (though with only 17 members), and study two scenarios similar to our self-similar and no evolution scenarios. They find negative evolution with respect to self-similar, though at lower significance than our result; with an additional 22 clusters from three other *Chandra* studies, the significance increases. In a no evolution scenario, they find the L_X–T_X relation evolution to be consistent with zero, as we do in our $L_{X,2500}$–T_X relation, which is most directly comparable. However, Branchesi et al. (2007) additionally measure scaling with respect to slopes and normalizations from local relations, obtain poor fits, and conclude that there is different evolution in the luminosity–temperature relation between $0 < z \lesssim 0.3$ and above this range. As discussed, however, there are systematic differences between cluster parameters measured with different instruments, or even the same instrument in different studies, as is shown in the Branchesi et al. (2007) results where fits worsen as additional clusters are added from other *Chandra* studies. If there is a sharp change at low redshift, quantifying it will require a homogeneously reduced sample, a task made unfortunately difficult for *Chandra* by its small field of view.

Results from simulations suggest possible explanations for the slower than self-similar evolution that we

observe in the L_X–T_X relation. While not trying to exactly duplicate observed relations, Muanwong et al. (2006) produced simulations using different models for the increase in entropy of the ICM. Their results show that, as naively expected, a simple radiative cooling model results in faster than self-similar evolution in luminosity–temperature because of reduced mean cluster temperatures and increased luminosities. They found slower than self-similar evolution using simple preheating and stellar feedback models, with the latter's negative evolution significantly greater than the former. While their models are simple and cannot be directly used to test specific realistic models, these results do illustrate the usefulness of scaling relations in constraining cluster physics.

Ettori et al. (2004a) and Kay et al. (2007) have studied scaling relation evolution in simulations that include radiative cooling, star formation, and feedback. Both studies found significant ($\gg 3\sigma$) negative evolution with respect to self-similar in bolometric $L_{X,500}$–T_X relations; specifically, Ettori et al. (2004a) found $\gamma = -0.76 \pm 0.08$ (depending on the exact method used; the other possible values are the same within the uncertainty), and Kay et al. (2007) found $\gamma = -0.98 \pm 0.03$ when using non-core subtracted quantities, and $\gamma = -0.61 \pm 0.04$ when measuring luminosities and temperatures excluding the central 50 kpc. Though direct comparisons may not be possible given differences in measurement of cluster temperatures between simulation and observation, differences in how the luminosities are measured, and the fact that our $L_{X,500}$ samples are relatively small and consequently have large uncertainties in their fit parameters, the simulation results are consistent with our results in Table 4.5 for $L_{X,500}$ and $L_{X,2500}$ relations. The more negative scaling in the non-core subtracted relation that Kay et al. (2007) found in simulations is matched by our data, and indicates that the primary source of the slower than self-similar evolution in the L_X–T_X relation is due to clusters being underluminous at higher redshifts, and not to temperature biases from cores. This slower than expected increase in luminosity at high redshifts indicates a potential source of difficulty for X-ray cosmology surveys, in that it may be more difficult to find large numbers of high-redshift clusters than has generally been assumed.

4.9.2 ICM Mass–Temperature

The ICM mass–temperature relation is less well studied than luminosity–temperature, and results are more varied. Vikhlinin et al. (2002) found significantly positive evolution relative to the self-similar expectation when measuring masses within a radius defined in terms of the average baryon density of the Universe; Ettori et al. (2004b) found marginally significant (1–2 σ) negative evolution with respect to self-similar ($\gamma = -(0.1$–$0.4)$, depending on the method used); Maughan et al. (2006) claim consistency of their high-redshift sample with low-redshift clusters when self-similar scaling is applied, though they do not attempt to directly measure

any evolution; and Morandi et al. (2007) find significantly positive evolution with respect to self-similar. The simulations of Ettori et al. (2004a) predict negative evolution ($\gamma = -(0.1\text{–}0.2)$, depending on the method) at the 1–2 σ level. To this we compare our results, in which we find that $M_{\rm ICM}$ has negative evolution with respect to self-similar at the 1–3 σ level, depending on the radius and whether core subtracted parameters are used.

4.9.3 Gas Fraction

An unchanging gas mass fraction, or one that changes in easily quantifiable ways, is an essential component of cosmological studies that use measurements of cluster gas mass fractions to study cosmology (e.g., Rines et al. 1999; Ettori et al. 2003; Allen et al. 2004, 2007). There are, however, several complications to this use of $f_{\rm ICM}$, which varies by cluster mass and by radius within a cluster (e.g., David et al. 1995; Mohr et al. 1999; Sanderson et al. 2003; Sadat et al. 2005). Sadat et al. (2005) found that measured gas fractions at high redshift differ from local measurements depending on the cosmology used, and that in particular there appeared to be a decrease in $f_{\rm ICM}$ at higher redshifts when assuming a standard ΛCDM cosmology, consistent with our findings that $f_{\rm ICM}$ within r_{2500} decreases with redshift relative to the self-similar expectation. The angular diameter distance of clusters, which is used in these cosmological studies, varies with $f_{\rm ICM}$ as $d_A \propto f_{\rm ICM}^{2/3}$, and so our observed $\sim$25% decrease in $f_{\rm ICM}$ between redshifts 0 and 1 corresponds to a decrease of $\sim$17% in d_A over the same redshift range.

Simulations that include radiative cooling, star formation, and feedback processes likewise predict this decrease in $f_{\rm ICM}$ with redshift, with the magnitude of that decrease being larger at smaller fractions of the cluster virial radius (e.g., Kravtsov et al. 2005; Ettori et al. 2006). As with the $L_{\rm X}$ and $M_{\rm ICM}$ evolution, the predicted magnitude of this evolution differs according to the simulation parameters and the numerical codes used (Ettori et al. 2006), and so observational results such as ours will provide constraints as simulation quality improves.

As has been demonstrated Ferramacho & Blanchard (2007), the results obtained from cosmological studies that assume constant gas fraction depend heavily on the radius within which measurements are made, with radii closer to the virial radius giving results that disagree greatly with the concordance model. Though measurements at large radii require extrapolation that may introduce additional biases, such results when combined with evidence of the radial and redshift dependence of $f_{\rm ICM}$ give strong warning against ready acceptance of cosmological results that assume constant $f_{\rm ICM}$, particularly when measurements are made at small radii such as r_{2500}.

Though our results suggest difficulties for cosmological studies that assume constant $f_{\rm ICM}$, we have

presented in §4.7.2 an alternative method for studying cosmology that involves using information about the evolution of $f_{\rm ICM}$ to constrain the evolution of angular diameter distances. Though the measurements that are used to measure the evolution of $L_{\rm X}$ and $M_{\rm ICM}$, and thus $f_{\rm ICM}$, themselves have a cosmology dependence, the dependence on d_A of $L_{\rm X}$ and $M_{\rm ICM}$ is rather different from that of R_I, and by cycling through input cosmologies any degeneracy can be identified.

4.10 Conclusions

We study the evolution of the ICM using X-ray scaling relations measured from a large, homogeneously analyzed sample of clusters spanning $0.2 \lesssim z \lesssim 1.2$. We use luminosity– and ICM mass-temperature relations, including both relations with and without core subtracted quantities, to test scenarios of standard "self-similar evolution" and of "no evolution". We also study the evolution of isophotal size–temperature relations, for which (under certain assumptions) these two scenarios are identical. Finally, we compare the scatter in scaling relations after attempting to reduce cool core-induced scatter in two different ways. Our principal results are as follows.

1. Luminosity– and ICM mass-temperature relations evolve less rapidly than expected in the self-similar evolution scenario; that is, clusters at higher redshifts have systematically lower luminosity and ICM mass at a given temperature than would be expected if clusters evolved self-similarly. The core subtracted relations have a combined consistency with the self-similar prediction of <0.1%; non-core subtracted relations are even more inconsistent with the self-similar prediction.

2. The data are also inconsistent with the no evolution scenario, though not at as great a confidence level as in the self-similar scenario. The core subtracted relations have positive evolution in this scenario (i.e., evolve more rapidly than expected at higher redshift), and combined probability of consistency with zero of 1%.

3. The evolution in the $L_{\rm XCS}$–$T_{\rm XCS}$ and $M_{\rm ICM}$–$T_{\rm XCS}$ relations is consistent with a simple evolution in gas fraction, with evolution in $f_{\rm ICM}$ at $> 99\%$ confidence ($\gamma_{f_{\rm ICM}} = -0.39 \pm 0.13$) in the self-similar evolution scenario when using observables measured within r_{2500}.

4. Isophotal size evolves with redshift at a rate that depends on the isophote used, reflecting evolution in the ICM spatial distribution in clusters. Evolution of isophotal size at a low isophote (i.e., well away from the core) is consistent with that expected given the measured $f_{\rm ICM}$ evolution.

5. Relations with core subtracted quantities in general have more positive evolution than relations with the cores included, suggesting that either the cool core fraction decreases with increasing redshift, or that the cool core fraction remains constant but the cores that do exist are weaker at high redshift. This is supported by direct observations of the redshift dependence of central surface brightness, a good indicator of cool core development; the scatter and magnitude of I_0 appear to increase at low redshift.

6. Core subtracted relations generally have slopes shallower than non-core subtracted relations, and thus are more consistent with the slopes predicted by the self-similar model for each scaling relation.

7. The use of core subtracted quantities for scaling relations and the use of non-core subtracted quantities with the addition of a third parameter, the central surface brightness, both significantly reduce scaling relation scatter by compensating to some extent for cool core-related effects.

8. Scatter in observables at fixed temperature appears to decrease with redshift. This could indicate an increase in the cool core fraction, or an increase in the strength of cool cores in those clusters that have them.

Cluster simulations are still improving with regard to their ability to accurately model non-gravitational processes and thus to directly test specific models by comparison to observational data. However, our results of negative evolution with respect to self-similar expectations in $L_{\rm X}$ and $M_{\rm ICM}$, and consequently in $f_{\rm ICM}$, provide important constraints for future computational studies. Our findings provide new warnings with regard to the assumptions made when using $f_{\rm ICM}$ measurements to study cosmology. At the same time, the combination of isophotal size measurements with measurements of the evolution of $f_{\rm ICM}$ provides a promising tool for measuring angular diameter distances and hence constraining cosmology in a manner complementary to more established techniques.

Chapter 5

Summary and Future Directions

5.1 Summary of Main Results

We have identified a cold front in the nearby merging system A2319, and proposed a model wherein two subclusters are merging in a trajectory well out of the plane of the sky. Remarkably, the bulk properties of A2319 are not significantly perturbed relative to the expected values predicted by scaling relations.

Pursuing this issue of merging effects on cluster bulk properties, we have shown that in fact cool core-related phenomena, and not mergers, are the primary source of scatter in cluster scaling relations. This surprising result, with greater scatter in the cool core cluster population than in non-cool core clusters, may support cluster formation scenarios in which the presence or lack of a cool core is determined by factors beyond simply time since last major merger. In the course of this work, we have shown that central surface brightness can be used to dramatically decrease the scatter in scaling relations by acting as a proxy for cool core "strength", a finding that should prove beneficial in cluster cosmology surveys that use X-ray luminosity as a proxy for cluster mass.

Finally, we have used a large, homogeneously analyzed sample of clusters to show that the evolution in cluster bulk properties is inconsistent with the predictions of simple self-similar models of cluster formation. Effects of core structure are again apparent in this work, as scaling relations constructed from core subtracted quantities have more positive evolution at higher redshift than those using non-core subtracted quantities, and the scatter of scaling relations and in central surface brightness increases at low redshift.

Observational guidance is required as cluster simulations mature and models of cool core formation, feedback, and energy injection are improved to constrain the formation history of clusters. The work presented in this dissertation provides several important constraints on the evolution of cluster bulk properties and the impact of cluster structural changes, particularly cool core formation and mergers, on those properties.

5.2 Recent Supporting Results

Since the work in Chapter 3 was published Poole et al. (2007) carried out computational investigations of mergers of relaxed clusters, similar in concept to those of Ricker & Sarazin (2001) discussed earlier, but including cooling and star formation. Poole et al. (2007) also specifically examined how merging systems should move on scaling relations as the clusters interact and relax. They found that correlated shifts in cluster parameters indeed take place, though temperature shifts should not be as extreme as predicted by Ricker & Sarazin (2001). While characterizing the track of merging systems along scaling relations, Poole et al. (2007) find that merger-induced shifts in cluster properties are inadequate to explain the magnitude of observed scaling relation scatter, consistent with our observational results.

Using the same simulations, Poole et al. (2006) found that centroid variation provides the best indication of the dynamical state of a cluster, including when mergers take place along axes close to the line of sight. They showed that temperature variations persist long after clusters have relaxed following a merger, and so examining temperature distributions is not a particularly good method of identifying merging systems. This provides support for our choice of centroid variation as our primary substructure indicator in Chapter 3.

Further simulation work has been carried out by McCarthy et al. (2007) in support of the scenario in which cool cores form based on the level of cluster preheating (McCarthy et al. 2004). They find that matching observed cluster entropy profiles requires additional heating in cool core clusters, and propose a model in which cooling material feeds AGN, which in turn heat the material and expel it back into the ICM. This gives predictions largely in line with observations, though some additional processes may be needed. Based on their own simulations, Burns et al. (2007) suggest a model in which formation history determines cool core formation, as non-cool core clusters undergo early major mergers that destroy young cool cores and create conditions that prevent future cool core formation. Neither of these sets of simulations correctly predicts all aspects of clusters as observed, however, and so questions regarding cool core formation still remain.

5.3 Future Directions

There are several potentially productive extensions to the work presented in this dissertation. First, the concept of using central surface brightness to reduce scatter in luminosity–mass relations for cosmology studies needs further exploration. Neither of the methods used to measure I_0 in Chapters 3 and 4 is feasible in cosmology surveys that will lack detailed spectroscopic information necessary to identify a fraction of the virial radius, as in Chapter 4, or even include enough photons to model the surface brightness distribution,

as in Chapter 3; further, point spread function effects could cause difficulties in shallow observations. It may prove necessary to determine I_0 by averaging within some fixed angular aperture, but this will introduce redshift effects, and it remains to be seen if even such a crude estimator is useful when cluster observations contain as few as $\sim$50 photons. These issues could be addressed via existing low-redshift cluster catalogs, as a prelude to planned X-ray cluster surveys.

The approach to cosmological measurements outlined in §4.7, wherein isophotal sizes are used to determine angular diameter distances, also deserves attention. Work must be done to determine how degenerate the input cosmology (used to determine evolution in $f_{\rm ICM}$) and the output cosmology from size measurements are, along with issues regarding the correct matching of the radius for $f_{\rm ICM}$ evolution measurements to the isophote used for measuring distances. If these issues are successfully addressed, this method holds great promise for determining cosmological parameters in a manner complementary to CMB measurements, particularly as larger samples of high-redshift X-ray observations become available.

It would be quite interesting to return to the question of correlation between ICM and galaxy properties, as hinted at via the examination of the $L_{\rm NIR}$–$T_{\rm X}$ relation in Chapter 3. X-ray and near-IR observations of clusters over a range of redshifts can be used to constrain the evolution and interplay of ICM and stellar mass, providing information as to the rate of star formation and stellar feedback as clusters evolve. This in turn will help to constrain models of cluster structural evolution and cool core formation.

Finally, the ICM evolution studies of Chapter 4 must be revisited as larger, flux-limited samples of clusters over similarly wide redshift ranges appear. The results presented here provide some important points of comparison for simulations attempting to model ICM structure and evolution; future work with larger, more complete samples will further enhance these observational constraints.

References

Abell, G. O. 1958, ApJS, 3, 211

Allen, S. W., Rapetti, D. A., Schmidt, R. W., Ebeling, H., Morris, G., & Fabian, A. C. 2007, MNRAS, submitted (arXiv:0706:3277)

Allen, S. W., Schmidt, R. W., Ebeling, H., Fabian, A. C., & van Speybroeck, L. 2004, MNRAS, 353, 457

Allen, S. W., Schmidt, R. W., & Fabian, A. C. 2001, MNRAS, 328, L37

Arnaud, M., & Evrard, A. E. 1999, MNRAS, 305, 631

Arnaud, M., Pointecouteau, E., & Pratt, G. W. 2005, A&A, 441, 893

Bîrzan, L., Rafferty, D. A., McNamara, B. R., Wise, M. W., & Nulsen, P. E. J. 2004, ApJ, 607, 800

Bahcall, N. A., & Cen, R. 1993, ApJ, 407, L49

Bahcall, N. A., Fan, X., & Cen, R. 1997, ApJ, 485, L53

Balestra, I., Tozzi, P., Ettori, S., Rosati, P., Borgani, S., Mainieri, V., Norman, C., & Viola, M. 2007, A&A, 462, 429

Balogh, M. L., Babul, A., Voit, G. M., McCarthy, I. G., Jones, L. R., Lewis, G. F., & Ebeling, H. 2006, MNRAS, 366, 624

Bauer, F. E., Fabian, A. C., Sanders, J. S., Allen, S. W., & Johnstone, R. M. 2005, MNRAS, 359, 1481

Bialek, J. J., Evrard, A. E., & Mohr, J. J. 2001, ApJ, 555, 597

—. 2002, ApJ, 578, L9

Borgani, S., Governato, F., Wadsley, J., Menci, N., Tozzi, P., Quinn, T., Stadel, J., & Lake, G. 2002, MNRAS, 336, 409

Borgani, S., Rosati, P., Tozzi, P., Stanford, S. A., Eisenhardt, P. R., Lidman, C., Holden, B., Della Ceca, R., Norman, C., & Squires, G. 2001, ApJ, 561, 13

Bower, R. G., Benson, A. J., Lacey, C. G., Baugh, C. M., Cole, S., & Frenk, C. S. 2001, MNRAS, 325, 497

Branchesi, M., Gioia, I. M., Fanti, C., & Fanti, R. 2007, A&A, 472, 739

Bryan, G. L. 2000, ApJ, 544, L1

Bryan, G. L., & Norman, M. L. 1998, ApJ, 495, 80

Buote, D. A., & Tsai, J. C. 1995, ApJ, 452, 522

—. 1996, ApJ, 458, 27

Burns, J. O., Hallman, E. J., Gantner, B., Motl, P. M., & Norman, M. L. 2007, ApJ, submitted (arXiv:0708.1954)

Cash, W. 1979, ApJ, 228, 939

Cavaliere, A., & Fusco-Femiano, R. 1978, A&A, 70, 677

Cavaliere, A., Menci, N., & Tozzi, P. 1997, ApJ, 484, L21

—. 1998, ApJ, 501, 493

Cowie, L. L., & Binney, J. 1977, ApJ, 215, 723

Crain, R. A., Eke, V. R., Frenk, C. S., Jenkins, A., McCarthy, I. G., Navarro, J. F., & Pearce, F. R. 2007, MNRAS, 377, 41

David, L. P., Jones, C., & Forman, W. 1995, ApJ, 445, 578

David, L. P., Slyz, A., Jones, C., Forman, W., Vrtilek, S. D., & Arnaud, K. A. 1993, ApJ, 412, 479

Day, C. S. R., Fabian, A. C., Edge, A. C., & Raychaudhury, S. 1991, MNRAS, 252, 394

De Grandi, S., & Molendi, S. 2001, ApJ, 551, 153

de Propris, R., Stanford, S. A., Eisenhardt, P. R., Dickinson, M., & Elston, R. 1999, AJ, 118, 719

Dickey, J. M., & Lockman, F. J. 1990, ARA&A, 28, 215

Dressler, A., & Shectman, S. A. 1988, AJ, 95, 985

Edge, A. C., & Stewart, G. C. 1991, MNRAS, 252, 414

Edge, A. C., Stewart, G. C., Fabian, A. C., & Arnaud, K. A. 1990, MNRAS, 245, 559

Eisenstein, D. J., Zehavi, I., Hogg, D. W., Scoccimarro, R., Blanton, M. R., Nichol, R. C., Scranton, R., Seo, H.-J., Tegmark, M., Zheng, Z., Anderson, S. F., Annis, J., Bahcall, N., Brinkmann, J., Burles, S., Castander, F. J., Connolly, A., Csabai, I., Doi, M., Fukugita, M., Frieman, J. A., Glazebrook, K., Gunn, J. E., Hendry, J. S., Hennessy, G., Ivezić, Z., Kent, S., Knapp, G. R., Lin, H., Loh, Y.-S., Lupton, R. H., Margon, B., McKay, T. A., Meiksin, A., Munn, J. A., Pope, A., Richmond, M. W., Schlegel, D., Schneider, D. P., Shimasaku, K., Stoughton, C., Strauss, M. A., SubbaRao, M., Szalay, A. S., Szapudi, I., Tucker, D. L., Yanny, B., & York, D. G. 2005, ApJ, 633, 560

Ettori, S., Borgani, S., Moscardini, L., Murante, G., Tozzi, P., Diaferio, A., Dolag, K., Springel, V., Tormen, G., & Tornatore, L. 2004a, MNRAS, 354, 111

Ettori, S., De Grandi, S., & Molendi, S. 2002, A&A, 391, 841

Ettori, S., Dolag, K., Borgani, S., & Murante, G. 2006, MNRAS, 365, 1021

Ettori, S., Tozzi, P., Borgani, S., & Rosati, P. 2004b, A&A, 417, 13

Ettori, S., Tozzi, P., & Rosati, P. 2003, A&A, 398, 879

Evrard, A. E., & Gioia, I. M. 2002, in ASSL Vol. 272: Merging Processes in Galaxy Clusters, 253

Evrard, A. E., Metzler, C. A., & Navarro, J. F. 1996, ApJ, 469, 494

Evrard, A. E., Mohr, J. J., Fabricant, D. G., & Geller, M. J. 1993, ApJ, 419, L9

Faber, S. M., & Dressler, A. 1977, AJ, 82, 187

Fabian, A. C., Crawford, C. S., Edge, A. C., & Mushotzky, R. F. 1994, MNRAS, 267, 779

Fabian, A. C., & Nulsen, P. E. J. 1977, MNRAS, 180, 479

Fabricant, D., Lecar, M., & Gorenstein, P. 1980, ApJ, 241, 552

Feretti, L., Giovannini, G., & Bohringer, H. 1997, New Astronomy, 2, 501

Ferramacho, L. D., & Blanchard, A. 2007, A&A, 463, 423

Ferrari, C., Arnaud, M., Ettori, S., Maurogordato, S., & Rho, J. 2006, A&A, 446, 417

Ferrari, C., Maurogordato, S., Cappi, A., & Benoist, C. 2003, A&A, 399, 813

Finoguenov, A., Reiprich, T. H., & Böhringer, H. 2001, A&A, 368, 749

Fukazawa, Y., Makishima, K., Tamura, T., Ezawa, H., Xu, H., Ikebe, Y., Kikuchi, K., & Ohashi, T. 1998, PASJ, 50, 187

Geller, M. J., & Beers, T. C. 1982, PASP, 94, 421

Haiman, Z. ., Mohr, J. J., & Holder, G. P. 2001, ApJ, 553, 545

Henriksen, M. J., & Markevitch, M. L. 1996, ApJ, 466, L79

Hicks, A. K., Wise, M. W., Houck, J. C., & Canizares, C. R. 2002, ApJ, 580, 763

Holden, B. P., Stanford, S. A., Squires, G. K., Rosati, P., Tozzi, P., Eisenhardt, P., & Spinrad, H. 2002, AJ, 124, 33

Hu, W. 2003, Phys. Rev. D, 67, 081304

Hughes, J. P., Butcher, J. A., Stewart, G. C., & Tanaka, Y. 1993, ApJ, 404, 611

Ikebe, Y., Ezawa, H., Fukazawa, Y., Hirayama, M., Ishisaki, Y., Kikuchi, K., Kubo, H., Makishima, K., Matsushita, K., Ohashi, T., Takahashi, T., & Tamura, T. 1996, Nature, 379, 427

Ikebe, Y., Makishima, K., Fukazawa, Y., Tamura, T., Xu, H., Ohashi, T., & Matsushita, K. 1999, ApJ, 525, 58

Irwin, J. A., & Bregman, J. N. 2000, ApJ, 538, 543

Jee, M. J., White, R. L., Ford, H. C., Blakeslee, J. P., Illingworth, G. D., Coe, D. A., & Tran, K.-V. H. 2005, ApJ, 634, 813

Jeltema, T. E., Canizares, C. R., Bautz, M. W., & Buote, D. A. 2005, ApJ, 624, 606

Johnstone, R. M., Fabian, A. C., Edge, A. C., & Thomas, P. A. 1992, MNRAS, 255, 431

Jones, C., & Forman, W. 1984, ApJ, 276, 38

Kaiser, N. 1986, MNRAS, 222, 323

Kay, S. T., da Silva, A. C., Aghanim, N., Blanchard, A., Liddle, A. R., Puget, J.-L., Sadat, R., & Thomas, P. A. 2007, MNRAS, 377, 317

Kempner, J. C., Sarazin, C. L., & Markevitch, M. 2003, ApJ, 593, 291

Kempner, J. C., Sarazin, C. L., & Ricker, P. M. 2002, ApJ, 579, 236

Kotov, O., & Vikhlinin, A. 2005, ApJ, 633, 781

Kravtsov, A. V., Nagai, D., & Vikhlinin, A. A. 2005, ApJ, 625, 588

Kravtsov, A. V., Vikhlinin, A., & Nagai, D. 2006, ApJ, 650, 128

Landau, L. D., & Lifshitz, E. M. 1987, Fluid Mechanics (2nd ed.; Oxford: Butterworth-Heinemann)

Lima, M., & Hu, W. 2005, Phys. Rev. D, 72, 043006

Lin, Y., Mohr, J. J., & Stanford, S. A. 2003, ApJ, 591, 749

—. 2004, ApJ, 610, 745

Lin, Y.-T., Mohr, J. J., Gonzalez, A. H., & Stanford, S. A. 2006, ApJ, 650, L99

Lockman, F. J. 2004, in Astrophysics and Space Science Library, Vol. 309, Soft X-ray Emission from Clusters of Galaxies and Related Phenomena, ed. R. M. J. Lieu, 111

Lopes, P. A. A., de Carvalho, R. R., Capelato, H. V., Gal, R. R., Djorgovski, S. G., Brunner, R. J., Odewahn, S. C., & Mahabal, A. A. 2006, ApJ, 648, 209

Lumb, D. H., Bartlett, J. G., Romer, A. K., Blanchard, A., Burke, D. J., Collins, C. A., Nichol, R. C., Giard, M., Marty, P. B., Nevalainen, J., Sadat, R., & Vauclair, S. C. 2004, A&A, 420, 853

Majumdar, S., & Mohr, J. J. 2003, ApJ, 585, 603

—. 2004, ApJ, 613, 41

Markevitch, M. 1996, ApJ, 465, L1

—. 1998, ApJ, 504, 27

Markevitch, M., Forman, W. R., Sarazin, C. L., & Vikhlinin, A. 1998, ApJ, 503, 77

Markevitch, M., Gonzalez, A. H., David, L., Vikhlinin, A., Murray, S., Forman, W., Jones, C., & Tucker, W. 2002, ApJ, 567, L27

Markevitch, M., Mazzotta, P., Vikhlinin, A., Burke, D., Butt, Y., David, L., Donnelly, H., Forman, W. R., Harris, D., Kim, D.-W., Virani, S., & Vrtilek, J. 2003, ApJ, 586, L19

Markevitch, M., Ponman, T. J., Nulsen, P. E. J., Bautz, M. W., Burke, D. J., David, L. P., Davis, D., Donnelly, R. H., Forman, W. R., Jones, C., Kaastra, J., Kellogg, E., Kim, D.-W., Kolodziejczak, J., Mazzotta, P., Pagliaro, A., Patel, S., Van Speybroeck, L., Vikhlinin, A., Vrtilek, J., Wise, M., & Zhao, P. 2000, ApJ, 541, 542

Markevitch, M., & Vikhlinin, A. 1997, ApJ, 474, 84

—. 2001, ApJ, 563, 95

Matsuzawa, H., Matsuoka, M., Ikebe, Y., Mihara, T., & Yamashita, K. 1996, PASJ, 48, 565

Maughan, B. J., Jones, C., Forman, W., & Van Speybroeck, L. 2007, ApJS, in press (astro-ph/0703156)

Maughan, B. J., Jones, L. R., Ebeling, H., Perlman, E., Rosati, P., Frye, C., & Mullis, C. R. 2003, ApJ, 587, 589

Maughan, B. J., Jones, L. R., Ebeling, H., & Scharf, C. 2006, MNRAS, 365, 509

McCarthy, I. G., Babul, A., Bower, R. G., & Balogh, M. L. 2007, MNRAS, submitted (arXiv:0706.2768)

McCarthy, I. G., Balogh, M. L., Babul, A., Poole, G. B., & Horner, D. J. 2004, ApJ, 613, 811

McNamara, B. R., & O'Connell, R. W. 1992, ApJ, 393, 579

Mohr, J. J., & Evrard, A. E. 1997, ApJ, 491, 38

Mohr, J. J., Evrard, A. E., Fabricant, D. G., & Geller, M. J. 1995, ApJ, 447, 8

Mohr, J. J., Fabricant, D. G., & Geller, M. J. 1993, ApJ, 413, 492

Mohr, J. J., Mathiesen, B., & Evrard, A. E. 1999, ApJ, 517, 627

Mohr, J. J., Reese, E. D., Ellingson, E., Lewis, A. D., & Evrard, A. E. 2000, ApJ, 544, 109

Molendi, S., de Grandi, S., Fusco-Femiano, R., Colafrancesco, S., Fiore, F., Nesci, R., & Tamburelli, F. 1999, ApJ, 525, L73

Morandi, A., Ettori, S., & Moscardini, L. 2007, MNRAS, 379, 518

Muanwong, O., Kay, S. T., & Thomas, P. A. 2006, ApJ, 649, 640

Nagai, D., & Kravtsov, A. V. 2003, ApJ, 587, 514

Navarro, J. F., Frenk, C. S., & White, S. D. M. 1997, ApJ, 490, 493

Neumann, D. M., & Arnaud, M. 1999, A&A, 348, 711

Oegerle, W. R., Hill, J. M., & Fitchett, M. J. 1995, AJ, 110, 32

O'Hara, T. B., Mohr, J. J., Bialek, J. J., & Evrard, A. E. 2006, ApJ, 639, 64

O'Hara, T. B., Mohr, J. J., & Guerrero, M. A. 2004, ApJ, 604, 604

Onuora, L. I., Kay, S. T., & Thomas, P. A. 2003, MNRAS, 341, 1246

Ota, N., Kitayama, T., Masai, K., & Mitsuda, K. 2006, ApJ, 640, 673

Pearce, F. R., Thomas, P. A., & Couchman, H. M. P. 1994, MNRAS, 268, 953

Peres, C. B., Fabian, A. C., Edge, A. C., Allen, S. W., Johnstone, R. M., & White, D. A. 1998, MNRAS, 298, 416

Peterson, J. R., Paerels, F. B. S., Kaastra, J. S., Arnaud, M., Reiprich, T. H., Fabian, A. C., Mushotzky, R. F., Jernigan, J. G., & Sakelliou, I. 2001, A&A, 365, L104

Ponman, T. J., Sanderson, A. J. R., & Finoguenov, A. 2003, MNRAS, 343, 331

Poole, G. B., Babul, A., McCarthy, I. G., Fardal, M. A., Bildfell, C. J., Quinn, T., & Mahdavi, A. 2007, MNRAS, 380, 437

Poole, G. B., Fardal, M. A., Babul, A., McCarthy, I. G., Quinn, T., & Wadsley, J. 2006, MNRAS, 373, 881

Pratt, G. W., Böhringer, H., Croston, J. H., Arnaud, M., Borgani, S., Finoguenov, A., & Temple, R. F. 2007, A&A, 461, 71

Randall, S. W., Sarazin, C. L., & Ricker, P. M. 2002, ApJ, 577, 579

Reiprich, T. H., & Böhringer, H. 2002, ApJ, 567, 716

Ricker, P. M., & Sarazin, C. L. 2001, ApJ, 561, 621

Rines, K., Forman, W., Pen, U., Jones, C., & Burg, R. 1999, ApJ, 517, 70

Roettiger, K., Loken, C., & Burns, J. O. 1997, ApJS, 109, 307

Sadat, R., Blanchard, A., Vauclair, S. C., Lumb, D. H., Bartlett, J., Romer, A. K., Bernard, J.-P., Boer, M., Marty, P., Nevalainen, J., Burke, D. J., Collins, C. A., & Nichol, R. C. 2005, A&A, 437, 31

Sanderson, A. J. R., Finoguenov, A., & Mohr, J. J. 2005, ApJ, 630, 191

Sanderson, A. J. R., Ponman, T. J., Finoguenov, A., Lloyd-Davies, E. J., & Markevitch, M. 2003, MNRAS, 340, 989

Schuecker, P., Böhringer, H., Reiprich, T. H., & Feretti, L. 2001, A&A, 378, 408

Smith, G. P., Kneib, J.-P., Smail, I., Mazzotta, P., Ebeling, H., & Czoske, O. 2005, MNRAS, 359, 417

Spergel, D. N., Bean, R., Doré, O., Nolta, M. R., Bennett, C. L., Dunkley, J., Hinshaw, G., Jarosik, N., Komatsu, E., Page, L., Peiris, H. V., Verde, L., Halpern, M., Hill, R. S., Kogut, A., Limon, M., Meyer, S. S., Odegard, N., Tucker, G. S., Weiland, J. L., Wollack, E., & Wright, E. L. 2007, ApJS, 170, 377

Struble, M. F., & Rood, H. J. 1987, ApJS, 63, 543

Sun, M., Murray, S. S., Markevitch, M., & Vikhlinin, A. 2002, ApJ, 565, 867

Tamura, T., Day, C. S., Fukazawa, Y., Hatsukade, I., Ikebe, Y., Makishima, K., Mushotzky, R. F., Ohashi, T., Takenaka, K., & Yamashita, K. 1996, PASJ, 48, 671

Townsley, L. K., Broos, P. S., Garmire, G. P., & Nousek, J. A. 2000, ApJ, 534, L139

Vikhlinin, A., Burenin, R., Forman, W. R., Jones, C., Hornstrup, A., Murray, S. S., & Quintana, H. 2006, Proc. Heating vs. Cooling in Galaxies and Clusters of Galaxies, in press (astro-ph/0611438)

Vikhlinin, A., Markevitch, M., & Murray, S. S. 2001, ApJ, 551, 160

Vikhlinin, A., Markevitch, M., Murray, S. S., Jones, C., Forman, W., & Van Speybroeck, L. 2005, ApJ, 628, 655

Vikhlinin, A., VanSpeybroeck, L., Markevitch, M., Forman, W. R., & Grego, L. 2002, ApJ, 578, L107

Voit, G. M. 2005, Rev. Mod. Phys., 77, 207

Voit, G. M., & Donahue, M. 1995, ApJ, 452, 164

White, D. A. 2000, MNRAS, 312, 663

Zabludoff, A. I., & Zaritsky, D. 1995, ApJ, 447, L21

Zhang, Y.-Y., Finoguenov, A., Böhringer, H., Kneib, J.-P., Smith, G. P., Czoske, O., & Soucail, G. 2007, A&A, 467, 437

Author's Biography

Tim O'Hara, a native of Midland, Texas, started his university career at the Texas Academy of Mathematics and Science at the University of North Texas, where he received his high school diploma in 1998. He moved on to Carnegie Mellon University, where he completed a B.S. in physics in 2001. Having not quite come to his senses, he entered graduate school in physics at the University of Illinois in 2001. He emerged, battered and bruised but not defeated, in 2007, M.S. and Ph.D. in hand. Along the way he picked up an NSF/JSPS East Asia and Pacific Summer Institutes award, which provided quite generous funding for a summer at the University of Tokyo, and a NASA Graduate Student Researchers Program fellowship, which funded additional travel opportunities, plus that whole monthly paycheck thing.

With six years of basic research deemed sufficient—the travel, flexible working conditions, and general academic environment being insufficient to counterbalance the, well, research—he will begin his post-graduate school career with employment at the CNA Corporation. He really enjoyed grad school a lot more than this blurb makes it sound, but notes that the Graduate College's requirement that the dissertation's biographical sketch begin with the author's name severely cramps said author's style, though at least he managed to avoid "was born".

Publications

1. "Evolution of the Intracluster Medium Between $0.2 < z < 1.3$ in a *Chandra* Sample of 70 Galaxy Clusters"
   O'Hara, T. B., Mohr, J. J., & Sanderson, A. J. R.
   2007, ApJ, submitted

2. "Effects of Mergers and Core Structure on the Bulk Properties of Nearby Galaxy Clusters"
   O'Hara, T. B., Mohr, J. J., Bialek, J. J., & Evrard, A. E.
   2006, ApJ, 639, 64

3. "A *Chandra* Study of the Effects of a Major Merger on the Structure of A2319"
   O'Hara, T. B., Mohr, J. J., & Guerrero, M. A.
   2004, ApJ, 604, 604

4. "The Dust Ring of LBV Candidate HD 168625: Infrared Observations and Model Calculations"
   O'Hara, T. B., Meixner, M., Speck, A. K., Ueta, T., & Bobrowsky, M.
   2003, ApJ, 598, 1255

Conference Presentations

1. "Testing Cluster Evolution with X-ray Scaling Relations"
   O'Hara, T. B. & Mohr, J. J.
   Tracing Cosmic Evolution with Clusters of Galaxies: Six Years Later, 25–29 June 2007, Sesto, Italy

2. "Galaxy Cluster Scaling Relations: Evolution and Scatter"
   O'Hara, T. B. & Mohr, J. J.
   The Extreme Universe in the *Suzaku* Era, 4–8 December 2006, Kyoto, Japan

3. "Effects of Mergers and Core Structure on the Bulk Properties of Nearby Galaxy Clusters"
   O'Hara, T. B., Mohr, J. J., Bialek, J. J., & Evrard, A. E.
   American Astronomical Society Meeting #207, 8–12 January 2006, Washington, DC

4. "Scaling Relations and Substructure in Nearby Clusters"
   O'Hara, T. B. & Mohr, J.J.
   Fundamental Physics from Galaxy Clusters, 9–11 December 2004, Fermilab

5. "Effects of Mergers on the Structure of Galaxy Clusters"
   O'Hara, T. B. & Mohr, J. J.
   AAS High Energy Astrophysics Division Meeting, 8–11 September 2004, New Orleans, LA

6. "A *Chandra* Study of the Merger in Abell 2319"
   O'Hara, T. B., Mohr, J. J., & Guerrero, M. A.
   American Astronomical Society Meeting #203, 4–8 January 2004, Atlanta, GA

7. "The Dust Ring of LBV Candidate HD 168625"
   O'Hara, T. B., Meixner, M., Speck, A. K., Ueta, T., & Bobrowsky, M.
   American Astronomical Society Meeting #201, 5–9 January 2003, Seattle, WA

8. "The Circumstellar Dust Shell of LBV HD 168625: Model Calculations"
   Ueta, T., O'Hara, T. B., Meixner, M., Speck, A. K., & Bobrowsky, M.
   Eta Carinae Workshop, 10–13 July 2002, Mt. Rainier, WA

9. "Infrared Imaging of the Nebula Around *IRAS* 18184-1623"
   O'Hara, T. B., Meixner, M., Speck, A. K., Ueta, T., & Bobrowsky, M.
   American Astronomical Society Meeting #199, 6–10 January 2002, Washington, DC